



**HAL**  
open science

# atherosclerotic plaque adhesion strength and its role in plaque rupture

Bilal Merei

► **To cite this version:**

Bilal Merei. atherosclerotic plaque adhesion strength and its role in plaque rupture. Other. Université de Lyon; University of South Carolina, 2016. English. NNT : 2016LYSEM016 . tel-01665012

**HAL Id: tel-01665012**

**<https://theses.hal.science/tel-01665012>**

Submitted on 15 Dec 2017

**HAL** is a multi-disciplinary open access archive for the deposit and dissemination of scientific research documents, whether they are published or not. The documents may come from teaching and research institutions in France or abroad, or from public or private research centers.

L'archive ouverte pluridisciplinaire **HAL**, est destinée au dépôt et à la diffusion de documents scientifiques de niveau recherche, publiés ou non, émanant des établissements d'enseignement et de recherche français ou étrangers, des laboratoires publics ou privés.



N°d'ordre NNT : 2016LYSEM016

## **THESE de DOCTORAT DE L'UNIVERSITE DE LYON**

opérée au sein de

**MINES Saint-Etienne**

**délivrée en partenariat international avec 'University of South Carolina'**

**Ecole Doctorale N° 488**  
**Sciences, Ingénierie, Santé**

**Spécialité de doctorat :**  
**Discipline** : Mécanique et ingénierie

Soutenue à huis clos le 29/09/2016, par :

**Bilal Merei**

---

# **Force d'adhésion des plaques athérosclérotiques et son rôle dans leur détachement**

---

Devant le jury composé de :

Ohayon, Jacques	Professeur	Université de Savoie	Président et
Rapporteur			

Shazly, Tarek	Professeur	University of South Carolina	Rapporteur
Avril, Stéphane	Professeur	EMSE-CIS	Directeur
Lessner, Susane	Professeur	USC-School of medicine	Directrice
Sutton, Mickael	Professeur	University of South Carolina	Co-directeur
Badel, Pierre	Professeur	EMSE-CIS	Co-directeur

Spécialités doctorales	Responsables :	Spécialités doctorales	Responsables
SCIENCES ET GENIE DES MATERIAUX	K. Woldi, Directeur de recherche	MATHEMATIQUES APPLIQUEES	G. Roustant, Maître-assistant
MECANIQUE ET INGENIERIE	S. Dreyer, professeur	INFORMATIQUE	O. Boissier, Professeur
GENIE DES PROCÉDES	F. Crey, Maître de recherche	IMAGE, VISION, SIGNAL	J.C. Pinol, Professeur
SCIENCES DE LA TERRE	B. Gey, Directeur de recherche	GENIE INDUSTRIEL	A. Delguy, Professeur
SCIENCES ET GENIE DE L'ENVIRONNEMENT	D. Gnilot, Directeur de recherche	MICROELECTRONIQUE	S. Dazeres Paris, Professeur

**EMSE : Enseignants-chercheurs et chercheurs autorisés à diriger des thèses de doctorat (titulaires d'un doctorat d'État ou d'une HDR)**

AISI	Nabil	CR	Génie industriel	CMP
AVRIL	Stéphane	PR2	Mécanique et ingénierie	CIS
BALBO	Florent	PR2	Informatique	FAYOL
BASSEREAU	Jean-François	PR	Sciences et génie des matériaux	SMS
BATTON-HUBERT	Mirella	PR2	Sciences et génie de l'environnement	FAYOL
BERGER DOUCE	Sandrine	PR2	Sciences de gestion	FAYOL
BERNACHE-ASSOLLANT	Didier	PR0	Génie des Procédés	CIS
BHOOT	Jean Pierre	MR(DRZ)	Génie des Procédés	SPIN
BELAL	Essid	DR	Sciences de la Terre	SPIN
BLAYAC	Sylvain	MA(MDC)	Microélectronique	CMP
BOISSIER	Olivier	PR1	Informatique	FAYOL
BORBELY	Andras	MR(DRZ)	Sciences et génie des matériaux	SMS
BOUCHER	Xavier	PR2	Génie Industriel	FAYOL
BRODHAG	Christian	DR	Sciences et génie de l'environnement	FAYOL
BRUCHON	Jélan	MA(MDC)	Mécanique et ingénierie	SMS
BURLAT	Patrick	PR1	Génie Industriel	FAYOL
COURNIL	Michel	PR0	Génie des Procédés	DIR
DAERHULAT	Michel	IGM	Sciences et génie des matériaux	SMS
DAUZERE-PERES	Stéphane	PR1	Génie Industriel	CMP
DEBAYLE	Jehan	CR	Image Vision Signal	CIS
DELAFOSSÉ	David	PR0	Sciences et génie des matériaux	SMS
DESRAYAUD	Christophe	PR1	Mécanique et ingénierie	SMS
DOUGUI	Alexandre	PR0	Génie Industriel	FAYOL
DRAPER	Sylvain	PR1	Mécanique et ingénierie	SMS
FEUILLET	Dominique	PR1	Génie Industriel	CMP
FEVOTTE	Gilles	PR1	Génie des Procédés	SPIN
FRACZKIEWICZ	Anna	DR	Sciences et génie des matériaux	SMS
GARCIA	Daniel	MR(DRZ)	Génie des Procédés	SPIN
GERINIER	Jean	MA(MDC)	Sciences et génie des matériaux	CIS
GOELREOT	Dominique	DR	Sciences et génie des matériaux	SMS
GRAILLOT	Didier	DR	Sciences et génie de l'environnement	SPIN
GROSSEAU	Philippe	DR	Génie des Procédés	SPIN
GRUY	Frédéric	PR1	Génie des Procédés	SPIN
GUY	Bernard	DR	Sciences de la Terre	SPIN
HAN	Woo-Suck	MR	Mécanique et ingénierie	SMS
HERRI	Jean Michel	PR1	Génie des Procédés	SPIN
KERMOUCHE	Guillaume	PR2	Mécanique et Ingénierie	SMS
KLOCKER	Helmert	DR	Sciences et génie des matériaux	SMS
LAFORÉST	Valérie	MR(DRZ)	Sciences et génie de l'environnement	FAYOL
LERICHE	Rodolphe	CR	Mécanique et ingénierie	FAYOL
LJ	Jean-Michel		Microélectronique	CMP
MALLIARAS	Georges	PR1	Microélectronique	CMP
MAURINE	Philippe			CMP
MOLIMARD	Arteso	PR2	Mécanique et ingénierie	CIS
MONTHEILLIET	Frank	DR	Sciences et génie des matériaux	SMS
MOUTTE	Jacques	CR	Génie des Procédés	SPIN
NEUBERT	Gilles			FAYOL
NIKOLOVSKI	Jean-Pierre	Ingénieur de recherche		CMP
NORTIER	Patrice	PR1		SPIN
PUDLAT	Christophe	PR0	Génie des Procédés	SPIN
PUDLAT	Michèle	PR1	Génie des Procédés	SPIN
PINOLI	Jean Charles	PR0	Image Vision Signal	CIS
POURCHEZ	Jérémy	MR	Génie des Procédés	CIS
ROBISSON	Iltuso	Ingénieur de recherche		CMP
ROUSSY	Agathe	MA(MDC)	Génie industriel	CMP
ROUSTANT	Olivier	MA(MDC)	Mathématiques appliquées	FAYOL
ROUX	Christian	PR	Image Vision Signal	CIS
STOLARZ	Jacques	CR	Sciences et génie des matériaux	SMS
TRIA	Asia	Ingénieur de recherche	Microélectronique	CMP
VALDIVIESO	François	PR2	Sciences et génie des matériaux	SMS
VIRICELLE	Jean Paul	DR	Génie des Procédés	SPIN
WOLSKI	Krzysztof	DR	Sciences et génie des matériaux	SMS
XIE	Xiaolan	PR1	Génie industriel	CIS
YUOMA	Galban	CR	Génie industriel	CMP

**ENISE : Enseignants-chercheurs et chercheurs autorisés à diriger des thèses de doctorat (titulaires d'un doctorat d'État ou d'une HDR)**

BERGHEAU	Jean-Michel	PU	Mécanique et Ingénierie	ENISE
BERTRAND	Philippe	MCF	Génie des procédés	ENISE
DUBUIET	Philippe	PU	Mécanique et Ingénierie	ENISE
FEULVARCH	Eric	MCF	Mécanique et Ingénierie	ENISE
FORTUNIER	Roland	PR	Sciences et Génie des matériaux	ENISE
GUSSAROV	Andrey	Enseignant contractuel	Génie des procédés	ENISE
HAMDE	Hédi	MCF	Mécanique et Ingénierie	ENISE
LYONNET	Patrick	PU	Mécanique et Ingénierie	ENISE
REICH	Joël	PU	Mécanique et Ingénierie	ENISE
SMUROV	Igor	PU	Mécanique et Ingénierie	ENISE
TOSCANO	Rosario	PU	Mécanique et Ingénierie	ENISE
ZAHOUANI	Hassan	PU	Mécanique et Ingénierie	ENISE

Mise à jour : 26/10/2014

ATHEROSCLEROTIC PLAQUE ADHESION STRENGTH AND ITS ROLE IN PLAQUE  
RUPTURE

by

Bilal MEREI

Mechanical Engineer & Master in Science and technologies for health  
Lebanese University Faculty of Engineering, UTC France, 2010

Master of Biomechanics  
Ecole des Arts et Metiers ParisTech, 2011

---

Submitted in Partial Fulfillment of the Requirements

For the Degree of Doctor of Philosophy in

Biomedical Engineering

College of Engineering and Computing

University of South Carolina

2016

Accepted by:

Stephane Avril, Major Professor

Susan M. Lessner, Major Professor

Michael A. Sutton, Committee Member

Pierre Badel, Committee Member

Cheryl Addy, Vice Provost and Dean of the Graduate School

© Copyright by Bilal Merei, 2016  
All Rights Reserved.

## **ACKNOWLEDGEMENTS**

I would like to gratefully and sincerely thank Dr. Stephane Avril for his guidance, understanding, patience, and most importantly, his friendship during my graduate studies at Ecole des Mines de Saint Etienne. His mentorship was paramount in providing a well-rounded experience consistent my long-term career goals. Also, I would like to thank Dr. susan Lessner from USC for her guidance and her help in every detail when I was in Columbia. I was lucky also to meet and work with Dr. Mickael Sutton who enriched my research experience, thanks to his advanced knowledge in the field of fracture mechanics. The work could not be done without Dr. Pierre Badel contributions, thank you for always giving me right advices when I needed and for the help in different topics.

I had the chance to be in a joint program and be in two cities during my Phd. This was not always easy but some great people and colleagues made life simpler. I would like to thank both laboratories in EMSE and USC. To my colleagues Moe, Lindsey, Alexandre, Baptiste, Rebecca, Pierre Yves, Nico, Aron, Fanny, Fanette, Shana and many others, it was a great experience with you. Special thanks to Sareh and Amelie from EMSE for all the support they gave to me and their priceless contributions. Even if we didn't work directly together, but I was also lucky to meet and share my experience with Dr. Shazly and Dr. Eberth from USC, and get many constitutive advices from them.

Obviously being surrounded by friends is the best feeling to give all the motivation you need. Thank you Chaker, my dearest friend, for giving me all the moral support I needed for more than 20 years. Thank you Katerina, my adorable friend, for being a part of this dissertation with all your effort to help in every single detail, you are amazing, and yes 'tu es la meilleure'. To Youssef, Leonardo, Laeticia, thank you for all the encouragements. Special thanks to Katie, Dwain, and Cole, I couldn't picture my stay in the US without you.

And finally, thank you my family, my brother, my sisters, my 12 nephews, and sure my father and mother. You are my first motivation for success and I hope you are proud of me.

## **FRENCH ABSTRACT**

Les maladies cardio-vasculaires sont des maladies qui affectent les vaisseaux sanguins et le cœur. Selon l'Organisation mondiale de la santé, les maladies cardiovasculaires sont l'une des principales causes de décès dans le monde entier. Elles sont responsables de plus de 17,1 millions de décès par an dans le monde, ce qui représente 31,5% des décès <sup>1, 2</sup>. L'athérosclérose, connue par un trouble inflammatoire chronique affectant les grandes artères, est la cause sous-jacente de nombreuses maladies cardio-vasculaires. La rupture de la plaque athérosclérotique est une complication grave de l'athérosclérose avancée, qui conduit souvent à des conséquences cliniques potentiellement mortelles telles que l'infarctus du myocarde (crise cardiaque) ou un AVC. Plus que 75% des cas d'infarctus du myocarde nouvellement développés sont causés par la rupture de plaque. Elle touche environ 1,1 million de personnes aux Etats-Unis par an, avec un taux de létalité de 40%; 220.000 de ces décès surviennent sans hospitalisation. Au cours des dernières décennies, les mécanismes de la progression de la plaque d'athérome et de formation ont été largement étudiés. Toutefois, en raison de la complexité des processus, les mécanismes de rupture de la plaque sont encore mal connus.

Dans cette thèse, une nouvelle hypothèse concernant les mécanismes de rupture de plaque est proposée. Plus précisément, nous supposons que la force d'adhérence de la liaison entre la plaque et la paroi vasculaire est un déterminant important de la stabilité de

la plaque athérosclérotique (résistance à la rupture). Nous nous attendons également à ce que la force d'adhésion soit fonction de la composition de la plaque et de la matrice extracellulaire (ECM) à l'interface plaque-support. Ce mode de rupture proposé est appelé délaminage.

Les essais de délaminage de plaques de souris sont compliqués et ils nécessitaient plus de temps pour être exécutés et validés. Ainsi, en raison de la similitude du protocole expérimental, nous avons utilisé des données expérimentales obtenues sur la dissection de spécimens des artères coronaires humaines par Wang et al. 2014<sup>3</sup>, et nous avons créé un modèle numérique pour appliquer la technique des éléments cohésifs à ce problème. La dissection artérielle est une maladie rare mais potentiellement mortelle dans laquelle le sang passe à travers la paroi interne et entre les couches de la paroi artérielle. Elle se traduit par une séparation des différentes couches, créant ainsi une fausse lumière dans le processus. Les avantages pour la réalisation d'une étude primaire sur la dissection artérielle ont été déterminants pour décider d'appliquer les modèles de zone cohésive à un problème moins complexe que l'athérosclérose.

Expérimentalement, l'approche technique innovante pour mesurer la force d'adhésion développée précédemment<sup>4,3</sup> sera appliquée dans cette thèse sur des souris de deux génotypes différents. Notre équipe à l'USC, a été la première à effectuer ce type de mesures sur des souris. L'utilisation de souris dans nos expériences, présente l'avantage que la composition de la matrice extracellulaire pourrait être systématiquement modifiée

en utilisant des souches transgéniques, le régime alimentaire modifié, ou des traitements médicamenteux. Différentes souches de souris ou modèles pourraient alors être utilisées et les propriétés mécaniques seront étudiées sur chaque type.

Une autre innovation de notre travail implique l'application d'un modèle de zone cohésive pour décrire le comportement de délaminage des plaques athérosclérotiques dans une gamme de conditions physiologiques et physiopathologiques, en utilisant un modèle numérique 2D. Bien que l'approche de la zone cohésive soit largement utilisée pour modéliser les mécanismes de rupture dans les matériaux d'ingénierie classiques, elle est peu utilisée pour décrire le délaminage des plaques. L'étude qui a traité le délaminage par Leng et al. 2015<sup>5</sup> avait pour objectif de tester l'utilisation de zones cohésives en implémentant une loi de traction séparation spécifique, en assumant des valeurs de paramètres des lois de comportement de la plaque et de la zone cohésive. L'innovation dans notre approche est d'utiliser un schéma explicite et une loi de traction séparation simple pour étudier le comportement des plaques et identifier leurs propriétés. Les données expérimentales de délaminage des plaques seront utilisées dans la définition des lois traction-séparation de la zone cohésive.

**MOTS-CLÉS:** Maladies cardiovasculaires - dissection artérielle - plaque athérosclérotique - Modes de délamination - Mécanique de Rupture – Modèle à zone cohésive - Méthode Inverse

## ENGLISH ABSTRACT

Cardiovascular diseases are disorders affecting the blood vessels and the heart. According to the World Health Organization, cardiovascular diseases are one of the leading causes of death worldwide. They are responsible for over 17.1 million deaths per year worldwide, representing 31.5% of deaths <sup>1, 2</sup>. Atherosclerosis, a chronic inflammatory disorder affecting large arteries, is the underlying cause of many cardiovascular diseases. Plaque rupture is a serious complication of advanced atherosclerosis, often leading to life-threatening clinical consequences such as myocardial infarction (heart attack) or stroke. 75% of newly developed myocardial infarction cases are caused by atherosclerotic plaque rupture. It affects approximately 1.1 million people in the USA per year, with a 40% fatality rate; 220,000 of these deaths occur without hospitalization. Over the past few decades, the mechanisms of atherosclerotic plaque progression and formation have been widely studied. However, due to the complexity of the process, plaque rupture mechanisms are still poorly understood.

In this thesis, a novel hypothesis regarding mechanisms of plaque rupture is proposed. Specifically, we hypothesize that the adhesive strength of the bond between the plaque and the vascular wall is an important determinant of atherosclerotic plaque stability (resistance to rupture). We also expect adhesive strength to be a function of plaque composition and extracellular matrix (ECM) organization at the plaque-media interface. This proposed mode of rupture is called delamination or plaque peeling.

Mouse plaque peeling experiments were very challenging and they needed time to be performed and validated. Thus, due to similarity of the experimental protocol, we used experimental data obtained on the dissection of human coronary artery specimens by Ying Wang<sup>3</sup>, and we created a numerical model to apply the cohesive zone technique to this problem. Arterial dissection is a rare but potentially fatal condition in which blood passes through the inner lining and between the layers of the arterial wall. It results in separation of the different layers, creating a false lumen in the process. The advantages to performing a primary study on arterial dissection were first to apply the cohesive zone models to a less complex problem than atherosclerosis.

The innovative technical approach to measure the adhesive strength developed previously<sup>4,3</sup>, will be applied in this thesis to mice. It includes a micro-scale peel experiment protocol to measure adhesive strength of mouse atherosclerotic plaques during delamination from the underlying vessel wall. Our team at USC, as far as we know, was the first to perform these types of measurements on mice. The use of mice in our experiments presents the advantage that the extracellular matrix composition could be systematically changed using transgenic strains, altered diet, or drug treatments. Different mouse strains or models could then be used and the mechanical properties will be studied on each type.

Another innovation of our work will involve application of a cohesive zone model to describe delamination behavior of atherosclerotic plaques under a range of

physiological and pathophysiological conditions, using a 2D numerical model. While the cohesive zone approach has been widely used to model fracture mechanics in classic engineering materials, it was rarely applied to describe failure of atherosclerotic plaques. The study of plaque delamination by Leng et al. 2015<sup>5</sup> was designed to test the use of cohesive zones by implementing a specific traction separation law, assuming the parameter values of the behavior laws of the plaque and the cohesive zone using values from the literature. Innovation in our approach is to use a simple traction separation law to study the behavior of plaques and identifying their properties. Experimental results of delamination of the plaques were used in the definition of traction-separation laws of the cohesive zone.

**KEYWORDS:** Cardiovascular Diseases – Arterial Dissection – Atherosclerotic Plaque – Delamination Mode – Fracture Mechanics – Cohesive Zone Model – Inverse Method ...

## TABLE OF CONTENTS

<b>ACKNOWLEDGEMENTS .....</b>	<b>v</b>
<b>FRENCH ABSTRACT .....</b>	<b>v</b>
<b>ENGLISH ABSTRACT .....</b>	<b>x</b>
<b>TABLE OF CONTENTS .....</b>	<b>xiii</b>
<b>LIST OF TABLES.....</b>	<b>xvii</b>
<b>LIST OF FIGURES.....</b>	<b>xviii</b>
<b>CHAPTER 1 INTRODUCTION AND STATE OF ART .....</b>	<b>1</b>
<i>Section 1 – Biological introduction.....</i>	<i>1</i>
I – Anatomy of healthy arteries .....	1
II – Atherosclerotic plaque formation .....	3
III – Role of collagen in extracellular matrix .....	5
IV – Conclusion.....	6
<i>Section 2 – Mechanical introduction .....</i>	<i>7</i>
I – History and Griffith theory .....	7
II – Cohesive models .....	9
III – Mechanical properties of arterial and atherosclerotic plaque components 10	
IV – Conclusion.....	12
<i>Section 3 – State of art and literature review.....</i>	<i>13</i>
I – Arterial dissection.....	13
II – Plaque rupture mechanisms .....	14
A –Histological features of vulnerable plaques.....	14

B – Role of circumferential tensile stress in plaque rupture .....	15
C – Fatigue and fracture mechanics .....	16
III – Conclusion .....	18
<i>Section 4 – Fracture mechanics in soft tissue biomechanics .....</i>	<i>19</i>
I – Experiments .....	19
II – Numerical studies .....	21
III – Conclusion .....	25
<b>CHAPTER 2 ARTERIAL DISSECTION: IDENTIFICATION OF MECHANICAL AND DISSECTION PROPERTIES IN HUMAN CORONARY ARTERIES USING AN INVERSE METHOD .....</b>	<b>28</b>
<i>Abstract .....</i>	<i>28</i>
<i>Section 1 – Introduction .....</i>	<i>29</i>
<i>Section 2 – Materials and Methods .....</i>	<i>31</i>
I – <i>Experiments .....</i>	<i>31</i>
II – Numerical model: characterization of material parameters .....	34
A – Geometry and boundary conditions .....	34
B – Material model .....	38
C – Inverse method .....	39
<i>Section 3 – Results .....</i>	<i>45</i>
I – Notch length characterization .....	45
II – Material parameters .....	46
A – Arterial layer properties .....	47
B – Interface layer properties (cohesive parameters) .....	49
1 – Dissection through Intima .....	49
2 – Dissection through Media .....	50
<i>Section 4 – Discussion .....</i>	<i>51</i>

Section 5 – Conclusions & Future Work.....	56
<b>CHAPTER 3 ATHEROSCLEROTIC PLAQUE DELAMINATION: 2D FINITE ELEMENT MODEL TO SIMULATE PLAQUE PEELING IN APOE KNOCKOUT AND APOE COL8 DOUBLE KNOCKOUT MICE .....</b>	<b>57</b>
<i>Abstract</i> .....	57
Section 1 – Introduction.....	58
Section 2 – Materials and methods.....	60
I – Experimental protocol .....	60
II – Delamination Test and Data Acquisition Experimental Protocol .....	63
A –Determination of the fracture energy from each delamination cycle $\Delta E$ .....	63
B –Determination of exposed area $\Delta A$ .....	64
C –Calculation of G (energy release rate) .....	65
D –Statistical analysis .....	65
III – Finite-Element model .....	66
A –Abaqus Explicit .....	66
B –Geometry.....	66
1 – Plaque length ( $L_p$ ) measurement .....	67
2 – Plaque height ( $H_p$ ) measurement.....	68
3 – Plaque width ( $W_p$ ) measurement.....	68
C –Boundary Conditions .....	69
Mesh size .....	70
D –Material Model .....	71
1 – Necrotic core .....	71
2 – Fibrous cap and underlying aorta .....	71
3 – Interface between the plaque and the aorta.....	71
IV – Parameter identification using an inverse method .....	72

V – Energy Balance.....	75
<i>Section 3 – Results</i> .....	75
I – Experimental results.....	75
II – Numerical results .....	76
<i>Section 4 – Discussion</i> .....	83
I – Discussion of experimental results.....	83
II – Discussion of numerical results .....	85
<i>Section 5 – Conclusion</i> .....	89
<b>CHAPTER 4 CONCLUSION AND FUTURE WORK.....</b>	<b>91</b>
<b>REFERENCES .....</b>	<b>95</b>
<b>CHAPTER 5 APPENDIX .....</b>	<b>110</b>
Appendix 1.....	110
Appendix 2 .....	113
Appendix 3 .....	115

## LIST OF TABLES

Table 1.1: Collagens and collagen-like proteins in vertebrates .....	6
Table 1.2: Dissection energy calculated experimentally for different arterial samples in literature .....	20
Table 1.3: Numerical studies and the resolution scheme chosen for the models .....	24
Table 2.1: Width values for the different specimens used (mm).....	34
Table 2.2: Thickness of the three layers composing the sample.....	35
Table 2.3: G values obtained for cycle 1 from different samples .....	42
Table 2.4: Notch length corresponding to the minimum error between the numerical and experimental points.....	45
Table 2.5: C10 values for different samples (table format) .....	48
Table 2.6: Cohesive parameters corresponding to the minimum error between numerical and experimental curves in dissection through intima cases .....	49
Table 2.7: Cohesive parameters corresponding to the minimum error between numerical and experimental curves in dissection through media cases.....	50
Table 2.8: R values reported from literature .....	51
Table 2.9: R values calculated for the samples studied .....	52
Table 2.10: Cohesive parameters used in different published numerical studies .....	53
Table 3.1: Number of plaques and cycles obtained from each mouse group .....	62
Table 3.2: Plaque Geometry: (Lp) Plaque Length, (Wp) Plaque Width and (Hp) Plaque Height.....	68
Table 3.3: Statistical parameters for energy release rate, stiffness, and failure load values for ApoE <sup>-/-</sup> and ApoE <sup>-/-</sup> Col8 <sup>-/-</sup> mice.....	76
Table 5.1: $\Delta A$ , $\Delta E$ and G values for the ApoE <sup>-/-</sup> mouse group.....	113
Table 5.2: $\Delta A$ , $\Delta E$ and G values for the ApoE <sup>-/-</sup> Col8 <sup>-/-</sup> mouse group .....	114

## LIST OF FIGURES

Figure 1.1: A cross section of a normal vessel showing the different layers in human arteries, veins and capillaries ( <a href="http://www.vascularconcepts.com">http://www.vascularconcepts.com</a> ) .....	2
Figure 1.2: Atherosclerotic plaque composition.....	4
Figure 1.3: Traction/separation schematic curve for bilinear cohesive zone models.....	10
Figure 1.4: Stress Strain arterial response.....	11
Figure 1.5: Elastic and damage loading stages of the cohesive model: state of damage $\delta n$ , elastic stiffness $c_n$ and elastic traction limit $t_n$ at $\delta n$ defined by Gasser et al. 2006 <sup>73</sup> .....	22
Figure 1.6: Set of cohesive laws considered in the model used in Ferrara et al. 2010 study <sup>84</sup> . Both cohesive strengths and critical energy release rates are scaling proportionally. The maximum opening displacement $\delta c$ does not change .....	23
Figure 1.7: Chart representing the work plan for the next chapters.....	27
Figure 2.1: Schematic of the delamination process (longitudinal view) .....	32
Figure 2.2: First cycles (Load vs Displacement) obtained for one sample (LAD4-R3)...	33
Figure 2.3: Histological picture showing the three layers media, intima and adventitia..	35
Figure 2.4: Simplified representation of the 2D model used to simulate the dissection through the media .....	36
Figure 2.5: Simulation of the peeling test at 4 different times throughout the test.....	37
Figure 2.6: Traction/separation schematic curve for Bilinear Cohesive Zone models.....	39
Figure 2.7: Cost function values for LAD6 case with respect to the variation of $T_0$ (cohesive) and $C_{10}$ (elastic) parameters .....	43
Figure 2.8: Experimental versus simulation curves obtained with the minimum cost value, for samples dissected through the intima .....	46
Figure 2.9: Experimental versus simulation curves obtained with the minimum cost value, for samples dissected through the media.....	47
Figure 2.10: Characterization of $C_{10}$ for the three layers of different samples (Histogram format).....	48
Figure 2.11: Average $C_{10}$ values for the three layers .....	49
Figure 3.1: Schematic of the experimental setup; (a): the Bose machine prescribes a displacement (actuator) and records the resulting force (load cell). The micro-clamps are attached to the actuator and grip the tip of the plaque (b) Schematic of delamination process.....	62

Figure 3.2: A representative image of the raw force vs. displacement data. The area under the load-displacement curve represents the energy released during one delamination cycle. The linear region depicted is used to determine the plaque stiffness for each cycle ..... 64

Figure 3.3: The estimated  $\Delta A$  for one cycle, outlined by yellow (top view)..... 65

Figure 3.4 : Schematic representation of the plaque model and the underlying aorta. (a):  $L_m$  represents the aortic media length,  $L_p$  the plaque length,  $W_m$  the medial width,  $W_p$  the plaque width,  $H_m$  the medial height and  $H_p$  the maximum plaque height ( $L_m$  not shown to scale); (b): 2D representation of the atherosclerotic plaque (green) attached by cohesive elements to the underlying aorta (blue), lying on the gray rigid surface (S). The bottom edge of S, the left & right edges of (A+S), and the top left edge of A were clamped to simulate experimental testing conditions. The reference point represents the master node where displacement boundary conditions were applied. .... 67

Figure 3.5: Simulation of the peeling test at 4 different times throughout the test..... 70

Figure 3.6: Traction/separation curve for Bilinear Cohesive Zone model ..... 72

Figure 3.7: Variation of cost function values with respect to  $C_{10}$ , with  $T_0=0.05-0.10$  MPa for the sample 173P1 ApoE<sup>-/-</sup> Col8<sup>-/-</sup> ..... 75

Figure 3.8: Force-displacement curve obtained after simulation for 1 sample. The curve consists of three segments: 1 represents the deformation of the attached peel arm of the plaque, 2 represents the separation phase where the cohesive elements are deleted to simulate the separation, and 3 represents the unloading phase. Segment 2 displays serrations related to the deletion of cohesive elements..... 77

Figure 3.9: Experimental vs simulated force-displacement curves and strain vs kinetic energy for the first delamination cycles from four ApoE<sup>-/-</sup> mice..... 79

Figure 3.10: Experimental vs simulated force-displacement curves and strain vs kinetic energy for the first delamination cycles from four ApoE<sup>-/-</sup> Col8<sup>-/-</sup> mice ..... 80

Figure 3.11: Histograms of average identified values and standard deviations for (a) G, (b)  $T_0$ , and (c)  $C_{10}$ ..... 82

Figure 3.12: Average and standard deviation of the G values obtained for the 8 months and 6 months ApoE<sup>-/-</sup> mouse groups..... 85

Figure 4.1: Experiment vs numerical load displacement curves for two successive cycles using same material parameter values obtained for the first cycle ..... 93

Figure 5.1: (a) Example of the strain energy and the total energy curves vs crack length, for  $G_c = 0.0025$  N/mm (b) the average ratio of  $(\Delta S/\Delta a) / (\Delta T/\Delta a)$  vs.  $G_c$  values ..... 112

Figure 5.2: Force vs Displacement curves obtained experimentally for the 5 plaques tested from the ApoE<sup>-/-</sup> mouse group..... 115

Figure 5.3: Force vs Displacement curves obtained experimentally for 6 plaques tested from the ApoE<sup>-/-</sup> Col8<sup>-/-</sup> mouse group ..... 116

Figure 5.4: Force vs Displacement curves obtained experimentally for the remaining 3 plaques tested from the ApoE<sup>-/-</sup> Col8<sup>-/-</sup> mouse group ..... 116

# CHAPTER 1 INTRODUCTION AND STATE OF ART

## Section 1 – **Biological introduction**

### I – **Anatomy of healthy arteries**

Each individual has his own arterial tree. The shapes, lengths or even the positions of the various arteries and veins are very variable from one person to another. This particularity is due to the growth and history of each person, which leads to important anatomical differences. Nevertheless, the arteries all have a common structure: the arterial walls are composed of three concentric layers<sup>6</sup>, as represented in Figure 1.1:

- The intima (inner coat) consists of endothelial cells. Endothelial cells are flat cells which interleave into each other forming a smooth surface limiting friction with the blood. They are fixed on a basal lamina, assembled of proteins and extra-cellular glycoproteins, delivering nutrients and removing wastes from the endothelial layer. Endothelial cells themselves are surrounded by connective tissue (cells separated by an extracellular matrix) called the sub-endothelial layer<sup>7</sup>.

- The media (tunica media) consists of smooth muscle cells embedded in an extracellular matrix composed of collagen and elastin fibers.

- The adventitia (tunica adventitia) is mainly composed of collagen, but also elastin, fat cells and blood vessels.

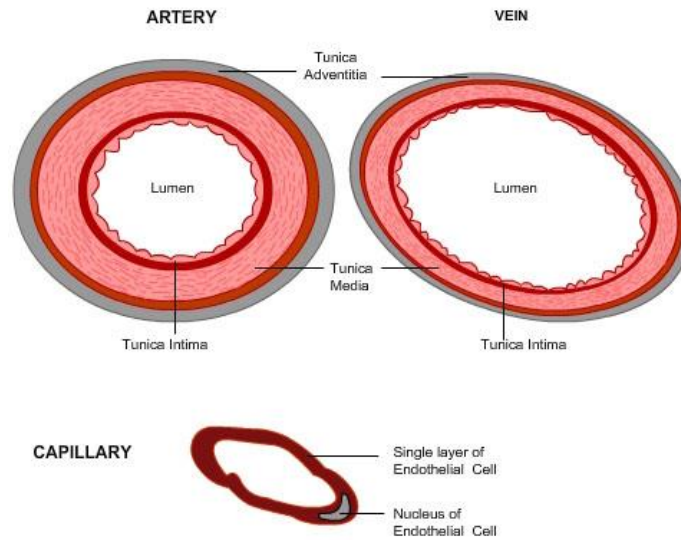


Figure 1.1: A cross section of a normal vessel showing the different layers in human arteries, veins and capillaries (<http://www.vascularconcepts.com>)

Smooth muscle cells, elastic and collagen fibers are considered the main structural components of the different layers of the artery; each component has its own properties.

Elastic fibers (mostly elastin) have a diameter on the order of microns. They are present in the form of a network<sup>8</sup>. Elastic fibers can withstand very large deformations (2000%)<sup>9</sup>.

Collagen fibers provide most of the strength of the artery<sup>10</sup>.

Smooth muscle cells allow the modification of the geometry of the arteries.

The morphology and the proportion of each of the three layers can vary depending on the function and location of the artery. Thus there are three different kinds of arteries:

- The elastic arteries, which have the largest diameter and whose media contains a high proportion of elastin. They deform easily under the action of the blood<sup>11</sup>. This group contains the most well-known arteries such as the aorta, pulmonary artery, or carotid arteries.
- Muscular arteries, which contain more medial smooth muscle cells and less elastin than the elastic arteries<sup>12</sup>.

## **II – Atherosclerotic plaque formation**

Atherosclerosis is a chronic inflammatory disease of the large elastic arteries characterized by a progressive accumulation of lipids, calcium, and other elements within the intima, leading to the formation of a plaque with complex structure as represented in Figure 1.2. Risk factors such as excessive consumption of tobacco, fatty food causing excessive cholesterol in the blood, stress, genetic predisposition, diabetes, and lack of exercise contribute to its development, eventually leading to symptoms that can have serious consequences<sup>13</sup>.

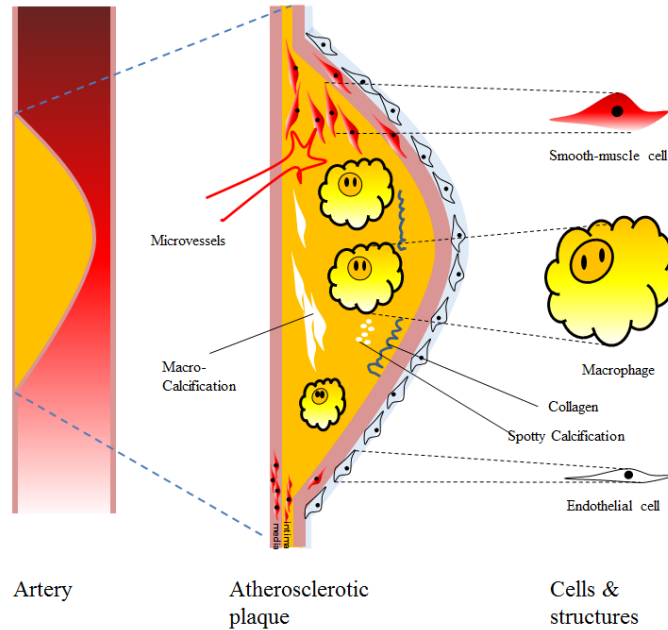


Figure 1.2: Atherosclerotic plaque composition

Atherosclerosis is a disease mainly affecting the elderly, developing over several decades. Given the aging population and dietary habits in developed countries, several authors have suggested that this disease is the disease of the 21st century<sup>14,15,16</sup>. This is a complex disease in which the initiation and evolution are still not fully understood<sup>17</sup>.

Low density lipoproteins (LDL) are absorbed directly through the endothelial layer of the intima. The intima layer thickens around the lipid core (atheroma) and the fibrous tissue resulting as a consequence of the inflammation. The thickened intima with its lipid core and surrounding fibrous tissue is called an atherosclerotic plaque. Arterial remodeling takes place, and the final result is a compact layer containing primarily collagen and smooth muscle cells, with some contribution of additional matrix proteins. The lipid core does not contain only lipid. It is also a complex tissue containing many

constituents, including lipoproteins, triglycerides, foam cells, leukocytes and macrophages<sup>18</sup>...

The formation of calcifications may occur during plaque growth. Calcification of plaques can be caused by either genetic factors or by smooth muscle cells and macrophages that have become calcified after undergoing apoptosis while crossing the fibrous cap in their migration into or out of the necrotic lipid core. The calcifications could then be found in both atherosclerotic plaque cap and lipid core<sup>19</sup>.

### **III –Role of collagen in extracellular matrix**

Collagen is an important component of the extracellular matrix of the arterial wall. Studies have shown that the amount and organization of matrix collagen is related to the mechanical stability of the fibrous cap<sup>20</sup>. Collagen is the most abundant fibrous protein and satisfies a variety of mechanical functions, particularly in mammals. It is present in skin, cartilage, arteries and in most of the extracellular matrix in general<sup>21</sup>. There are at least 28 genetically distinct types of collagen<sup>22,23</sup>. They can be grouped into a number of subfamilies (Table 1.1). From the biomechanical point of view, the fibrillar collagens are of most interest<sup>24,25</sup>. The fibrillar collagens are defined as a family of structurally related collagens that form the characteristic collagen fibril bundles seen in connective tissue. Fibrillar collagen is a critical component of atherosclerotic lesions. Uncontrolled collagen accumulation leads to arterial stenosis, while excessive collagen failure combined with inadequate synthesis weakens plaques, making them prone to rupture<sup>26</sup>.

Table 1.1: Collagens and collagen-like proteins in vertebrates

Sub-family	Members
Fibrillar collagens	Types I, II, III, V, XI, XXIV and XXVII
Fibril associated and related collagens	Types IX, XII, XIV, XVI, XIX, XX, XXI and XXII
Beaded filament forming collagen	Type VI
Basement membrane and associated collagens	Type IV, VII, XV and XVIII
Short chain collagens and related proteins	Types VIII and X; C1q; hibernation-related proteins HP-20, HP-25 and HP-27; emilins 1 and 2; adiponectin; CTRPs 1-7; inner ear (saccular) collagen
Transmembrane collagens and collagen-like proteins	Types XIII, XVII, XXIII and XXV/CLAC-P; ectodysplasins; macrophage scavenger receptors I-III; MARCO; SRCL; gliomedin; CL-P1
Collectins and ficolins	Mannan binding protein; surfactant proteins A and D; conglutinin; CL-43; CL-46; CL-L1; CL-P1; L-, M- and H-ficolins
Other collagens and collagen-like proteins	Emu1; collagen XXVI/Emu2; collagen XXVIII; acetylcholinesterase tail subunit

Human atherosclerotic plaques contain mostly fibrillar collagen types I and III<sup>27</sup>. Type I collagen itself comprises approximately two-thirds of the total collagen<sup>28</sup>. Type V collagen also increases in advanced atherosclerotic plaques<sup>29</sup>. Thick type IV collagen depositions are frequently seen in the fibrous cap regions<sup>27,29,30</sup>.

Type VIII collagen is considered a short-chain collagen (subgroup of non-fibrillar collagens). It may serve different functions such as stabilization of membranes, and interactions with other extracellular matrix molecules. It is found in basement membranes where it plays a role as a molecular bridge between different types of matrix molecules<sup>31</sup>, including in ECM of atherosclerotic plaques. Lopes et al. 2013 showed that Type VIII collagen mediates fibrous cap formation in atherosclerosis<sup>32</sup>.

#### IV – Conclusion

Studying plaque stability is challenging. Therefore, it is important to understand plaque formation and composition from a biological point of view. But plaque rupture is a mechanical process that needs to be also studied as a mechanical problem. In the next

section, some important mechanical concepts will be presented in order to use them later to have a better understanding of plaque rupture mechanisms.

## Section 2 – **Mechanical introduction**

### I – **History and Griffith theory**

From a mechanical point of view, our medical problem will be solved using fracture mechanics laws. In this part we will introduce as simply as we can fracture mechanics in general.

In 1920, A.A. Griffith started his work on fracture mechanics considering that the theoretical strength of a material was taken to be  $E/10$ , where  $E$  is the Young's Modulus for the particular material. He was only considering elastic, brittle materials, in which there is no plastic deformation. A lot of experimental tests were done since then to study the critical strength, and it was observed that these critical strength values (strength before failure) were 1000 times less than the predicted values. Griffith wished to investigate this disagreement. He discovered that there were many microscopic cracks in every material and hypothesized that these small cracks actually are responsible for this difference. The presence of these cracks lowered the overall strength of the material because of the increased stress concentration when a load is applied.

Griffith used the energy approach to deduce the energy release rate  $G$ , using the first law of thermodynamics. This law implies that during the passage from a non-equilibrium state to an equilibrium state, there is a net decrease in energy. Based on this idea, Griffith explained the formation of a crack. A crack can form or extend only if a process does not increase the total energy. Thus the critical conditions for fracture can be

defined as the point where crack growth occurs under equilibrium conditions, with no net change in total energy.

The Griffith energy balance for an incremental increase in the crack area under equilibrium conditions can be expressed by: (Eq. 1.1)

$$\frac{dE}{dA} = \frac{dSE}{dA} + \frac{dW_s}{dA} \quad (1.1)$$

Where:

E: total energy.

SE: potential energy supplied by the internal strain energy and external forces.

Ws: work required to create new surfaces.

The energy release rate  $G$  is defined as a measure of the energy available for an increment of crack extension (Eq.1.2)

$$G = \frac{dE}{dA} - \frac{dSE}{dA} \quad (1.2)$$

So  $G$  measurements can define a fracture parameter, which is the energy release rate during the dissection phase; the challenging part is to measure experimentally the  $G$  values.

## II – Cohesive models

Delamination is defined as the act of splitting or separating a laminate into layers. Delamination along an interface plays a major role in limiting the toughness and ductility of multi-phase materials. This motivated considerable research on the separation of interfaces using finite element models. Delamination of the interface can be modeled by traditional methods such as nodal release techniques. On the other hand, it is possible to use other techniques that simulate failure by adopting relations between tractions and separations, and introducing a critical fracture energy representing the energy required to separate the interface between surfaces. This technique is called the simulation by cohesive zone model (CZM). The definition of traction-separation laws used depends on the choice of elements and the surrounding material behavior. Generally, the traction-separation law  $T = f(\delta)$ , cannot be identified directly. Most of the traction-separation laws used in the literature contain at least two parameters: the cohesive strength  $T_0$  and the critical separation  $\delta_f$ <sup>33</sup>. It has been shown that the shape of the law has an effect on crack propagation even if the same  $T_0$  and  $\delta_f$  are used<sup>34</sup>. A bilinear traction-separation cohesive law is considered here. Figure 1.3 depicts this law. It shows linear elastic loading (OA), followed by linear softening (AB). The normal maximum contact traction is reached at point A and denoted as  $T_0$ . Separation starts at point A and ends at point B when the normal contact traction reaches zero. The area under the OAB curve is the energy released due to complete separation, which is termed the critical fracture energy per unit area. It is assumed that separation is cumulative and that any unloading/reloading cycle induces a purely elastic response along line OC.

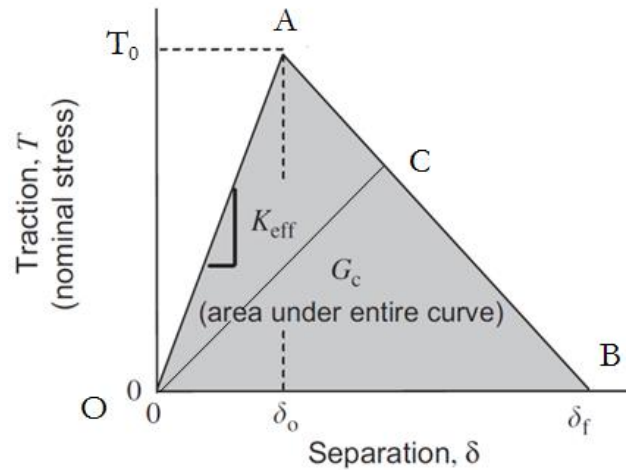


Figure 1.3: Traction/separation schematic curve for bilinear cohesive zone models

The parameters of the bilinear traction/separation cohesive law to be characterized are:  $K_{\text{eff}}$ (MPa/mm),  $T_0$ (N/mm) and  $\delta_f$  (mm).

### III –Mechanical properties of arterial and atherosclerotic plaque components

Smooth muscle cells, elastin and collagen fibers are considered as the main structural components of the different layers of the artery.

Elastin fibers have a linear elastic behavior with a Young's modulus on the order of 1 MPa<sup>8,9</sup>. However, due to the presence of collagen fibers, the arteries have a strongly nonlinear behavior with a rigidity that tends to increase with the applied mechanical load. Three zones are generally considered on the stress-strain curve of an artery (Figure 1.4).

Smooth muscle cells play an important role in the mechanical response of the tissue. The vessel tends to contract from a wall pressure threshold, and to relax from a shear stress threshold applied to the arterial wall<sup>35</sup>.

The vast majority of studies on the mechanical behavior of arteries use a hyperelastic model and define an elastic strain energy function, logarithmic, polynomial or exponential<sup>7,36</sup>. Burton<sup>37</sup> showed that the intima makes a very small mechanical contribution, which could be expected given the low thickness of this layer. The other two layers are the media and the adventitia. Both provide the majority of resistance and mechanical behavior.

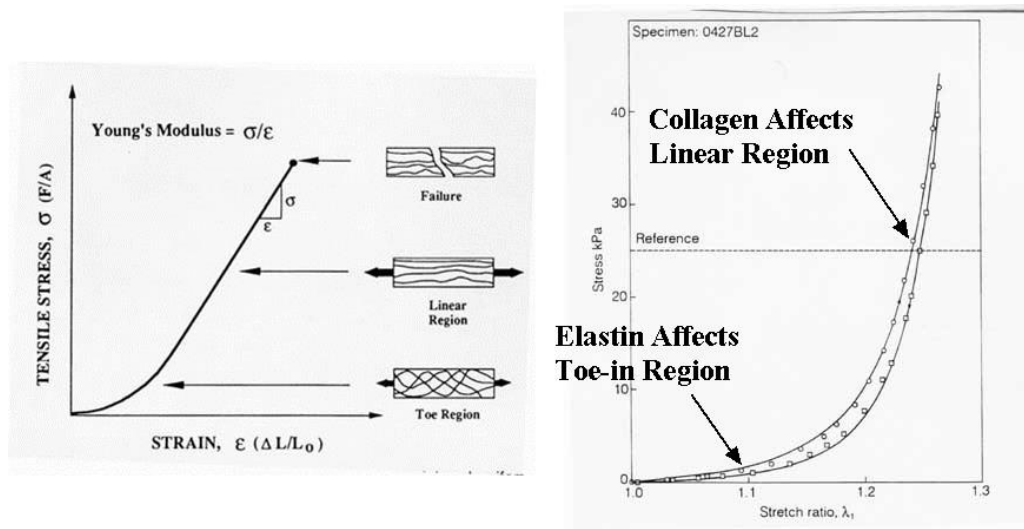


Figure 1.4: Stress Strain arterial response

In 1967, Sacks and Thicker measured different elastic moduli between the radial, circumferential and axial directions on canine femoral arteries<sup>38,12</sup>. These studies therefore suggest that the behavior of arteries is anisotropic. A system is called anisotropic when the mechanical properties are dependent on the considered direction. This property was confirmed two years later by Patel et al. who worked on the carotid arteries of dogs and showed that the circumferential direction of the artery was generally stiffer than the axial direction<sup>39</sup>. The mechanical behavior of arteries could be modeled by

three groups of mechanical properties, depending on the axial, radial, and circumferential directions. One of the major characteristics of the vessels is the existence of circumferential residual stresses. This phenomenon can be observed directly by cutting an artery radially: the ring opens naturally as residual stresses are released. In vivo, it seems that the stress level across the arterial wall is offset in large part by blood pressure<sup>7,40</sup>. It is known that the residual stresses are a result of growth and permanent remodeling of the artery. Saini et al.<sup>41</sup> showed that the elastin fibers are the main element responsible for these residual stresses, although it has been proven that collagen fibers also play an important role<sup>42</sup>.

Many studies have confirmed this observation of the existence of residual stresses in the arterial wall<sup>43,44,45,7</sup>. Chuong and Fung<sup>40</sup> suggested that it was possible to quantify the residual stresses by measuring the opening angle of the artery once cut radially. The problem is more complex in reality as it has been shown that opening angles are different between the media and adventitia layers<sup>46,47</sup>, and even between the external and internal parts of the media<sup>48</sup>. Many other authors have proposed computational strategies to predict the stresses in arterial wall<sup>49</sup>.

#### **IV – Conclusion**

To study plaque separation from a mechanical point of view, mechanical laws should be used depending on the mechanical process. In layer separation problems, fracture mechanics is the field of interest. In the case of experimental work, it is important to understand the Griffith theory. And in numerical work, cohesive zone models can be

implemented to model the separation and to understand dissection properties. In the next section, a state of the art literature review is presented to show how these mechanical principles and laws have been applied to biological tissues to study arterial dissection or atherosclerotic plaque rupture.

### **Section 3 – State of art and literature review**

#### **I – Arterial dissection**

Arterial dissection may lead to serious complications such as myocardial ischemia, ischemic stroke and other fatal consequences<sup>50,51</sup>. It begins with an intimal tear that propagates into the vessel wall and leads to the creation of a false lumen<sup>51</sup>. Separation could occur between the intima and the media, between the media and the adventitia, or within layers (intima and media)<sup>52</sup>.

Many factors contribute to arterial dissection such as elastin fragmentation, loss of smooth muscle cells, atherosclerosis, and hypertension<sup>52,53</sup>. 60% of coronary artery dissection cases occur in the left anterior descending coronary, and coronary atherosclerosis is one of the most frequent pathologies leading to coronary artery dissection<sup>54</sup>.

In order to better understand the mechanical process of dissection, many studies have been realized in which the dissection strength between different interfaces was measured<sup>51,55,56</sup>. Wang et al. 2014, were interested in the LAD (Left Anterior Descending) coronary artery, since no data had previously been reported in the literature<sup>3</sup>. This study used peeling tests to characterize the adhesion strength for dissection within medial and intimal layers. The peeling test was designed to measure the dissection strength at

different interfaces within the arterial wall in terms of local energy release rate, **G**. This method gave quantitative data that helped to provide a better understanding of arterial dissection mechanisms. Histological studies were performed to complement the mechanical tests by confirming the exact dissection locations and examining the microstructural characteristics at the separated surface. The results showed that there is a statistically significant difference in dissection resistance between tearing events occurring within the intima and within the media <sup>3</sup>.

## **II – Plaque rupture mechanisms**

### *A – Histological features of vulnerable plaques*

Several studies have used specimens obtained at autopsy to study the stability of atherosclerotic plaques<sup>57,58</sup> These studies aimed to identify the histological features that distinguish stable plaques from unstable (ruptured) ones. Histological features of ruptured plaques include the following

- A thin fibrous cap (on the order of 65  $\mu\text{m}$  thick);
- A large lipid core (>40% of plaque volume);
- Angiogenesis within the plaque;
- Decreased collagen content in the fibrous cap;
- Increased inflammatory cell content;
- Outward vascular remodeling.

The thin-cap fibroatheroma (TCFA) is widely considered to be the type of plaque most likely to rupture. It is characterized by a fibrous cap  $< 65 \mu\text{m}$  thick, which is heavily infiltrated by macrophages. Typically, a TCFA has a large, lipid-rich necrotic core, which contains numerous cholesterol esters, free cholesterol, phospholipids, triglycerides and apoptotic macrophage foam cells, lying between the thin fibrous cap and the media<sup>57,59</sup>. Many studies used mouse atherosclerotic plaque models and showed that their plaques are less susceptible to rupture than human plaques<sup>60</sup>. Despite this, mouse plaque models are widely used. A lot of similarities were noticed in advanced atherosclerotic plaques in mouse models with advanced human plaques<sup>60,61</sup> even if more recent studies had shown that mouse biomechanical properties of plaques and artery size give less propensity to rupture comparing to humans<sup>62</sup>.

#### *B – Role of circumferential tensile stress in plaque rupture*

While histological features remain qualitative data, measuring fibrous cap tensile strength was the subject of many studies aiming to quantify plaque stability. These studies were interested in calculating tensile stresses using 2D finite element models, in combination with histology to estimate the vulnerable geometry in human atherosclerotic plaques<sup>58,63,64</sup>. It is also possible to separate individual layers from plaques and to identify the mechanical properties of the layers (intima & fibrous cap)<sup>65</sup>. The mechanical properties of lipid pools were also estimated based on lipid composition in human plaques<sup>66</sup>. FE analysis of human atherosclerotic plaques has shown that the areas of greatest circumferential tensile stress are generally located at the plaque shoulder, defined as the boundary between the fibrous cap and the adjacent normal wall. It is important to note that these results are related to lesions which have a large necrotic core and a thin

fibrous cap<sup>58,63,64</sup>. This prediction corresponds to clinical observations concerning the most frequent location of plaque ruptures. More observations suggest that additional factors, both biological and mechanical, must be involved to have a better understanding of plaque rupture. For example, it has been found in some numerical studies calculating the maximum circumferential tensile stresses in human plaques that the values were usually different than the failure strengths measured experimentally. Static 2-D finite element analysis underestimated by at least a factor of two the experimentally measured ultimate tensile stresses of tissue strips, suggesting that stresses experienced in vivo would not reach the levels required for plaque rupture<sup>63,65</sup>. More recent work by Holzapfel and colleagues has shown that there is significant anisotropy in the mechanical properties of the fibrous cap, with lower ultimate tensile stresses measured in the circumferential direction than in the axial direction<sup>67</sup>. The measure of the shear strain elasticity (SSE) was also used as an indicator to identify vulnerable plaques<sup>68</sup>, if the absolute value of the SSE is high, the plaque is more vulnerable. The same group has developed an intravascular ultrasound elasticity reconstruction method to have a predictor of plaque vulnerability<sup>69</sup>, and designed a technique to get strain fields and modulograms for the recorded intravascular ultrasound sequences, in order to have quantitative data taking into account the motion of the heart and therefore better predictions of plaques vulnerability<sup>70</sup>.

In conclusion, these observations suggest that additional factors, both biological and mechanical, must be considered in plaque rupture studies.

### *C – Fatigue and fracture mechanics*

Many other factors than those listed above could play a major role in plaque stability, such as calcification in the fibrous cap or the lipid core<sup>19,71</sup>. Using finite element analysis, Weinbaum and colleagues have recently shown that microscopic calcifications in the fibrous cap could lead to local stress concentrations which might exceed the mechanical strength of the material<sup>19</sup>. Material fatigue may play a significant role in plaque rupture, but this factor has received limited attention<sup>71,72</sup>. Atherosclerotic plaques are subject to cyclical pressure loading as a function of the normal cardiac cycle in vivo. Plaques in certain locations, such as the coronary arteries, also may experience cyclic tensile loading due to changes in the geometry of the heart as it contracts and relaxes. Clinical observations have shown an increased risk of acute cardiovascular events with increases in pulse pressure, consistent with the idea that material fatigue contributes to plaque instability<sup>72</sup>.

From a fracture mechanics point of view, few studies have attempted to characterize plaque rupture properties. Holzapfel's group has measured forces required to delaminate the normal human aortic media<sup>51</sup>. Recently, Pasta and colleagues<sup>56</sup> have also measured fracture properties of human aortic media in order to better understand aneurysm rupture mechanisms. Several studies carried out by the Gasser group used the cohesive elements technique in numerical models to represent the propagation of arterial dissection<sup>73</sup>. The cohesive zone model (CZM) captures the dissection properties of the individual arterial tissues. Gasser assumed the existence of a cohesive zone in which initialization and coalescence of micro-cracks are lumped into a discrete surface, based on the elasto-plastic fracture theory of metals<sup>74,75</sup>, and on the quasi-brittle fracture theory of concrete<sup>76</sup>. In his study of plaque dissection during balloon angioplasty, Gasser defined

the dissection as a gradual process in which cohesive traction resists separation between adjoining material surfaces. The presence of collagen in arterial layers motivated the use of this cohesive concept. These studies used a novel cohesive zone model with a defined traction separation law in their finite-element simulation to predict that, in the primary phase of material failure, the plaque breaks at both shoulders of the fibrous cap, with initial crack growth being stopped at the internal elastic lamina. In the secondary phase, local dissections between the intima and the media develop at the fibrous cap location with the smallest thickness<sup>77</sup>. However, the pressures acting on the fibrous cap are much greater during balloon angioplasty than under normal physiological conditions<sup>78</sup>. Importantly, plaque failure by delamination has been observed clinically during stenting of atherosclerotic human arteries; although the conditions contributing to delamination during this intervention are also well outside the physiological range.

A survey of the literature on plaque rupture reveals that little attention has been directed toward measuring or modeling plaque attachment to the vessel wall as an adhesive interaction. If successful, our proposed studies will provide evidence for an alternative mechanism of plaque rupture, which does not depend solely on mechanical strength of the fibrous cap. In addition, our computational studies will investigate a range of conditions (material properties, physiological parameters such as blood pressure) that contribute to each mechanism of plaque failure. Understanding the multiple mechanisms of plaque rupture will potentially lead to development of new strategies for clinical intervention to reduce the incidence of this potentially lethal event.

### **III –Conclusion**

Previous biomechanical studies of plaque rupture have focused primarily on the tensile strength of the fibrous cap, rather than on the adhesive strength of the cap/wall interface. We propose in this thesis a novel hypothesis regarding mechanisms of plaque rupture. Specifically, we hypothesize that the adhesive strength of the bond between the plaque and the vascular wall is an important determinant of atherosclerotic plaque stability (resistance to rupture). In the following section, we review the studies which have already been published about adhesive strength evaluation and modelling in biomechanics.

## Section 4 – **Fracture mechanics in soft tissue biomechanics**

### I – **Experiments**

Studies dealing with atherosclerotic plaque delamination as a fracture mechanics problem are rare. The *Lessner* group at the University of South Carolina used fracture mechanics to study coronary arterial dissection and atherosclerotic plaque rupture<sup>3,4</sup>. In these studies, a method was developed and applied to characterize the fracture energy per unit area. In other words, the aim was to characterize the dissection strength at different interfaces within the arterial wall in terms of local energy release rate. Taking a different approach to explore dissection properties, Chu et al. 2013 measured the fracture toughness<sup>79</sup> which is an inherent property describing the ability of a material to resist crack propagation from an existing flaw<sup>80</sup>.

Some studies took into account the effects of fatigue on the aortic wall. It is important to include fatigue effects, especially in the study of spontaneous rupture of the aorta (SRA), since the aorta is subjected to cardiac pressure cycles. Chu et al. 2013<sup>79</sup> hypothesized that fracture toughness as well as the stiffness of a piece of ascending aortic

tissue are separately governed by the amount of cumulative damage present internally, in a purely fatigue-driven environment<sup>79</sup>.

Other studies focused on measurement of the energy required to produce the dissection. Table 1.2 summarizes some of the values of the dissection energy characterized on different samples.

Table 1.2: Dissection energy calculated experimentally for different arterial samples in literature

Reference	Samples	Dissection Energy (J/m <sup>2</sup> )
Carson et al. 1990 <sup>81</sup>	Thoracic aorta	159.0 ± 8.9
Roach & Song 1994 <sup>82</sup>	Upper abdominal aorta	18.8 ± 8.9
Roach & Song 1994 <sup>82</sup>	Lower abdominal aorta	113.4 ± 4.05
Sommer, et al, 2008 <sup>51</sup>	Human abdominal aortic media	76±27 (axial) 51±6 (circumferential)
Tong, et al, 2011 <sup>55</sup>	Human carotid artery	60±16~75±24 (within media)
Wang et al. 2014 <sup>3</sup>	Human LAD coronary artery	20.71±16.47 (within intima) 13.46±7.19 (intima-media interface) 10.31±4.95 (within media)

In summary, we can see that the dissection energy has been characterized for different samples and under different conditions (pathological and healthy cases, for instance). The dissection energy was the major factor measured, since it can be deduced directly from load displacement curves obtained experimentally.

However, refined analyses of the characterized dissection energy are still missing. For example, the contribution of the strain energy to the total energy was never considered. Numerical simulations would offer an interesting possibility to investigate this contribution and its effects, but this has never been done.

## II – Numerical studies

Several studies carried out by the Gasser group used the cohesive elements technique to represent the propagation of arterial dissection<sup>73</sup>. The cohesive material model aims at capturing the dissection properties of the individual arterial tissue. The presence of collagen fibers in arterial layers motivated Gasser to use cohesive zone model to study the separation between biological layers<sup>73</sup>. Thus, damage of fiber bridging was considered to be the cause of a gradual decrease of cohesive force after exceeding the limit load.

Gasser et al. 2006<sup>73</sup> focused on the dissection of the human aortic media in mode I separation. The human aortic media has a highly organized lamellar structure with repeating structural and functional units of elastin, collagen and smooth muscle cells. Based on this lamellar structure, he postulated a cohesive potential per unit area and derived an appropriate traction separation law using the theory of invariants. This law is shown in Figure 1.5. It is composed of two parts; the linear elastic part has stiffness  $C_n$ :  
(Eq. 1.3)

$$C_n = \frac{t_n}{\delta_n} \tag{1.3}$$

And the softening part is defined by the traction separation law (Eq.1.4)

$$t_n = t_0 \exp(-a\delta_n^b) \quad (1.4)$$

Where  $t_n$  is the elastic traction limit of the cohesive zone related to  $\delta_n$ .  $t_0$  denotes the cohesive tensile strength and, the non-negative parameters  $a$  and  $b$  aim to capture the softening response of the tissue according to mode I dissection.

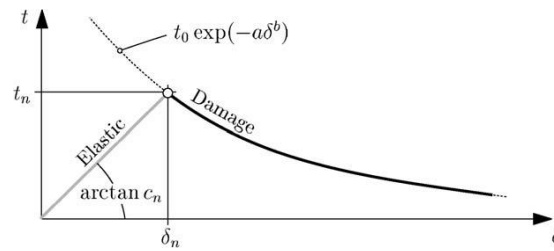


Figure 1.5: Elastic and damage loading stages of the cohesive model: state of damage  $\delta_n$ , elastic stiffness  $c_n$  and elastic traction limit  $t_n$  at  $\delta_n$  defined by Gasser et al. 2006<sup>73</sup>

The experimental evidence of crack propagation shows that the cohesive behavior is different for opening mode (I) and sliding modes (II and III), even in isotropic materials<sup>83</sup>. It is therefore necessary to follow the direction of the crack to distinguish the contribution of the normal and tangential components of the separation (displacement jump). An anisotropic cohesive law, able to distinguish the behavior of the cohesive response along the different directions of the cohesive surface, and an anisotropic fracture criterion were used in this study<sup>83</sup>. The cohesive law used is shown in the Figure 1.6, defining three critical fracture energy values, one for each direction.

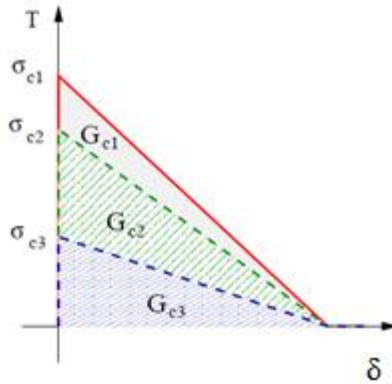


Figure 1.6: Set of cohesive laws considered in the model used in Ferrara et al. 2010 study<sup>84</sup>. Both cohesive strengths and critical energy release rates are scaling proportionally. The maximum opening displacement  $\delta_c$  does not change

In any cohesive law used, characterizing the cohesive parameters is challenging. In Gasser and Holzapfel's study<sup>85</sup>, three parameters had to be determined to characterize the cohesive law :  $t_0$ ,  $a$  and  $b$ . In order to quantify  $t_0$ , experiments carried out by the same group were used<sup>51</sup>. Tensile tests were carried out on circular-shaped specimens along the radial direction and the force displacement curves were measured. According to these experimental data,  $t_0$  was found equal to 140.1 kPa. The value of parameter «  $b$  » (equation 2) used in Gasser's simulations was estimated by assuming that the material is « plastic-like » with  $b=2$ . This value ensures convergence by avoiding a fast decay of the cohesive traction when reaching the cohesive strength, which is typical for quasi-brittle materials. «  $a$  » (equation 2) was deduced using an inverse method. The method consisted of varying «  $a$  » until a force vs displacement curve matching the experimental curves was obtained. «  $a$  » was found to be equal to  $6.5\text{mm}^{-1}$ . Computing the critical fracture energy using these parameters gave a value of  $4.9\text{ mJ/cm}^2$ . According to the values presented in table 1, the value  $49\text{ J/m}^2$  falls within the range of experimentally obtained

values. Ferrara et al.<sup>83</sup> used a simpler cohesive law, and the parameter to be determined was only  $G_c$  (critical fracture energy, which can be deduced directly from the experiments).

An important point to notice in the listed numerical studies was the integration scheme used for simulations. Table 1.3 shows numerical studies using CZM that deal with medical problems in which separation between layers occurs. For each listed study, an inventory of the resolution scheme and the cohesive law used for the model was cited.

Table 1.3: Numerical studies and the resolution scheme chosen for the models

<b>Study</b>	<b>Domain of application</b>	<b>Implicit or explicit</b>	<b>Cohesive Law</b>
<b>Gasser et al. 2003<sup>86</sup></b>	Dissection in soft biological tissues	Explicit	user defined: transversely isotropic traction law in form of a displacement–energy function and assuming that softening phenomena in the cohesive zone are modeled by a damage law, which depends on the maximum gap displacement of the deformation path.
<b>Gasser et al. 2006<sup>85</sup></b>	Modeling the propagation of arterial dissection	Explicit	user defined: Linear elastic part, exponential softening part represented in Figure 1.5
<b>Gasser et al. 2007<sup>77</sup></b>	Plaque fissuring during balloon angioplasty	Explicit	User defined
<b>Ferrara et al. 2008<sup>83</sup></b>	Fracture in human arteries	Explicit	Bilinear traction separation law represented in Figure 1.6
<b>Ferrara et al.</b>	Arterial media dissection	Explicit	

<b>2010<sup>84</sup></b>			
<b>Caballero et al. 2010<sup>87</sup></b>	Kidney stones fragmentation by direct impact	Explicit	bilinear traction separation law
<b>Badel et al. 2014<sup>88</sup></b>	Arterial dissection during balloon angioplasty of atherosclerotic coronary arteries	Implicit (Abaqus/standard)	Linear elastic part, exponential softening part
<b>Untaroiu et al. 2015<sup>89</sup></b>	Biomechanical and injury response of human liver parenchyma under tensile loading	Explicit	Normalized trapezoidal traction-separation relationship
<b>Leng et al. 2015<sup>5</sup></b>	Atherosclerotic plaque delamination in ApoE knockout mouse models	Implicit	User defined

Most numerical work studying dissection or separation problems in biological tissues used the cohesive element technique as represented in Table 1.3, with differences in the choice of cohesive law and its parameters, and the choice of the integration scheme. A bilinear traction separation law was used and accepted in some of these works, and the explicit scheme seemed to be the most frequent choice in CZM, since there is the presence of large deformations and high non-linearity.

### III –Conclusion

The objective of our research is to have a better understanding of two medical problems: arterial dissection and atherosclerotic plaque delamination, using fracture mechanics laws. A review of the literature showed that delamination has always been

under-considered by cardiovascular biomechanicists both experimentally and numerically.

In order to address this lack, experimental and computational work has been achieved in this thesis. The aim of the experimental work is to measure the interlaminar tissue adhesion strength first in human coronary artery specimens and then in a mouse model of atherosclerotic plaques. The aim of the computational work is to identify meaningful constitutive parameters from these delamination tests, as adhesive strength is expected to depend on plaque composition and extracellular matrix organization. The choice of integration scheme in simulations was an important factor to ensure convergence and to respond to the high non-linearity related to this problem.

The manuscript is organized as follows: after this introduction, Chapter 2 presents the numerical method used to identify mechanical properties of arterial layers based on the experimental data obtained by Wang et al. 2014<sup>3</sup>. This chapter also presents a novel use of an inverse method to characterize cohesive parameters of the interface between the layers. In Chapter 3, atherosclerotic plaque delamination will be studied. In Chapter 3, the experimental protocol to identify the energy release rate in two mouse genotypes is presented. These two groups of mice are the ApoE<sup>-/-</sup> vs ApoE<sup>-/-</sup> Col 8<sup>-/-</sup>. The aim is to verify whether or not the absence of Col8 in atherosclerotic plaque would be a factor affecting its stability. In chapter 4, based on the numerical method developed in chapter 2, a finite element model of atherosclerotic plaque is presented, to study the delamination using an explicit scheme and the cohesive zone model.

The whole work is summarized in the flowchart of Figure 1.7.

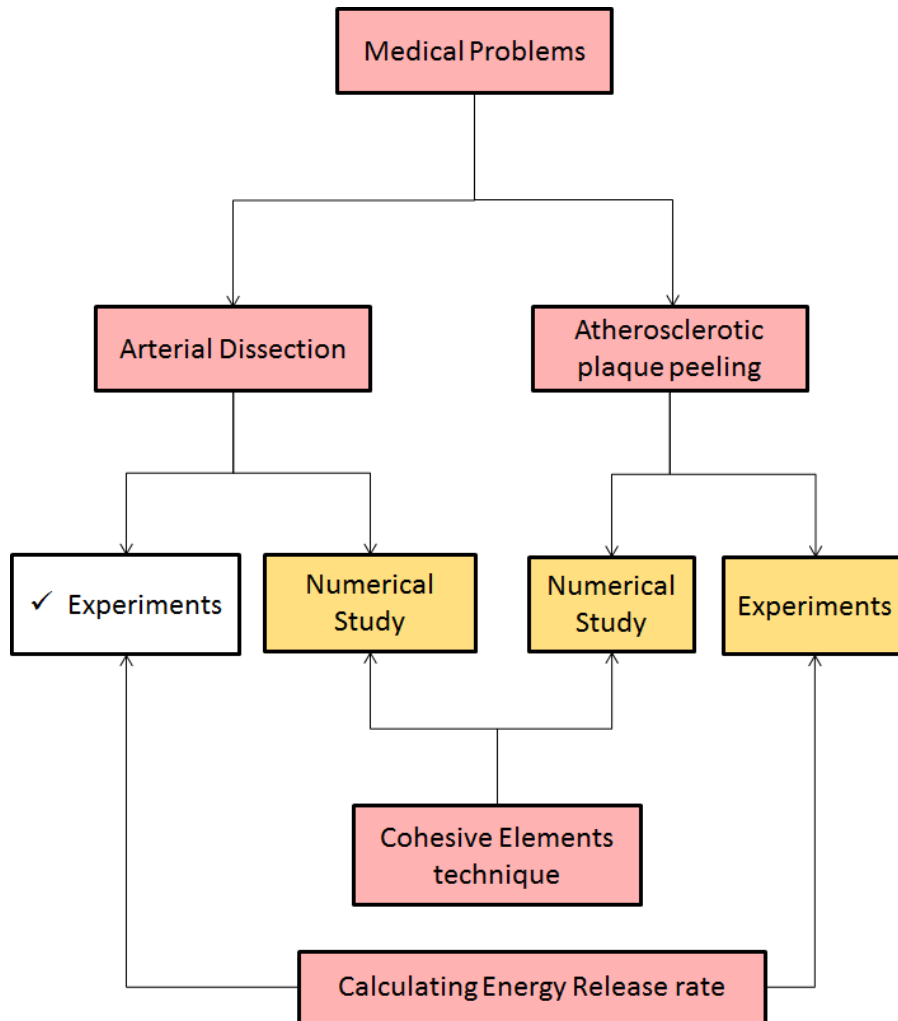


Figure 1.7: Chart representing the work plan for the next chapters

## **CHAPTER 2 ARTERIAL DISSECTION: IDENTIFICATION OF MECHANICAL AND DISSECTION PROPERTIES IN HUMAN CORONARY ARTERIES USING AN INVERSE METHOD**

### ***Abstract***

*The cohesive zone model has been widely used in finite element models to study separation between layers for medical problems. In this study, a 2D finite element model was developed using an implicit scheme and a cohesive zone model (CZM) to test an approach that could help identifying material and cohesive parameters using experimental data. The approach consisted of identifying unknown parameters of the model using an inverse method that related the force-displacement curves obtained experimentally. The method was applied to an arterial dissection problem to have a better understanding of the factors playing a crucial role in the dissection mechanisms. Simulation results showed good agreement between experimental and numerical curves when the correct parameters were identified. However there were some limitations due to the use of the implicit scheme, especially for high energy release rate values. No significant differences in identified cohesive parameters were found between dissection through media and dissection through intima cases. Mechanical properties were different between adventitia layers, and intima-media layers which corresponded to reported values*

*in the literature. Finally, this approach could be used to identify material and cohesive parameters, but the use of an explicit scheme would be more suitable for more complex problems.*

**Keywords:** *Cohesive zone model, arterial dissection, mechanical properties, inverse method, arterial layers*

## Section 1 – **Introduction**

Arterial dissection is a rare but potentially fatal condition in which blood passes through the inner lining and between the layers of the arterial wall. It results in separation of the different layers, creating a false lumen in the process. Arterial walls are composed of three layers, called intima, media and adventitia. Separation could occur between the intima and the media, between the media and the adventitia, or within the intima or media. Coronary arteries are among the arteries most prone to atherosclerotic diseases<sup>90</sup>, which is one of the most common pathologies associated with coronary artery dissection<sup>54</sup>. The left anterior descending coronary artery accounts for 60% of the cases of coronary artery dissection<sup>90</sup>. The different constituents composing arterial layers make the arterial wall a heterogeneous anisotropic tissue. Like most soft tissues, it displays a highly nonlinear behavior, stiffening progressively with increasing applied loads. A study carried out by Eberth et al. 2011<sup>91</sup> was based on the assumption that the arteries are scalable to different changes (pressure, layer thickness, lumen diameter, length...) and in order to estimate the specific implications of these changes, the study used a 4-fiber family constitutive model to quantify the biaxial passive mechanical behavior of mouse carotid arteries.

Gasser and Ogden 2003<sup>92</sup> explained in detail the mechanical behavior of arterial layers and elaborated a constitutive model, denoted Gasser-Holzappel-Ogden model (GHO model), taking into account the different orientations of fibers constituting the arterial wall layers<sup>93</sup>. Holzappel et al. explained that biological soft tissues, more precisely the arteries, present preferred directions in their microstructure<sup>92</sup>. When these materials are subjected to small strains (less than 2-5 %), their mechanical behavior can usually be adequately modeled using conventional laws of linear anisotropic elasticity<sup>94</sup>. However, under finite deformations, these materials have an anisotropic and nonlinear elastic behavior due to rearrangements in the microstructure, such as reorientation of fibers with the directions of deformation. The simulation of these non-linear effects in finite deformation calls for more advanced constitutive models formulated within the framework of anisotropic hyperelasticity. Hyperelastic materials are described in terms of a strain energy function, which defines the energy stored in an elastic material per unit volume of reference (volume in the initial configuration) in terms of deformation at a given point in the material<sup>92,93,94</sup>.

From a biomechanics point of view, the process of dissection can be thought of as a delamination process, and it is defined as separation along the interface. Delamination plays a major role in limiting the toughness and ductility of multi-phase materials, making this particular problem a medical and a mechanical problem that needs to be studied. This has motivated considerable research on the separation of interfaces<sup>94</sup>. Several studies performed by Gasser's group used the cohesive elements technique to represent the propagation of arterial dissection<sup>85</sup>. The cohesive material zone model aims at capturing the dissection properties of individual arterial tissues. Gasser assumed the

existence of a cohesive zone in which initialization and coalescence of micro-cracks are lumped into a discrete surface, based on the elasto-plastic fracture theory of metals<sup>74,75</sup>, and on the quasi-brittle fracture theory of concrete<sup>95</sup>. In his study, Gasser defined the dissection as a gradual process in which separation between surrounding material surfaces is resisted by cohesive traction. The presence of collagen in arterial layers motivated the use of this cohesive concept.

However, there is still a lack of information concerning the mechanical process of dissection, and the factors and parameters that should be taken into account to have a better understanding of the process. The main aim of this chapter is exploring dissection properties for arteries, by creating a 2D model simulating dissection and using the cohesive element technique. An inverse method will be implemented, consisting in calibrating a 2D model able to simulate the dissection through different arterial layers in order to identify the constitutive and dissection properties of human LAD coronary arteries tested by Wang et al. 2014<sup>3</sup>. This identification would help in understanding the factors that play a crucial role in the dissection mechanism.

## **Section 2 – Materials and Methods**

### **I – Experiments**

Experiments performed by Wang et al. 2014<sup>3</sup> aimed at characterizing the dissection strength at different interfaces within the arterial wall in terms of energy release rate  $G$  (N/mm).

Human coronary artery specimens tested were mounted on a plate. The plate was connected to the load cell of the Bose ELF 3200 for load data recording. A small delamination (notch) at the proximal end of the specimen was created and gripped by a

pair of micro-clamps connected to the Bose ELF 3200 actuator (Figure 2.1). The actuator was controlled using computer commands, allowing loading and unloading cycles to be applied to the upper tongue with a horizontal displacement condition.

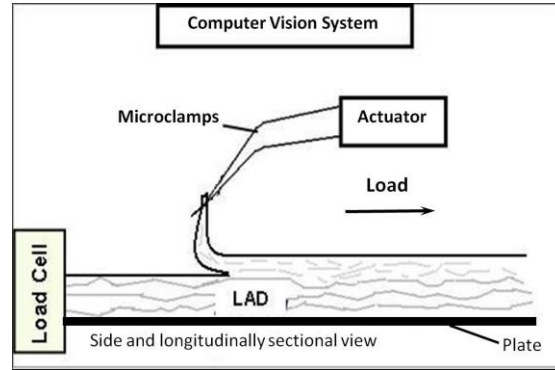


Figure 2.1: Schematic of the delamination process (longitudinal view)

Each loading-unloading cycle generated newly exposed area. Images were taken before and after a peeling cycle to obtain the corresponding newly exposed area  $\Delta A$ .

Figure 2.2 shows the first recorded load-displacement cycles during the delamination event for one of the cycles on one sample. The area enclosed by the loading and unloading curves is the fracture energy  $\Delta E$  from the current peeling cycle (Figure 2.2).

Using measured load-displacement curves, the fracture energy  $G$  was calculated using Eq. 2.1.

$$G = \frac{\Delta E}{\Delta A} \quad (2.1)$$

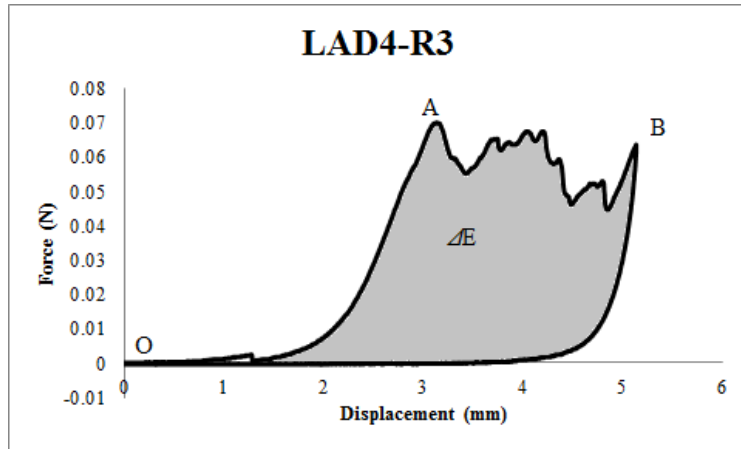


Figure 2.2: First cycles (Load vs Displacement) obtained for one sample (LAD4-R3)

The load displacement curves obtained experimentally were composed of 3 parts representing a full loading-unloading cycle, composed of OA, AB and BO as represented in Figure 2.2 for the sample LAD4-R3. OA represents the initial ramp corresponding to the elastic energy associated with the deformation of the plaque prior to the separation event. Using this first part, an inverse method will be applied to characterize the elastic material properties in the Model 1 section. AB and BO represent the separation and the unloading. The whole curve will be used in the Model 2 section where the cohesive elements will be used to characterize the cohesive parameters and model the dissection.

## II – Numerical model: characterization of material parameters

### *A – Geometry and boundary conditions*

A 2D model was used in this work. The length of all the specimens varied between 14 and 24 mm. The effect of the variation in length between these 2 values was negligible as proved in a preliminary numerical analysis for 4 lengths between 14 and 24 mm, so one model with the same length was used. The average value was 16 mm.

The width of the sample was measured using pictures taken during the experiments for all the samples and the values are reported in Table 2.1.

Table 2.1: Width values for the different specimens used (mm)

<b>Samples</b>	<b>Width (mm)</b>
<b>LAD4-R3</b>	5.6
<b>LAD6</b>	4
<b>LAD10-S1</b>	5
<b>LAD11-S3</b>	8

<b>LAD17</b>	8
<b>LAD19-S2</b>	6
<b>LAD23</b>	4

For each sample, the entire specimen was estimated to have an average thickness of 0.45 mm. Figure 2.3 shows a histological picture of one of the samples tested with the three layers adventitia, media and intima.

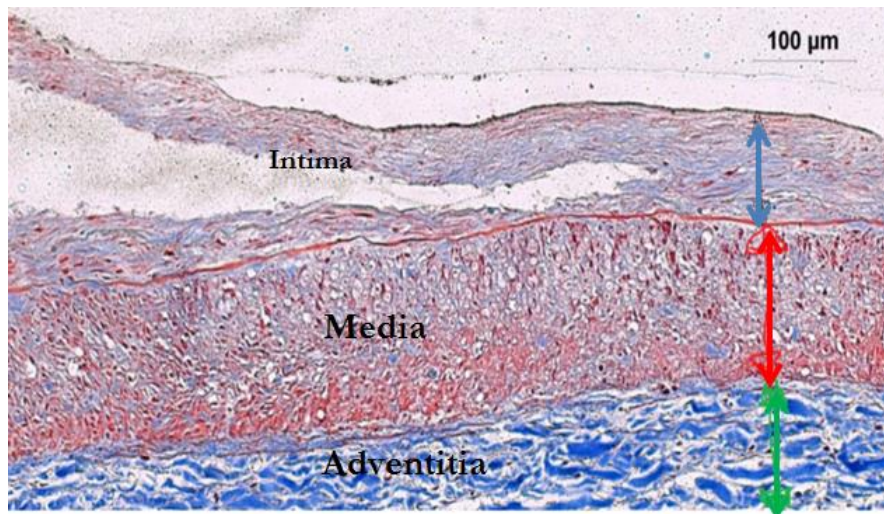


Figure 2.3: Histological picture showing the three layers media, intima and adventitia. The average thickness was evaluated and reported in Table 2.2.

Table 2.2: Thickness of the three layers composing the sample

	<b>Thickness (mm)</b>
<b>Adventitia</b>	0.1
<b>Media</b>	0.25
<b>Intima</b>	0.1

In order to simulate the initial flaw, a material separation was created at the left edge between the dissected layers before beginning the peeling simulation, defining an upper edge (where the displacement boundary conditions will be applied for the simulations), and a lower edge. The lower edge and the right edge were clamped as shown in Figure 2.4. The initial flaw shown in Figure 2.4 was created through the media; another model was also created where the initial flaw was created within the intima to represent experimental cases.

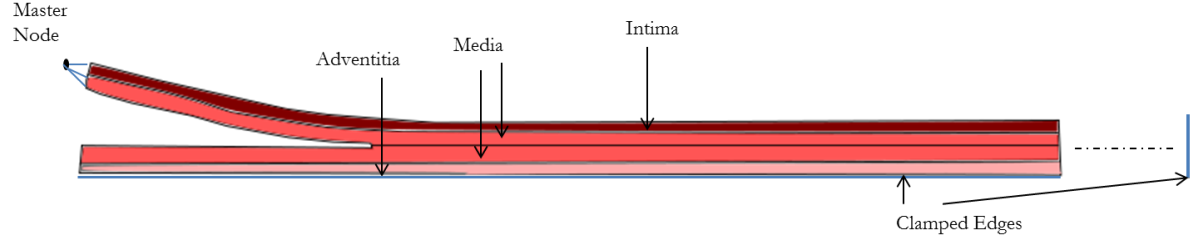


Figure 2.4: Simplified representation of the 2D model used to simulate the dissection through the media

In the finite element model, a master node was created to drive the slave nodes on the upper left edge where the displacement control conditions were applied. The simulations were run in 2 steps. In the first step, a vertical displacement was applied on the master node to move the upper arm to a vertical position, allowing at the same time free horizontal displacement and free rotation. Once the vertical position was reached, a second step was applied consisting of a horizontal displacement in the dissection direction; the vertical displacement was set equal to the value reached in step 1 and a free

rotation was still allowed. This step simulated the dissection phase where the data (force displacement curves) were collected.

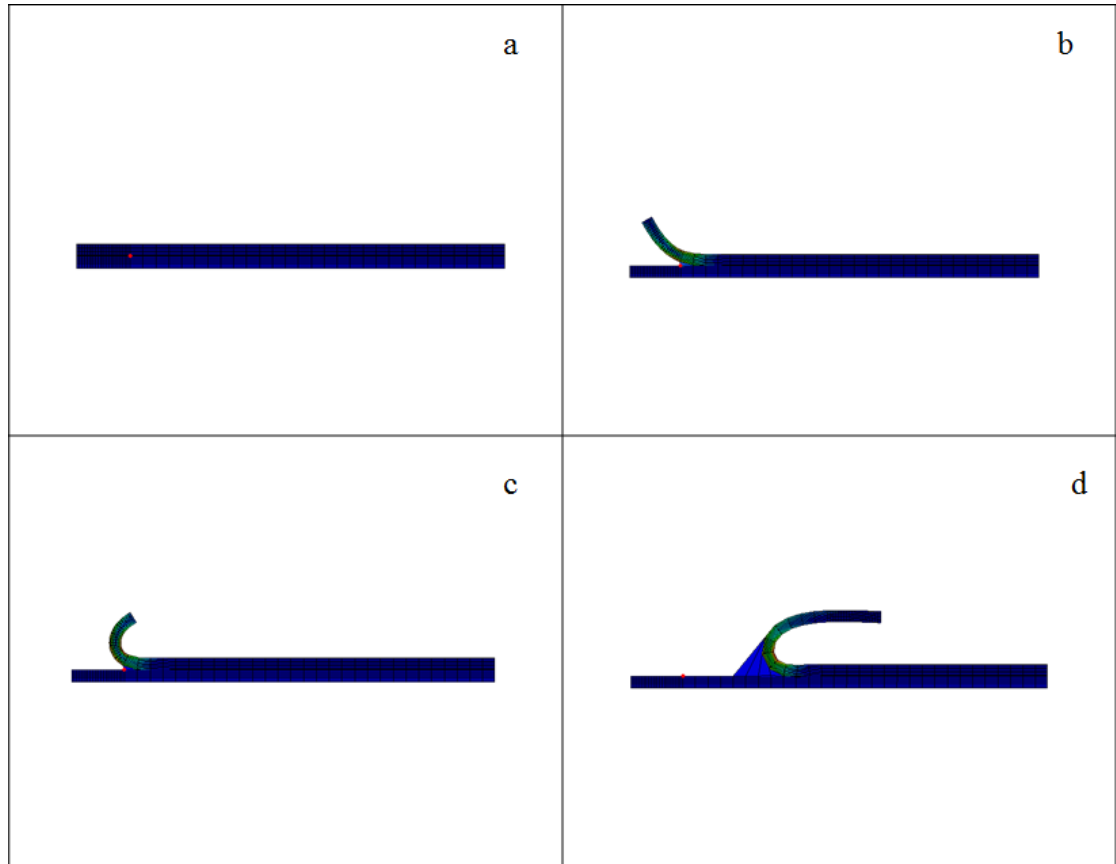


Figure 2.5: Simulation of the peeling test at 4 different times throughout the test

The geometry was meshed using plane strain quadrilateral elements. The cohesive zone was meshed using only quadrilateral structured elements of cohesive type. After trying different mesh sizes for the plaque and media (0.01, 0.025, 0.05 mm), it was found that a mesh size set equal to 0.05 mm gives acceptable results within a reasonable computational time (less than 2% error when compared with the 0.01mm mesh). The mesh size for the plate underneath the plaque was larger since this zone was kept rigid in this problem.

### *B – Material model*

A simplified neo-Hookean model was used in several studies<sup>96,97</sup> to represent the response of the isotropic medium, in the absence of collagen fiber recruitment. The strain energy function for a neo-Hookean model is represented by:Eq.2.2

$$\Psi = C_{10}(\bar{I}_1 - 3) + \frac{1}{D_1} (J_{el} - 1)^2 \quad (2.2)$$

Where  $C_{10}$  represents the neo-Hookean parameter characterizing the shear modulus,  $\bar{I}_1$  represents the first deviatoric strain invariant,  $D_1$  is the parameter related to compressibility and  $J_{el}$  is elastic volume ratio. Then, the first part of the equation represents the isotropic isochoric behavior and the second part represents the compressibility behavior.

The Neo-Hookean model seems to be used and accepted for small strains, and requires fewer parameters<sup>98,99</sup>. In addition, in cohesive zone problems, the elastic properties of the wall are of secondary importance with respect to the cohesive properties<sup>100</sup>. The Neo-Hookean law will be used in our approach to characterize the mechanical properties of the different arterial layers corresponding to the dissection experiments carried out by Wang et al. 2014<sup>3</sup>.

The cohesive law used represents a bilinear traction separation cohesive law. It shows linear elastic loading (OA), followed by linear softening (AB) (Figure 2.6). The normal maximum contact traction is reached at point A defined as  $T_0$ . The separation starts at point A and ends at point B when the normal contact traction reaches zero. The

area under the OAB curve is the energy released due to complete separation and is called the critical fracture energy. It is assumed that separation is cumulative and that any unloading/reloading cycles induce a purely elastic response along line OC.

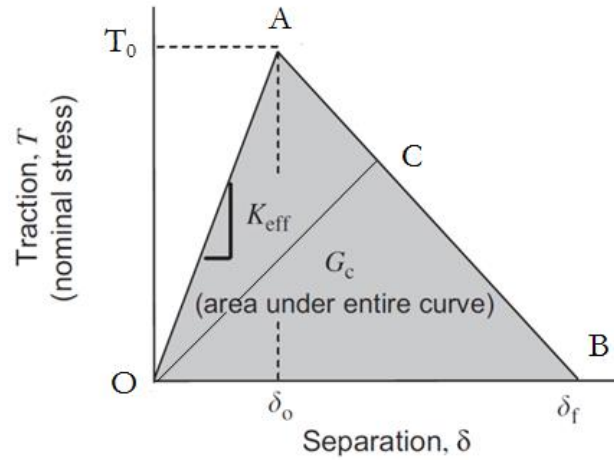


Figure 2.6: Traction/separation schematic curve for Bilinear Cohesive Zone models

The parameters of the bilinear traction separation cohesive law to be characterized are  $(K_{\text{eff}}(\text{MPa/mm}), T_0(\text{N/mm}), \delta_f(\text{mm}))$ . Knowing that  $T_0$  and  $\delta_f$  are related by Eq.2.3:

$$G = \left(\frac{1}{2}\right) \times T_0 \times \delta_f \quad (2.3)$$

If  $G$  is given as an input, then characterizing both parameters  $T_0$  and  $K_{\text{eff}}$  is sufficient.

### *C–Inverse method*

Three main parts composed the loading unloading curves as shown in Figure 2.2. The zero phase (before any load increase) showed important variations between all the

cycles. This variation was thought to be linked to the variation of the notch length created before applying the test. So, the notch length in this case could not be considered the same for all samples. The length ' $l$ ' was then considered as a fourth parameter to be identified in this study with the three Neo-Hookean parameters.

Mechanical properties of materials and cohesive parameters were determined using an inverse analysis, with a Neo-Hookean hyperelastic material model. The three material properties to identify are  $C_{10}$  *adventitia*,  $C_{10}$  *media* and  $C_{10}$  *intima* ( $C_{10}$  in MPa).  $D_{1(adventitia)}$ ,  $D_{1(media)}$ ,  $D_{1(intima)}$ , will be fixed to  $1 \text{ MPa}^{-1}$  according to the assumption of incompressibility<sup>97</sup>.

Figure 2.2 shows experimental force vs displacement curves obtained after one cycle. These curves were used to validate the numerical model.

The identification of the six parameters (' $l$ ',  $C_{10}$  of the three layers,  $T_0$  and  $K_{\text{eff}}$  for the cohesive zone) was performed in four steps:

Step 1: Characterizing the notch length for each model (first approximation)

As a first approximation for the notch length ' $l$ ', the three layers were considered to have the same  $C_{10}$  parameter which simplifies our identification problem to one material parameter, and one geometrical parameter. The cohesive zone was also considered to be a part of the material so having the same  $C_{10}$ . ' $l$ ' and  $C_{10}$  identified by this approach were approximations to have starting values for the notch length. Then the identified value of ' $l$ ' was considered as ' $l_{\text{initial}}$ ' and  $C_{10}$  was considered as  $C_{10(\text{initial})}$ . The notch length ' $l_{\text{initial}}$ ' was varied between 0.1 and 3 mm with 0.1 increments. Different models were generated with different notch lengths and an inverse method was applied

for each model generated with a different notch length to have a first approximation of ' $l_{initial}$ '. Since the cohesive zone was not considered in this first approach, only the zero-phase and the loading part of the experimental curve were used in this identification (OA in Figure 2.2). An inverse method was applied on each model using an optimization algorithm (lsqnnldn). This consisted in finding the ' $l_{initial}$ ' that minimizes the deviation between the experimental and the numerical curves for the zero phase with the corresponding  $C_{10(initial)}$ .

### Step 2: Characterizing cohesive parameters & $C_{10}$ for the three layers

In this step, the ' $l_{initial}$ ' identified above was used. The three arterial layers were considered identical and having the same mechanical behavior to reduce the number of unknown parameters. The parameters to be identified were then reduced to three, one material parameter ( $C_{10}$ ) and two cohesive parameters,  $T_0$  and  $K_{eff}$ . The inverse method consists in finding the material parameter and the cohesive parameters that minimize the deviation between the experimental and the numerical force-displacement curves. An initial matrix was defined containing all combinations of parameter values,  $X_{initial} = [C_{10}, T_0, K_{eff}]$ . The cost vector was defined by Eq. 2.4:

$$cost_{vector}(j) = F_{sim}(j) - F_{exp}(j) \quad (2.4)$$

Where  $F_{sim}$  represents the force values obtained by the simulations,  $F_{exp}$  represents the interpolated experimental points, and  $j$  defines the index of the simulated point. Then the cost function value was calculated as: (Eq.2.5)

$$cost = \frac{[cost_{vector}(j) \times cost_{vector}^T(j)]}{\overline{F_{exp}}^2} \quad (2.5)$$

To avoid irrelevant solutions, bounds were defined for each parameter.

$C_{10}$ : values between 0.05 and 2 MPa

$K_{eff}$ : The initial stiffness of cohesive elements defined in terms of traction/separation does not represent a physically measurable quantity and is treated as a penalty parameter. The value of this penalty stiffness must be high enough to prevent interpenetration of the crack faces and to prevent artificial compliance from being introduced into the model by the cohesive elements. However, an overly high value can lead to numerical problems<sup>101</sup>. Therefore, the values were constrained within the range [1-30 MPa/mm].

G values for the samples used in this identification were reported by Wang et al. 2014<sup>3</sup> for each cycle. Table 2.3 shows the different G values obtained for the studied cycles and for the different samples.

Table 2.3: G values obtained for cycle 1 from different samples

Sample	G (N.mm)
LAD4-R3	0.025
LAD6	0.014
LAD10-S1	0.014

<b>LAD11-S3</b>	0.0068
<b>LAD17</b>	0.0046
<b>LAD19-S2</b>	0.01
<b>LAD23</b>	0.024

Knowing the G values, and choosing the bounds of  $\delta_f$  between 0.1 mm and 2 mm,  $T_0$  values were automatically calculated. Only  $T_0$  values were represented in the defined matrix.

Figure 2.7 shows an example of the variation of the cost function values with respect to the variation of the cohesive parameter ( $T_0$ ) and the elastic parameter ( $C_{10}$ ).

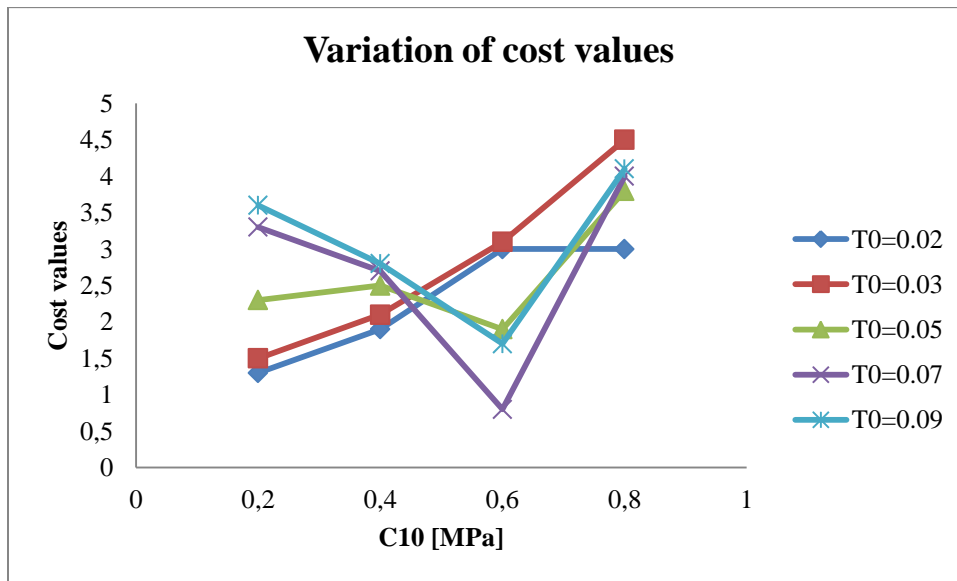


Figure 2.7: Cost function values for LAD6 case with respect to the variation of  $T_0$  (cohesive) and  $C_{10}$  (elastic) parameters

Step 3: Separating individual layer properties ( $C_{10}$  for the three layers)

After identifying the cohesive parameter and one global arterial property corresponding to the minimum cost values obtained, an inverse method was applied using an optimization algorithm (fminsearch) on the three layers (adventitia-media-intima), with the same cohesive parameters obtained previously in order to identify the three parameters  $C_{10}$  related to each layer.

## Section 3 – Results

### I – Notch length characterization

The notch length corresponding to the least deviation between numerical and experimental curves for the zero phase before the deformation process is reported in Table 2.4. The values represented in Table 6 are ' $l_{initial}$ ' obtained after applying step 1 in the inverse approach described in Materials and Methods.

Table 2.4: Notch length corresponding to the minimum error between the numerical and experimental points

Sample	Notch Length (mm)
<b>Dissection through intima</b>	
LAD4R3	1.2
LAD6	2.1
LAD10-S1	0.8
LAD11S3	0.8
<b>Dissection through media</b>	
LAD17	1.1
LAD19	1
LAD23	2.9

These notch length values were then used in the model, and the inverse method was applied to characterize the 3 material parameters (as described in Materials and Methods).

## II –Material parameters

The inverse method was then applied to identify the cohesive parameters and  $C_{10}$  values. Experimental vs numerical curves are shown in Figure 2.8 for dissection through intima, and in Figure 2.9 for dissection through media. They were obtained with the minimum error found for the seven samples.

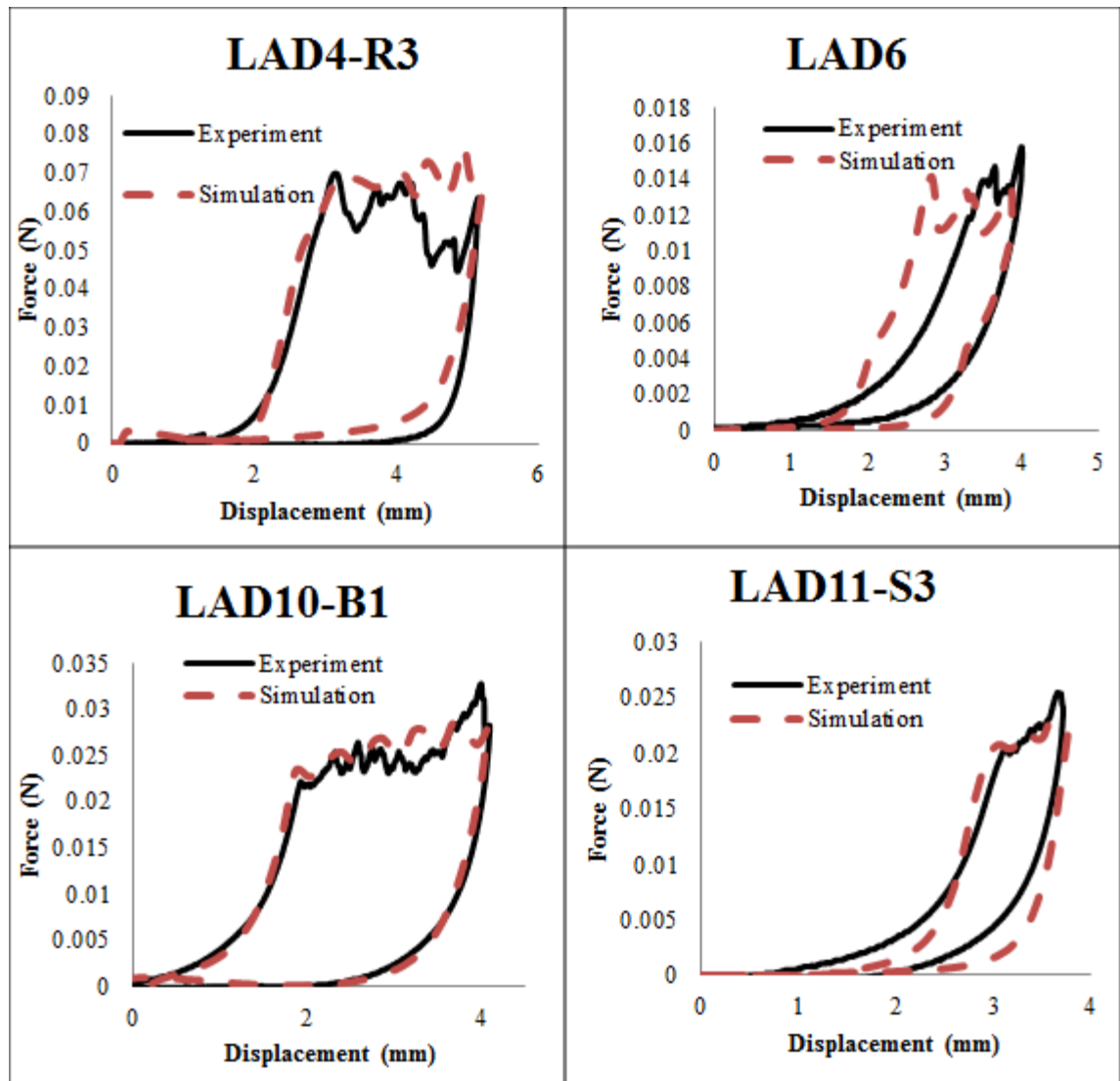


Figure 2.8: Experimental versus simulation curves obtained with the minimum cost value, for samples dissected through the intima

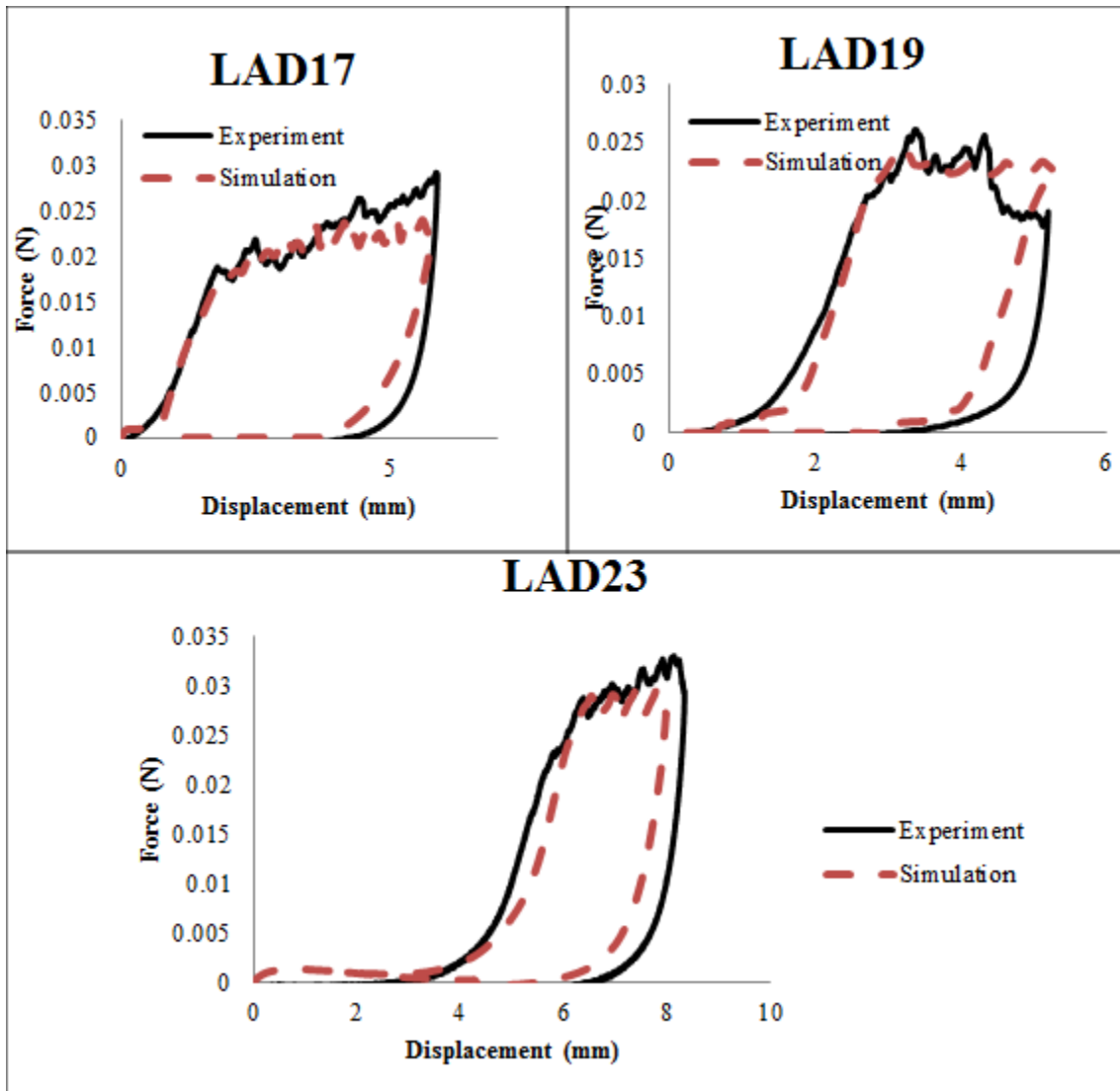


Figure 2.9: Experimental versus simulation curves obtained with the minimum cost value, for samples dissected through the media

*A – Arterial layer properties*

Figure 2.10 represents a histogram of values for 6 samples tested and Table 2.5 lists all the values corresponding to each sample. The values of  $C_{10\_ADV}$  were bound between 0.03 and 0.2, the values of  $C_{10\_MED}$  between 0.1 and 0.6 and the values of  $C_{10\_INT}$  between 0.3 and 1.3.

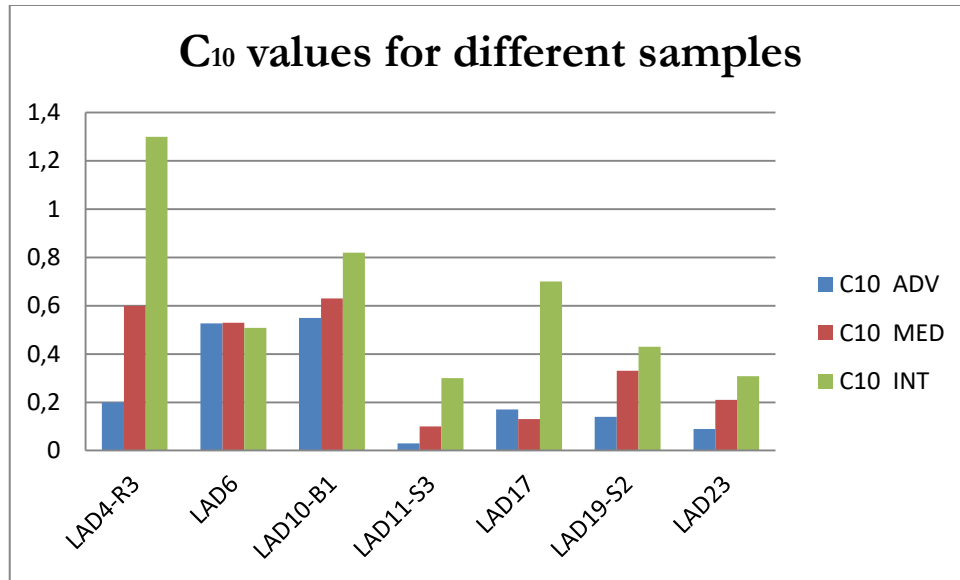


Figure 2.10: Characterization of C10 for the three layers of different samples (Histogram format)

Table 2.5 lists these results.

Table 2.5: C10 values for different samples (table format)

	<b>C<sub>10</sub> [MPa]</b>		
	<b>ADV</b>	<b>MED</b>	<b>INT</b>
<b>LAD4R3</b>	0.2	0.6	1.3
<b>LAD6</b>	0.52	0.53	0.51
<b>LAD10-B1</b>	0.55	0.63	0.82
<b>LAD11S3</b>	0.03	0.1	0.3
<b>LAD17</b>	0.17	0.13	0.7
<b>LAD19-S2</b>	0.15	0.33	0.43
<b>LAD23</b>	0.09	0.21	0.30

As shown in Table 2.5,  $C_{10}$  values identified were higher for the intimal layer than for media and adventitia. Figure 2.11 shows the average values and the standard deviation represented by the error bars, for the three layers.

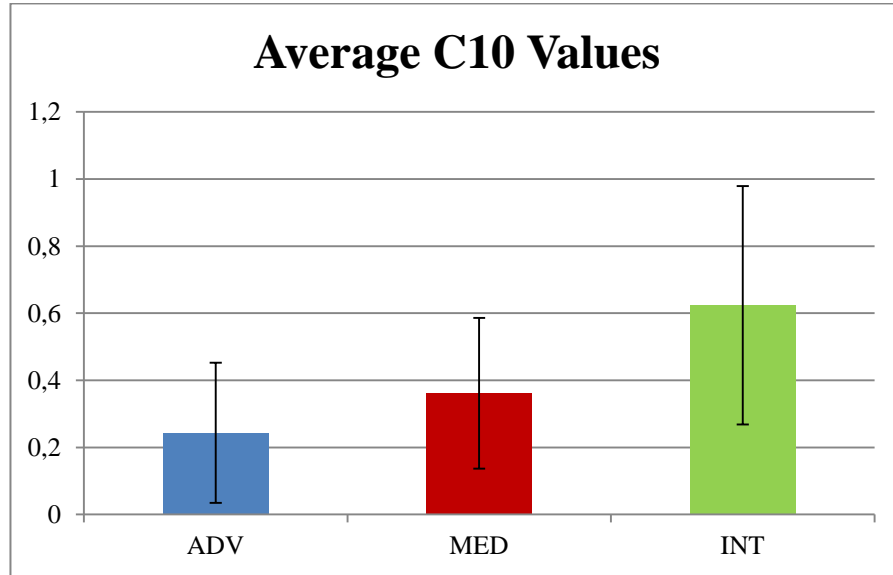


Figure 2.11: Average C10 values for the three layers

*B – Interface layer properties (cohesive parameters)*

Table 2.6 and Table 2.7 show the cohesive parameters corresponding to the curves represented in Figure 2.8 and Figure 2.9. Two groups were distinguished, one with dissection through the media and one with dissection through the intima.

1 – Dissection through Intima

Table 2.6: Cohesive parameters corresponding to the minimum error between numerical and experimental curves in dissection through intima cases

Sample	$K_{eff}$ (MPa/mm)	$T_0$	$\delta f$ (mm)
LAD4-R3	5	0.05	1
LAD6	17.5	0.07	0.4
LAD10-S1	14.25	0.0224	1.1
LAD11-S3	1	0.02	0.5

## 2 – Dissection through Media

Table 2.7: Cohesive parameters corresponding to the minimum error between numerical and experimental curves in dissection through media cases

<b>Sample</b>	<b>K<sub>eff</sub> (MPa/mm)</b>	<b>T<sub>0</sub></b>	<b>δf</b>
<b>LAD17</b>	5.75	0.02	0.4
<b>LAD19</b>	1.4	0.012	1.6
<b>LAD23</b>	19.2	0.096	0.5

The average values of the different cohesive parameters  $T_0$ ,  $K_m$  and  $\delta f$  were respectively 0.046 MPa, 9.43 MPa/mm and 0.75mm for the samples where the dissection occurred through the intima layer, and 0.042MPa, 8.7MPa/mm and 0.8mm for samples where dissection occurred through the media layer.

## Section 4 – Discussion

Few studies reported the neo-Hookean parameter values independently of the fiber contribution. In our study, the Neo-Hookean constitutive equation was sufficient to reproduce the elastic part of the response. This elastic part was restricted to small strains and did not involve much collagen fiber recruitment, justifying neglecting an exponential term in the constitutive equations. In order to check if our values correspond to literature values, the ratio  $R$  ( $C_{10}$  layer1/  $C_{10}$  layer2) was calculated. This ratio, even if it is calculated for non-coronary artery specimens, still gives an indicative idea. Table 2.8 shows  $C_{10}$  values reported in some studies along with the  $R$  ratio.

Table 2.8: R values reported from literature

Papers	Samples used	$C_{10}$ ADV [MPa]	$C_{10}$ MED [MPa]	$C_{10}$ INT [MPa]	$R = C_{10}MED/C_{10}ADV$
Holzapfel et al. 2000 <sup>102</sup>	Rabbit carotid Artery	0.003	0.03	-	10
Holzapfel et al. 2002 <sup>103</sup>	LAD	0.0027	0.27	-	10
Holzapfel et al. 2006 <sup>94</sup>	Human Aorta	0.08	0.165	0.2	2.02
Yosibash et al. 2012 <sup>97</sup>	Human coronary arteries	0.005	0.01	-	2

In order to check if the differences of the  $C_{10}$  values were significant between each layer, since the data does not satisfy a normal distribution, a Mann-Whitney test was applied to the Adventitia-Media data, Media-Intima data, and Adventitia-Intima data. The Mann-Whitney test is the non-parametric statistical test equivalent of the unpaired t-test using the rank order of data instead of the raw data. It is used when the data being

analyzed does not follow a normal distribution. The test showed that non-significant differences were observed for  $C_{10}$  values between Media and Intima but on the other hand, the differences between Adventitia and Media-Intima were significant.

Table 2.9 shows the obtained R values.

Table 2.9: R values calculated for the samples studied

	$C_{10}$ [MPa]			R= $C_{10}MED/C_{10}ADV$
	3 parameters			
	ADV	MED	INT	
<b>LAD4R3</b>	0.2	0.6	1.3	3.00
<b>LAD6</b>	0.52	0.53	0.51	1.02
<b>LAD10-B1</b>	0.55	0.63	0.82	1.15
<b>LAD11S3</b>	0.03	0.1	0.3	3.33
<b>LAD17</b>	0.17	0.13	0.7	0.76
<b>LAD19S2</b>	0.15	0.33	0.43	2.20
<b>LAD23</b>	0.09	0.21	0.30	2.33

R (Med-Adv) varies between 0.8 and 3.4, which is an indicator that the media is stiffer than the adventitia. Table 9 shows the ratio R calculated for different studies in the literature. For the studies listed, R varies between 2 and 10. This result is in agreement with our results.

Few studies have reported the  $C_{10}$  value for the intima of an artery. Arteries of laboratory animals have generally two mechanically significant layers (media and adventitia) <sup>104</sup>; however, in human aged arteries the intima is a third mechanically significant layer of considerable thickness and mechanical strength . The ratio R(int-med) in (Holzapfel G. A., 2006)<sup>8</sup> was 1.25, so the intimal layer is stiffer than the medial layer,

which is also the case in most of our results. It is important to note that pathological changes of the intimal components (*atherosclerosis*) are associated with significant alterations in the mechanical properties of arterial walls, differing significantly from those of healthy arteries <sup>105,106</sup>. The samples tested and reported in this study were taken from patients with ischemic cardiomyopathy which may also explain the thickening of the intimal layer.

The values obtained were considered for the next work to perform the dissection simulations using the cohesive elements.

The variation in material properties among specimens could relate to differences in arterial composition. For instance, smooth muscle cells are known to be molecularly heterogeneous and may cause this heterogeneity in mechanical properties <sup>107</sup>. This would explain the differences between the values for the different samples belonging to the different coronary arteries tested.

Different numerical studies have already been published related to dissection problems. They used different cohesive laws, so different parameters than the ones identified in this study.  $T_0$  was always a reported value. Figure 2.10 shows the different values obtained in these studies.

Table 2.10: Cohesive parameters used in different published numerical studies

<b>Study</b>	<b>Dissection part studied</b>	<b>G[N/mm]</b>	<b><math>T_0</math> [MPa]</b>
<b>Ferrara 2010<sup>84</sup></b>	Coronary arteries	0.049	[0.014-0.14]

<b>Ferrara 2007<sup>83</sup></b>	Aortic dissection	0.16	0.2 (medial) 0.7 & 0.2 (diseased intima)
<b>Gasser 2007<sup>77</sup></b>	Human iliac artery	-	0.16
<b>Badel 2014<sup>88</sup></b>	Coronary arteries	0.02	0.01

The average  $T_0$  value obtained by our identification for all samples was 0.046 MPa and it falls in the range of the values reported in Table 2.10.

A statistical study was done to gain a better understanding about the most influential factor among the three cohesive factors on the differences of G values obtained between dissection through media and dissection through intima. The results showed that the most influential factors were K and  $\delta_f$  parameters.

(Wang et al. 2014) studied the difference between tearing events occurring within the intima and tearing events occurring within the media. They showed that the difference in dissection properties between layers was statistically significant. They also postulated that when the dissection starts by a tear through the intima, which has a higher stiffness, it can have a more complicated path and possibly kink to the media.

In our study only one cycle for each sample was considered. A statistical test was done to check for significant differences between the parameter values identified for dissection through the media and for dissection through the intima. Applying the Mann-Whitney test on the two groups of cohesive parameters (dissection through media and dissection through intima), results showed non-significant differences between the 2 groups. But in our study, only the first cycle from each sample was considered. This

could explain the non-significant differences between the values. To prove this hypothesis, a Mann-Whitney test was applied on the two groups of G values obtained by (Wang et al. 2014) including the first cycle only. The test showed that the difference between tearing events occurring within the intima and within the media is statistically non-significant, which is not the case when all the cycles are considered. This indicates that the difference of properties between the intima and the media may have an impact on cohesive parameters only for larger cracks but not for the first cycle.

## Section 5 – **Conclusions & Future Work**

Arterial dissection occurring through arterial layers is a rare but sometimes fatal event that may occur in human coronary arteries. (Wang et al. 2014) explored dissection properties by evaluating the energy release rate needed to create these dissections. Using their force-displacement curves and energy release rates, we applied an inverse method to characterize the mechanical properties of the different layers composing the arterial wall (Adventitia, Media & Intima). For the dissection, a cohesive zone model was used. The cohesive parameters were also identified with the inverse method.

The results obtained showed that the media and the intima have similar mechanical properties. Significant differences were observed between the adventitia layer and the media-intima layers. Our study was the first to report mechanical properties for the intima for human coronary arteries.

Non-significant differences were observed for the three cohesive parameters for samples with dissection occurring through the media vs. samples with dissection occurring through the intima. This result could be explained by the fact that only the first cycles were considered in this study.

For future work, a global study should be realized including several cycles to check which parameter is the most influential factor on the differences between dissection through the media and dissection through the intima.

## **CHAPTER 3 ATHEROSCLEROTIC PLAQUE DELAMINATION: 2D FINITE ELEMENT MODEL TO SIMULATE PLAQUE PEELING IN APOE KNOCKOUT AND APOE COL8 DOUBLE KNOCKOUT MICE**

### ***Abstract***

*Finite element analyses using cohesive zone models (CZM) can be used to predict the fracture of atherosclerotic plaques but this requires setting appropriate values of the model parameters. In this study, material parameters of a CZM were identified for the first time on two groups of mice ( $ApoE^{-/-}$  and  $ApoE^{-/-} Col8^{-/-}$ ) using the measured force-displacement curves acquired during delamination tests. To this end, a 2D finite-element model of each plaque was solved using an explicit integration scheme. Each constituent of the plaque was modeled with a neo-Hookean strain energy density function and a CZM was used for the interface. The model parameters were calibrated by minimizing the quadratic deviation between the experimental force displacement curves and the model predictions. The elastic parameter of the plaque and the CZM interfacial parameter were successfully identified for a cohort of 11 mice. The results revealed that only the elastic parameter was significantly different between the two groups,  $ApoE^{-/-} Col8^{-/-}$  plaques being less stiff than  $ApoE^{-/-}$  plaques. Finally, this study demonstrated that a simple 2D finite element model with cohesive elements can reproduce fairly well the plaque peeling global response. Future work will focus on understanding the main biological determinants of regional and inter-individual variations of the material parameters used in the model.*

**Keywords:** *Cohesive zone model, plaque delamination, explicit scheme, inverse approach, parameter identification, collagen VIII*

## Section 1 – Introduction

Atherosclerotic plaque rupture is a major cause of myocardial infarction, coronary thrombosis and stroke. Cardiovascular diseases resulting from atherosclerosis are the leading cause of mortality in both developed and developing countries. Three-fourths of myocardial infarctions are caused by the rupture of atherosclerotic plaques, affecting about 1.1 million people in the US annually, with a fatality rate of 40%; 220,000 of these deaths occur without hospitalization<sup>59</sup>. Thus, a better understanding of this disease is needed to develop effective approaches for treatment and intervention. Experimentally, several studies have focused on developing experimental protocols to quantify the adhesive strength of the bond between two biological materials<sup>51,108–111</sup>. To better understand the plaque delamination process, Wang et al. 2011<sup>4</sup> developed and applied a methodology to quantify the adhesive strength between the atherosclerotic plaque and the underlying vascular wall. The method was applied to the apolipoprotein E knockout (apoE<sup>-/-</sup>) mouse model after 8 months on Western diet. The apoE-deficient mouse is an animal model frequently used in atherosclerosis research due to the development of plaques of similar type and distribution as in humans<sup>112,113</sup> and mice lacking apoE (ApoE<sup>-/-</sup>) provided the first practical animal model of hyperlipidemia and atherosclerosis<sup>114</sup>. The study by Wang et al. used the local energy release rate,  $G$ , as a quantifiable metric for direct comparison of plaque separation strengths.

On the computational side, cohesive zone models (CZM) have been applied to biological tissues to better understand a number of medical problems that involve separation of tissue layers. The cohesive zone is defined as the infinitesimally thin layer in which initialization and coalescence of micro-cracks are lumped into a discrete surface, based

on the elasto-plastic fracture theory of metals<sup>74, 75</sup>, and on the quasi-brittle fracture theory of concrete<sup>76</sup>. This approach is used to model the delamination or separation between layers. To understand some medical problems where fractures or separations between layers occur, the CZM has been used in modeling soft biological tissues<sup>83-87</sup> and bones<sup>115-118</sup>. These studies used CZM with traction-separation cohesive laws. None of these studies used experimental data obtained from direct mechanical experiments to identify both cohesive and material parameters at the same time. In the study presented here, a 2D numerical finite element model was developed to identify material parameters and cohesive parameters based on experimental data. The method we present could be applied to any medical problem where separation between layers occurs, such as arterial dissection or atherosclerotic plaque delamination. For soft biological tissues, Ferrara et al. 2010 used CZM to study the dissection properties of individual arterial tissues<sup>83</sup>. Gasser et al. 2006 used the CZM technique to model the propagation of arterial dissections using an explicit scheme<sup>85</sup>. In their study, they defined the dissection as a gradual process in which cohesive traction resists separation between two material surfaces. The presence of collagen in arterial layers motivated the use of this cohesive concept. A recent numerical study by Leng et al. 2015 also used CZM finite element analyses with an implicit resolution scheme to simulate atherosclerotic plaque delamination in ApoE knockout mouse abdominal aorta specimens, placing the cohesive zone along the plaque-media interface where delamination occurs<sup>5</sup>. The simulation predictions of force-displacement curves for the simulated cycles were found to match reasonably well with the experimental data, especially for the plaque deformation phase, but differences were still observed during the separation phase and the unloading phase. Leng et al explained these

differences by the fact that many parameters used in the model were not directly calculated but taken from existing values in the literature. They also considered that the use of the Holzapfel-Gasser-Ogden model (HGO) for the plaque could be the reason for these differences.

In summary, an experimental protocol was developed by Wang et al. to study atherosclerotic plaque delamination as a fracture mechanics problem by quantifying the energy release rates, but few studies have used CZM to study this problem. Those that did generally did not consider an explicit resolution approach, and many parameter values were assumed due to a lack of geometrical data.

In the current study, we focused on developing a 2D finite element modeling and simulation approach, using an inverse method, to identify material and cohesive parameters based on experimental delamination tests between atherosclerotic plaque and the underlying vascular wall in Type VIII collagen-deficient and non-deficient (control) apoE knockout (ApoE<sup>-/-</sup>) mice. In this particular problem, an explicit dynamic method of resolution was used (Abaqus 6.13-1 Explicit). Collagen Type VIII, from the short-chain non-fibrillar collagen family, is present in small amounts in normal arteries. After injury and during development of atherosclerosis in experimental animals and humans, the synthesis of type VIII collagen is dramatically increased<sup>119, 120</sup>. Thus, comparison of experimental plaque delamination data from mice belonging to a control group (ApoE<sup>-/-</sup>) and from a collagen VIII deficient group (ApoE<sup>-/-</sup> Col8<sup>-/-</sup>) presented an interesting test case to develop the FE model.

## Section 2 – **Materials and methods**

### I – **Experimental protocol**

Four C57Bl6 congenic ApoE<sup>-/-</sup> mice and seven ApoE<sup>-/-</sup> Col8<sup>-/-</sup> mice were fed with a high-fat (40% of total calories) diet during six months to develop advanced aortic atherosclerotic plaques. Mice were euthanized by carbon dioxide asphyxiation and perfused with heparinized saline at physiological pressure for five minutes. Mouse carcasses were firmly attached to a plate using adhesive tape. The aorta was opened longitudinally to visualize the atherosclerotic plaques. The adhesion strength between the atherosclerotic plaque and the internal elastic lamina (IEL) was measured with cyclic peeling experiments, based on a previously published protocol<sup>3,4</sup>. A Bose Electroforce 3200 Test Instrument was used to measure the force required for plaque delamination, and a stereomicroscope equipped with a CCD camera was used to capture images of the process. The Bose Test Instrument had two grips. One grip clamped the plate which held the mouse carcass with exposed aorta, and the other grip was attached to microclamps that held the tip of the plaque, after creating an initial notch to initiate delamination of the plaque.

Figure 3.1(a) shows a schematic of the experimental test setup. The Bose Electroforce 3200 Test Instrument applied controlled displacements to produce incremental delamination of the plaque, and the CCD camera acquired images of the newly exposed area underneath the plaque. Consecutive cycles were run with increasing total displacement until the plaque completely separated from the vessel wall. Figure 3.1(b) shows a schematic of the delamination process in an enlarged side view.

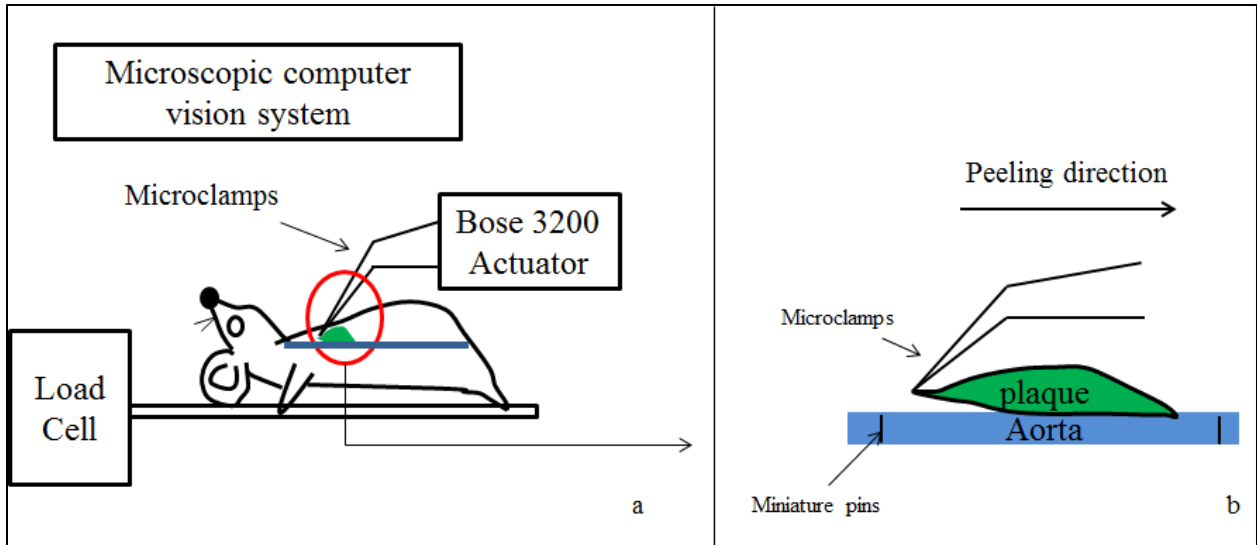


Figure 3.1: Schematic of the experimental setup; (a): the Bose machine prescribes a displacement (actuator) and records the resulting force (load cell). The micro-clamps are attached to the actuator and grip the tip of the plaque (b) Schematic of delamination process

Table 3.1 shows the total number of mice tested from each group (ApoE<sup>-/-</sup> and ApoE<sup>-/-</sup> Col8<sup>-/-</sup>), with the number of plaques tested (P<sub>i</sub>; where “i” is the index referring to the number of the plaque tested from the same mouse) and the total number of loading cycles obtained from each plaque.

Table 3.1: Number of plaques and cycles obtained from each mouse group

	Mouse ID	Plaque ID	Total Cycles
ApoE <sup>-/-</sup>	124	P1	7
	145	P1	2
	158	P1	2
	161	P1	2
		P2	4
<b>Total</b>	<b>4</b>	<b>5</b>	<b>17</b>
	150	P1	1

<b>ApoE<sup>-/-</sup> Col8<sup>-/-</sup></b>	151	P1	1
	152	P1	3
	157	P1	2
	173	P1	2
	174	P1	1
		P2	5
		P3	4
175	P1	3	
<b>Total</b>	<b>7</b>	<b>9</b>	<b>22</b>

## II – Delamination Test and Data Acquisition Experimental Protocol

### *A – Determination of the fracture energy from each delamination cycle $\Delta E$*

Figure 3.2 shows an example of a force-displacement curve obtained during delamination. The curve is composed of three parts. The first part shows the initial ramp of the load versus displacement curve. This section is not part of the separation phase but represents the energy associated with deformation of the plaque before the event of separation. The first slope discontinuity of the curve represents the beginning of the delamination process that occurs when the measured load reaches a first maximum and drops. The second part of the curve is jagged or serrated; this region corresponds to the delamination process. The third part represents the unloading phase. The area of the region surrounded by the curve, represented in Figure 3.2, is the energy dissipated throughout one delamination cycle and it is denoted  $\Delta E$ .

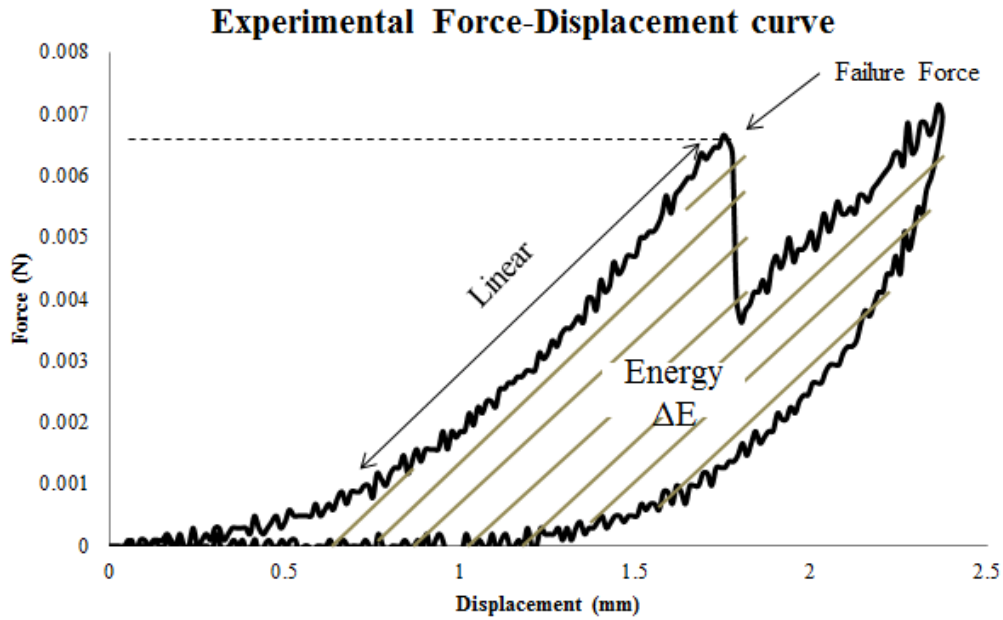


Figure 3.2: A representative image of the raw force vs. displacement data. The area under the load-displacement curve represents the energy released during one delamination cycle. The linear region depicted is used to determine the plaque stiffness for each cycle

### *B – Determination of exposed area $\Delta A$*

The area exposed at the plaque-IEL interface during one delamination cycle,  $\Delta A$ , is measured using ImageJ<sup>27</sup> by determining the area before delamination,  $A_i$ , and the area after delamination,  $A_f$ . To make this measurement, we applied diluted black marking tissue dye onto the surface of the plaque and onto its surrounding area before sequential delamination cycles. Pictures were taken before and after each cycle. At the end of the cycle the newly exposed area was white (or lighter than the surrounding area). The difference in colors was used to segment the newly exposed region and to measure its area  $\Delta A$  as defined in Eq. (3.1).

$$\Delta A = A_f - A_i \quad (3.1)$$

Three independent reviewers measured  $\Delta A$  for each cycle of delamination. Area measurements that agreed within 10% between reviewers were averaged to determine the final value of  $\Delta A$  for each cycle. Figure 3.3 shows a sample where the white area (newly exposed region) has been delimited by a yellow line.

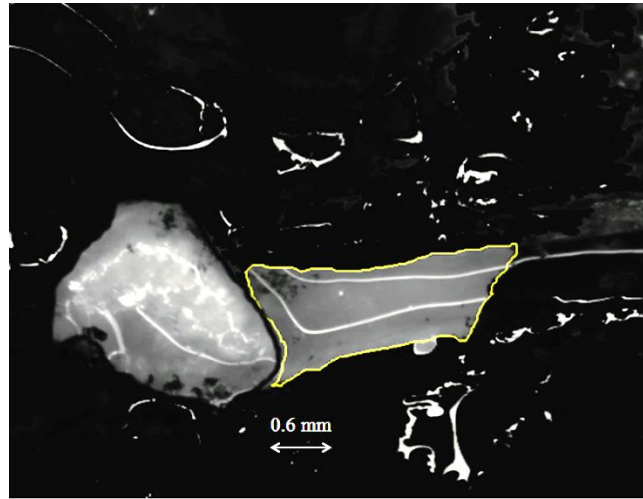


Figure 3.3: The estimated  $\Delta A$  for one cycle, outlined by yellow (top view)

#### *C – Calculation of $G$ (energy release rate)*

The energy release rate,  $G$  (N/mm), is a measure of adhesion strength and is calculated by dividing the energy released during delamination,  $\Delta E$ , by the area exposed during the same delamination,  $\Delta A$  as shown in Eq. (3.2):

$$G = \Delta E / \Delta A \tag{3.2}$$

#### *D – Statistical analysis*

A Shapiro-Wilk test was used to test the normality of the distributions of  $G$  values. For normally distributed data, a t-test was performed to test for differences between the two genotypes and for non-normally distributed data, a Mann-Whitney nonparametric test

was used to compare the median values between the ApoE<sup>-/-</sup> mice and the ApoE<sup>-/-</sup> Col8<sup>-/-</sup> mice.

### III – Finite-Element model

#### *A – Abaqus Explicit*

The explicit solver of the ABAQUS<sup>®</sup> software<sup>121</sup> was used in our simulations. An explicit solver in finite-element analyses uses an explicit time integration scheme to solve dynamic problems or quasi-static nonlinear problems. The explicit solver is particularly suitable for highly nonlinear problems as is the case here with contact and fracture issues<sup>122,123</sup>.

#### *B – Geometry*

Figure 3.4(a) shows a representation of the geometrical parameters used to create the 2D finite element model for our simulations. Some of these values could be measured by reference to images and experimental data, and others could not be measured. This was especially true of geometric parameters related to the aorta (media), such as the total length, the total width and the thickness. Therefore, we referred to values measured in other studies of similar problems and we assumed that these values could be applied in our simulations. The medial width ( $W_m$ ) was reported for ApoE<sup>-/-</sup> mice in the study of Gregersen et al.2007<sup>124</sup> to be in the range of 2 mm. Medial height (or thickness,  $H_m$ ) was also determined by the same authors to be in the range of 0.08 to 0.16 mm. In our simulations,  $H_m$  was set equal to 0.15 mm. The total length of the aorta (media) could not be identified using the experimental pictures, so we assumed that  $L_m$  was three times greater than the plaque length. A plate was added under the aorta with a frictionless

contact to avoid displacement in the negative y-direction, as in the experiments. The total length of the plate was set equal to the length of the aorta.

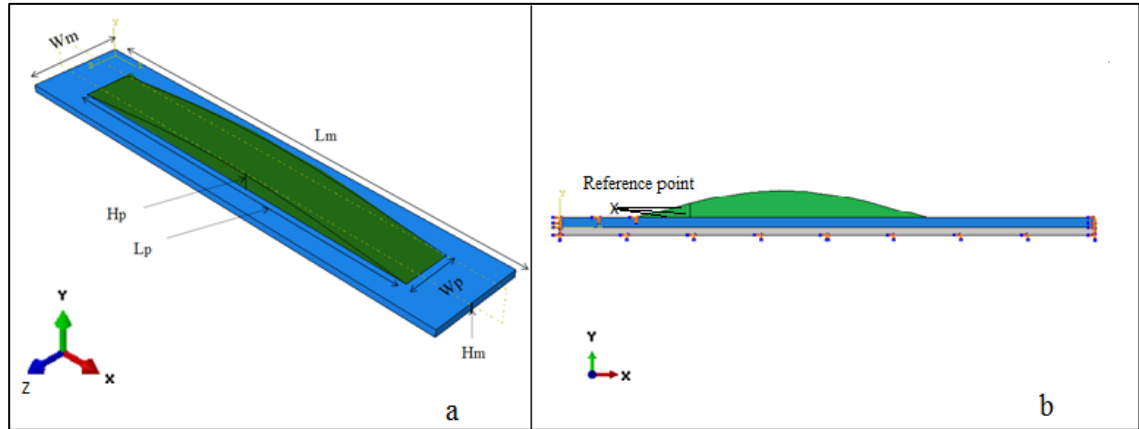


Figure 3.4 : Schematic representation of the plaque model and the underlying aorta. (a):  $L_m$  represents the aortic media length,  $L_p$  the plaque length,  $W_m$  the medial width,  $W_p$  the plaque width,  $H_m$  the medial height and  $H_p$  the maximum plaque height ( $L_m$  not shown to scale); (b): 2D representation of the atherosclerotic plaque (green) attached by cohesive elements to the underlying aorta (blue), lying on the gray rigid surface (S). The bottom edge of S, the left & right edges of (A+S), and the top left edge of A were clamped to simulate experimental testing conditions. The reference point represents the master node where displacement boundary conditions were applied.

#### 1 – Plaque length ( $L_p$ ) measurement

The plaque length was estimated using histological images. After total detachment of the plaque from the aorta, the plaque was kept for histology studies. The plaque was embedded vertically and cross sections of 5  $\mu\text{m}$  were made. Five sections were collected, then five sections were skipped, and this action was repeated until the entire plaque had been sectioned. The five collected sections represent a group. Each histological image was representative of these five sections forming a group. Thus, each image represented a plaque length of 25  $\mu\text{m}$ . Adjacent groups were separated by another 25  $\mu\text{m}$  of sectioned length. Therefore, if there were ten histological images for a particular plaque the estimated length would be 500  $\mu\text{m}$ .  $L_p$  values for each plaque are

shown in Table 3.2 Note here that this calculated length was underestimated since some tissue shrinkage occurs upon fixation and embedding.

### 2 – Plaque height (Hp) measurement

The plaque height was also calculated using histological images. Assuming that the middle of the plaque has the largest height, the height of the middle section was measured and considered to be the maximum height of the plaque. Values are reported in Table 3.2.  $H_p$  and  $L_p$  were underestimated using this approach, since there was some tissue shrinkage during fixation and embedding.

### 3 – Plaque width (Wp) measurement

Assuming that the plaque width is the same along the length of the plaque, the plaque width was measured using the CCD camera images recorded during experiments. The values are reported in Table 3.2.

Table 3.2: Plaque Geometry: ( $L_p$ ) Plaque Length, ( $W_p$ ) Plaque Width and ( $H_p$ ) Plaque Height

	Mouse	Plaque	$L_p$ (mm)	$W_p$ (mm)	$H_p$ (mm)
<b>ApoE<sup>-/-</sup></b>	124	P1	4.65	0.4	0.5
	145	P1	1.8	0.45	0.18
	158	P1	3.5	0.6	0.32
	161	P1	3.2	0.75	0.14
		P2	3.2	0.9	0.30
<b>ApoE<sup>-/-</sup> Col8<sup>-/-</sup></b>	150	P1	2.8	0.94	0.17
	151	P1	4	0.8	0.28
	152	P1	2.8	0.9	0.3
	157	P1	3.8	0.4	0.39
	173	P1	3.6	0.7	0.13

	174	P1	2.5	0.74	0.18
		P2	4	0.47	0.11
		P3	2.6	0.75	0.14
	175	P1	2.8	0.5	0.12

### *C –Boundary Conditions*

Experimentally, the lower face of the aorta was free, since the vessel was secured across its width only with micro-pins placed a few millimeters above and below the plaque. These micro-pins are represented in the 2D model as fixed contact points between the aorta and the underlying plate at the left and right edges of the media. The underlying plate was added in contact with the aorta to avoid any displacement in the (-y) direction. Figure 3.4(b) shows a model with a thick plaque (0.4 mm), the aorta, and the cohesive layer as an extension of the notch of 1 mm created between the plaque and the underlying aorta.

Figure 3.5 shows four pictures at four different times of the simulation. It shows how the boundary conditions were assigned. The simulations were run in 2 steps. In the first step, a vertical displacement of 1 mm was applied on the master node to move the tip of the plaque to a vertical position, allowing at the same time free horizontal displacement and free rotation. Once the vertical displacement of 1 mm was reached, a horizontal displacement was applied in the dissection direction. For each sample, the horizontal displacement was set equal to the value applied in the respective experiment. This step simulated the plaque delamination stage where the data (force-displacement curves) were collected.

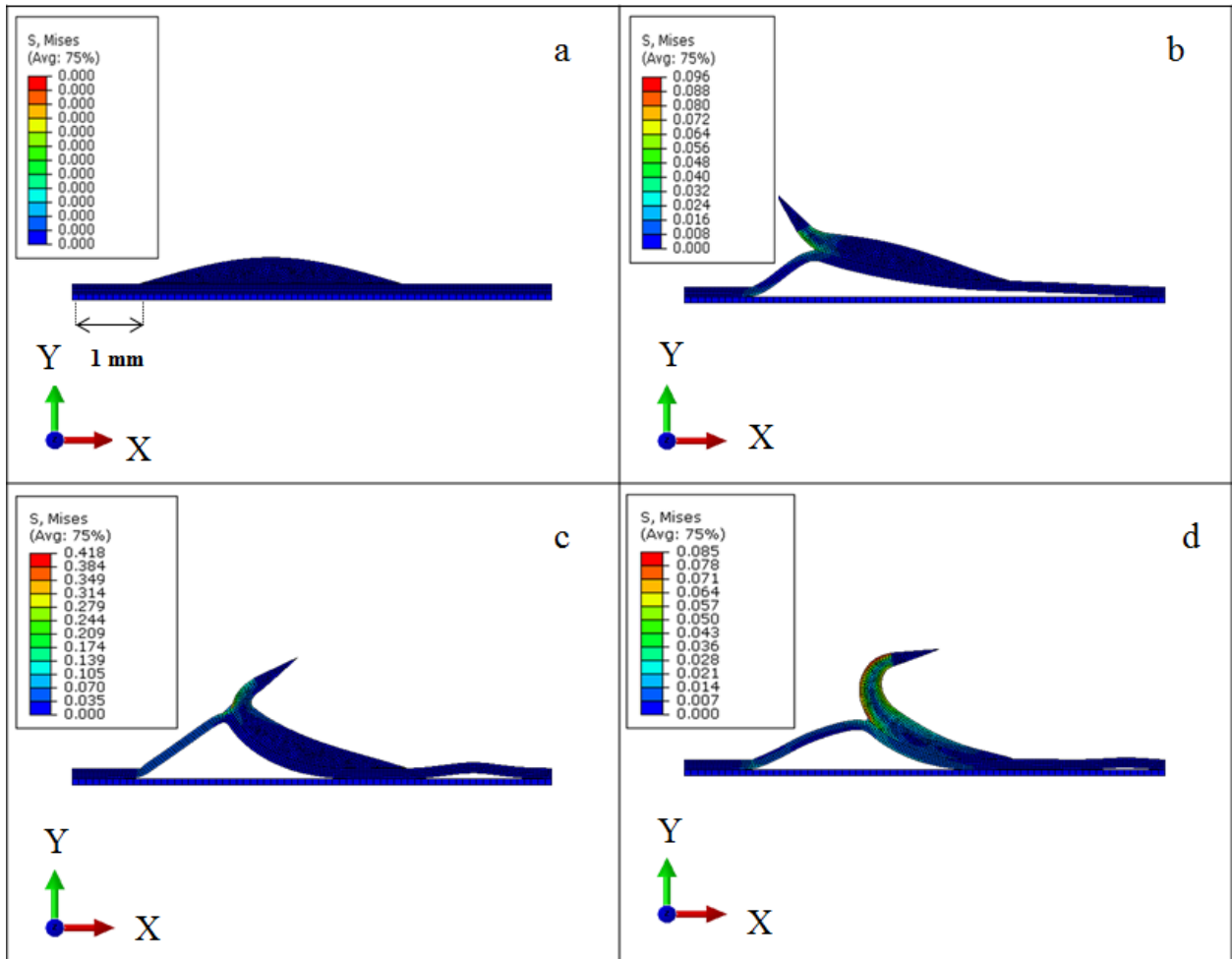


Figure 3.5: Simulation of the peeling test at 4 different times throughout the test

### Mesh size

The geometry was meshed using plane strain quadrilateral elements. The cohesive zone was meshed using only quadrilateral structured elements of cohesive type.

After trying different mesh sizes for the plaque and media (0.01, 0.025, 0.05 mm), it was found that a mesh size set equal to 0.025 mm gives acceptable results within a reasonable computational time (less than 2.8% error when compared with the 0.01mm mesh). The mesh size for the plate underneath the plaque was larger since this zone was kept rigid in this problem.

## *D –Material Model*

### 1 – Necrotic core

The necrotic core, which is not as clearly defined in mouse plaques as in human plaques, was treated as having the same material properties as the fibrous cap.

### 2 – Fibrous cap and underlying aorta

The fibrous cap and the underlying layer were modelled using a Neo-Hookean model. The strain energy function for a Neo-Hookean model is represented by Eq. (3.3):

$$\Psi = C_{10}(\bar{I}_1 - 3) + \frac{1}{D_1} (J_{el} - 1)^2 \quad (3.3)$$

Where  $C_{10}$  is the shear modulus,  $\bar{I}_1$  is the first deviatoric strain invariant,  $D_1$  is the compressibility parameter, and  $J_{el}$  is the elastic volume ratio. Then, the first term of the equation represents the isotropic isochoric behavior and the second term represents the compressibility behavior.

A Neo-Hookean model was used in several studies<sup>96, 97</sup> to represent the response of arterial tissues in the absence of collagen fiber recruitment. This model is widely used and accepted for small strains<sup>98, 99</sup>. In addition, in this CZM problem, the elastic properties of the wall at larger strains are of secondary importance compared to the cohesive properties<sup>100</sup>.

The underlying plate was modeled as a linear elastic material (Young modulus: 1200 MPa, Poisson ratio: 0.44).

### 3 – Interface between the plaque and the aorta

To represent the separation between the plaque and the underlying aorta, a bilinear traction separation cohesive law was used. Figure 3.6 depicts this law. It shows linear elastic loading (OA), followed by linear softening (AB). The normal maximum contact traction is reached at point A and denoted as  $T_0$ . Separation starts at point A and ends at point B when the normal contact traction reaches zero. The area under the OAB curve is the energy released due to complete separation, which is termed the critical fracture energy per unit area. It is assumed that separation is cumulative and that any unloading/reloading cycle induces a purely elastic response along line OC.

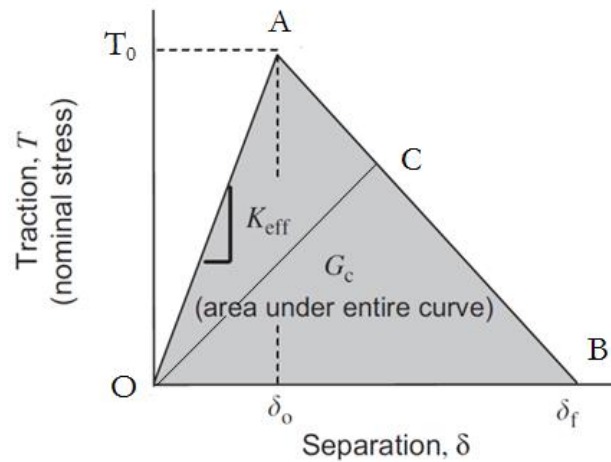


Figure 3.6: Traction/separation curve for Bilinear Cohesive Zone model

The parameters of the bilinear traction separation cohesive law to be characterized are:  $K_{\text{eff}}$  (MPa/mm),  $T_0$  (N/mm) and  $\delta_f$  (mm) (since  $\delta_f$  and  $T_0$  are related – see Eq. (3.4) - only one of them will have to be identified).

#### IV – Parameter identification using an inverse method

Teng et al.<sup>125</sup> showed that, for ApoE<sup>-/-</sup> mice,  $C_{10}$  is 1.4 times larger in the fibrous cap (FC) than in the media and  $C_{10}$  is 1.6 times larger in the intraplaque

haemorrhage/thrombus (IPH/T) than in the media. In the current study,  $C_{10}$  in the fibrous cap was set to twice the value of  $C_{10}$  in the media. This assumption is generalized in the rest of the simulations. Moreover, to avoid irrelevant solutions, bounds were defined for some of the unknown parameters.

$C_{10}$ : values between 0.01 and 0.5 MPa

$T_0$ : values between 0.05 and 0.2 MPa, which is consistent with values reported in the literature<sup>85</sup>.

Note that  $\delta_f$  and  $T_0$  are related to  $G$  by Eq. (3.4):

$$G = \left(\frac{1}{2}\right) \times T_0 \times \delta_f \quad (3.4)$$

The values of  $G$  were calculated directly from the force displacement curves for each cycle.

$K_{nn}$ , the initial stiffness of the cohesive elements, does not represent a physically measurable quantity and is treated as a penalty parameter. The value of this penalty stiffness must be high enough to prevent interpenetration of the crack faces and to prevent the introduction of artificial compliance into the model by the cohesive elements<sup>126</sup>. However, an overly high value can lead to numerical problems. Therefore, the value considered in the simulations for  $K_{nn}$  was 30MPa/mm.

In summary, two parameters of the model had to be identified from the experiments: the  $C_{10}$  elastic parameter of the plaque, and the  $T_0$  cohesive parameter. The inverse

method consisted in finding the values of these two parameters that minimize the deviation between the experimental and the numerical force-displacement curves. An initial matrix containing all combinations of parameter values,  $X_{initial} = [C_{10}, T_0]$  is defined, and a cost vector was defined such that:

$$cost_{vector}(j) = F_{sim}(j) - F_{exp}(j) \quad (3.5)$$

Where  $F_{sim}(j)$  is the force value predicted by the finite element model,  $F_{exp}(j)$  is the interpolated experimental force at the same displacement value, and  $j$  defines the index of the simulated point. Then the cost function value was calculated as in Eq. (3.6):

$$cost = \frac{[cost_{vector}(j) \times cost_{vector}^T(j)]}{\overline{F_{exp}}^2} \quad (3.6)$$

Where  $\overline{F_{exp}}^2$  represents the square of the average of the interpolated experimental force.

Finally, the minimum cost value was derived. Figure 3.7 shows an example of the pattern of the cost function for sample 173P1 with respect to the variations of  $C_{10}$  and  $T_0$ . It appears that the cost function has a unique minimum for  $T_0=0.09$ .

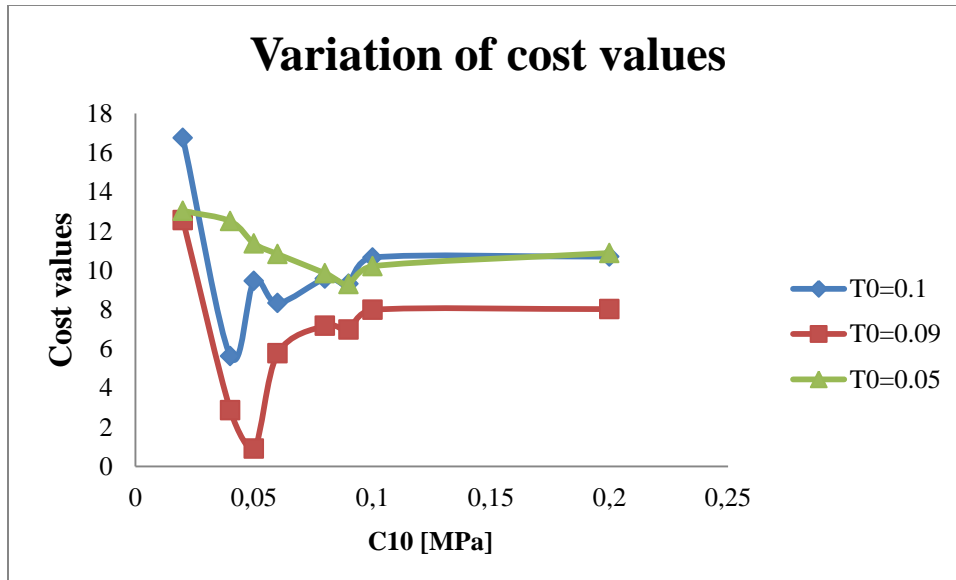


Figure 3.7: Variation of cost function values with respect to  $C_{10}$ , with  $T_0=0.05-0.10$  MPa for the sample 173P1 ApoE<sup>-/-</sup> Col8<sup>-/-</sup>

### V –Energy Balance

At the end of each simulation, an energy balance study was performed to verify that the solutions obtained satisfy quasi-static mechanical equilibrium. The kinetic energy must be negligible compared to the strain energy to satisfy this criterion.

## Section 3 – Results

### I – Experimental results

Results showed that the majority of G values were in the range [0.005-0.02] N/mm for both groups. The minimum value for both groups was 0.003 N/mm and belonged to the ApoE<sup>-/-</sup> Col8<sup>-/-</sup> group, and the highest value was 0.095 N/mm and belonged to the same group. To compare the differences in parameters between both groups, a statistical analysis was applied. Table 3.3 summarizes the averages and the standard deviations obtained for the energy release rate (G), the slope of the linear part of

the force-displacement curves, and the failure loads for each cycle. Average G values for both groups seemed to be similar with relatively large standard deviations for both groups (0.015N/mm for ApoE<sup>-/-</sup> group and vs 0.016 N/mm for ApoE<sup>-/-</sup> Col8<sup>-/-</sup> group). G values for both genotypes were not normally distributed; therefore, a Mann-Whitney test was applied and showed that the values were not significantly different between groups.

Table 3.3: Statistical parameters for energy release rate, stiffness, and failure load values for ApoE<sup>-/-</sup> and ApoE<sup>-/-</sup> Col8<sup>-/-</sup> mice

	G [N/mm]	
	ApoE <sup>-/-</sup>	ApoE <sup>-/-</sup> Col8 <sup>-/-</sup>
Average values	0.015	0.016
Median	0.01	0.01
Standard deviation	0.011	0.018
First quartile	0.008	0.0075
Third quartile	0.018	0.015

## II – Numerical results

After applying boundary conditions on the numerical model, the force-displacement curves obtained had the same shape as the experimental ones. Figure 3.8 shows a typical force- displacement curve obtained after simulation and after identifying the material parameters for one of the samples (173-P1). It shows that the curve was composed of three different segments as in experimental load-displacement curves (Figure 3.2). By comparing the changes in specimen geometry obtained after simulation (Figure 3.5) and the numerical curves, we could identify the mechanical process related to each part of the curve, as shown schematically in Figure 3.8.

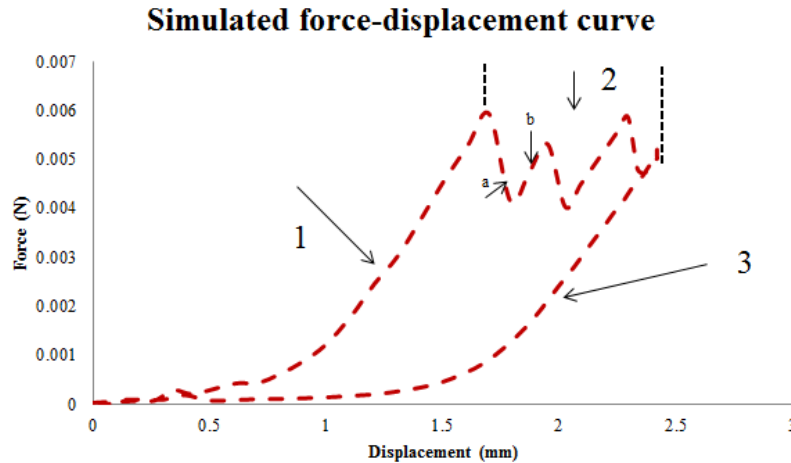


Figure 3.8: Force-displacement curve obtained after simulation for 1 sample. The curve consists of three segments: 1 represents the deformation of the attached peel arm of the plaque, 2 represents the separation phase where the cohesive elements are deleted to simulate the separation, and 3 represents the unloading phase. Segment 2 displays serrations related to the deletion of cohesive elements

The first segment (part 1) represents the deformation of the attached peeling arm of the plaque when the horizontal boundary condition was applied and before any separation occurred. The second segment (part 2) represents the separation between the plaque and the media layer. There were drops (a) and then increases (b) in force creating serrations as shown in Figure 3.8. Each drop in force represents a complete deletion of some cohesive elements because they had reached the maximum separation value. Then the force increased, which indicates that more cohesive elements were in the process of complete separation until they reached the maximum separation value and again created the release in force represented by the drops in Figure 3.8. The process of separation continued until the total horizontal displacement value was reached. The third segment (part 3) represents the unloading phase where an opposite horizontal displacement was applied on the attached arm of the plaque to take it back to the initial position. Figure 3.9

shows the results of the best-fit simulations with experimental curves for the first cycles from 4 different plaques from the ApoE<sup>-/-</sup> mouse group. It also shows the energy values during the simulations of the peeling test. In all cases the kinetic energy is negligible compared to the strain energy, which indicates that the solutions obtained satisfy quasi-static mechanical equilibrium.

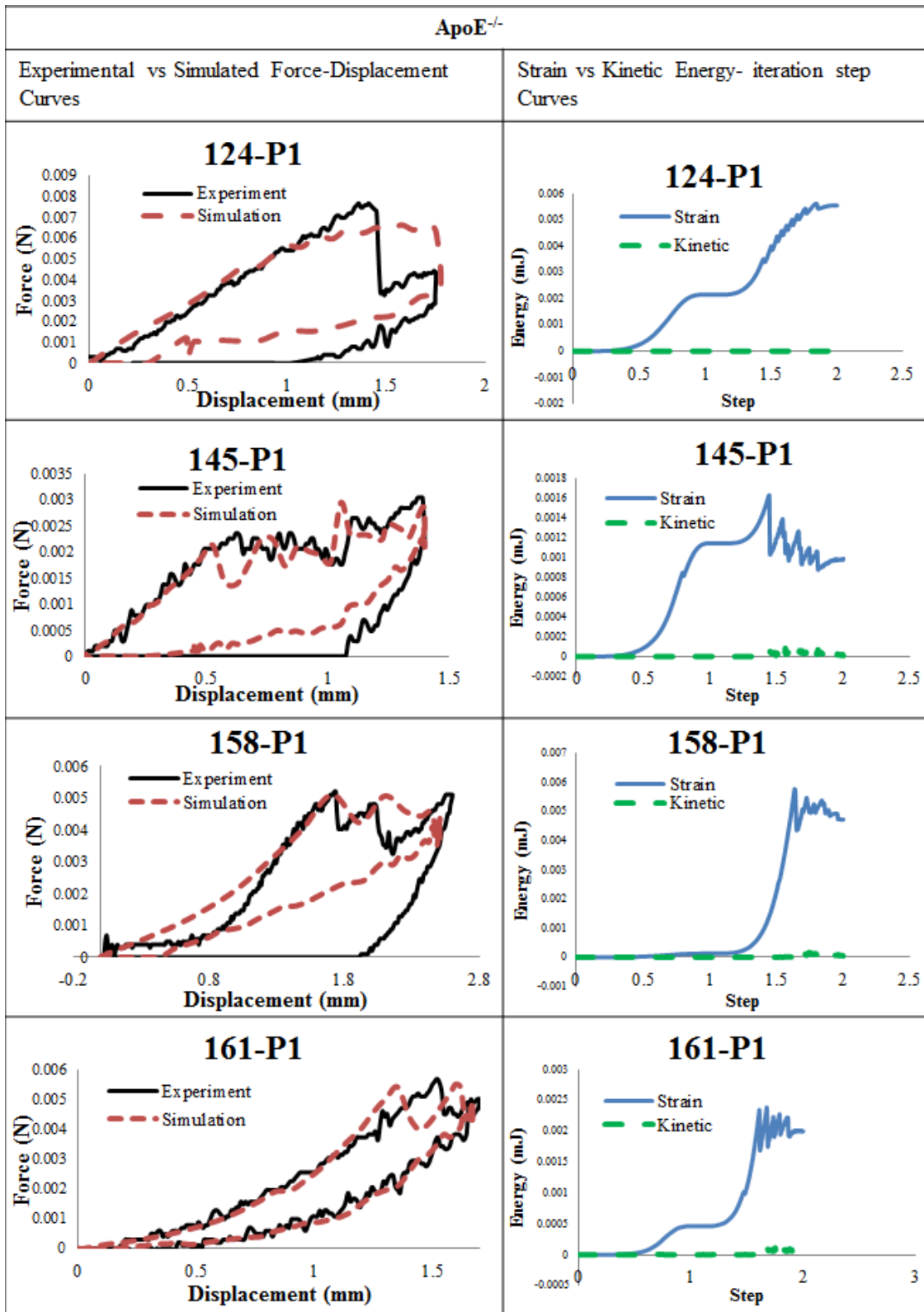


Figure 3.9: Experimental vs simulated force-displacement curves and strain vs kinetic energy for the first delamination cycles from four ApoE<sup>-/-</sup> mice

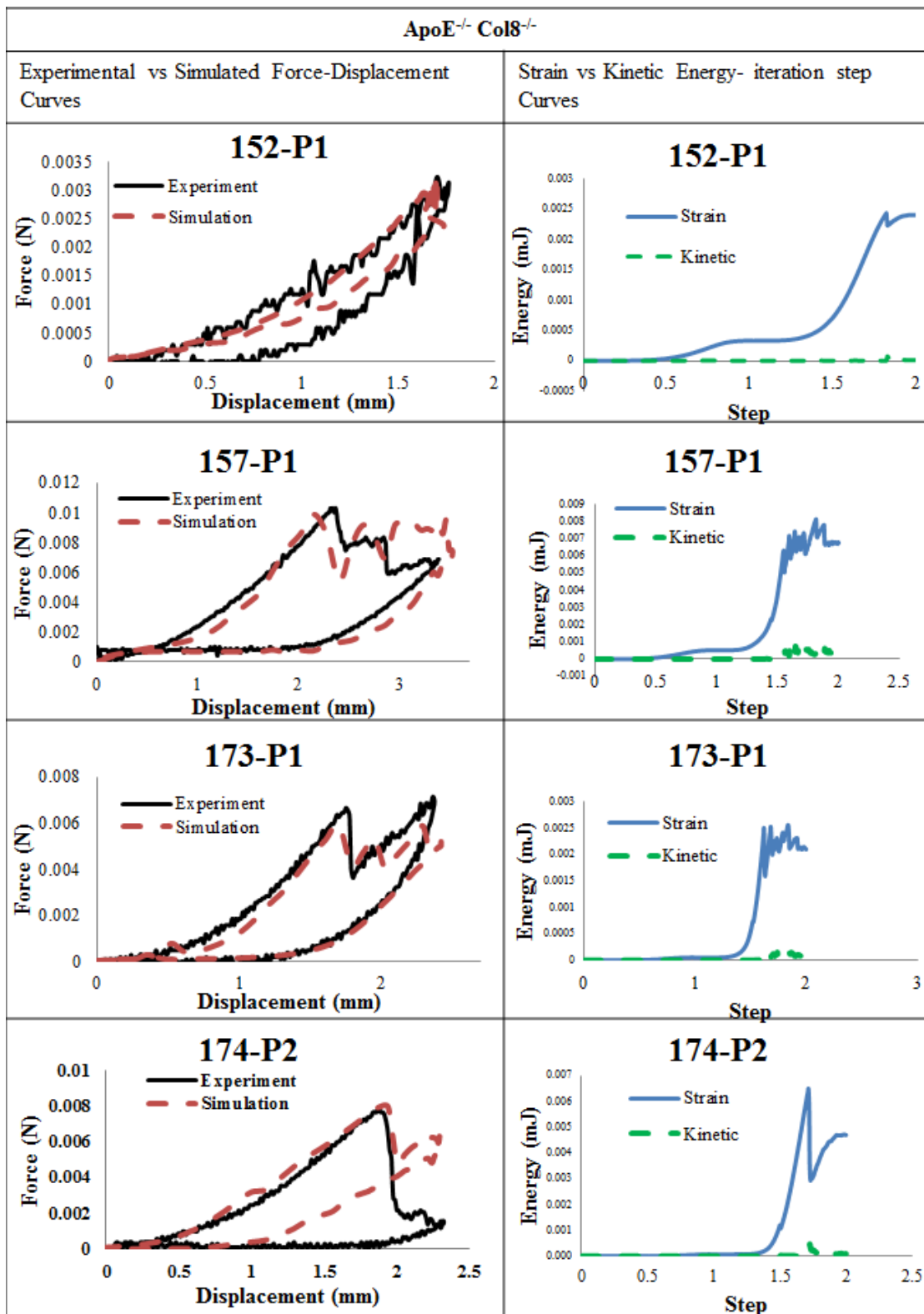


Figure 3.10: Experimental vs simulated force-displacement curves and strain vs kinetic energy for the first delamination cycles from four ApoE<sup>-/-</sup> Col8<sup>-/-</sup> mice

Figure 3.10 shows the best-fit parameters for the first cycles from 4 different plaques from the ApoE<sup>-/-</sup> Col8<sup>-/-</sup> mouse group. It also shows the energy values during the peeling test calculated from the simulation, verifying that the kinetic energy is negligible compared to the strain energy.

The  $T_0$  (cohesive parameter) and  $C_{10}$  (material parameter) best fit values are reported in Figure 3.11. Figure 3.11 shows the average values of  $G$ ,  $T_0$  and  $C_{10}$  obtained for ApoE<sup>-/-</sup> samples and ApoE<sup>-/-</sup> Col8<sup>-/-</sup> samples. Average values of  $G$  for the first group were higher than for the second.  $T_0$  values show a slight variation between the two groups.  $C_{10}$  average values between groups show an important difference, with the higher value for the ApoE<sup>-/-</sup> group.

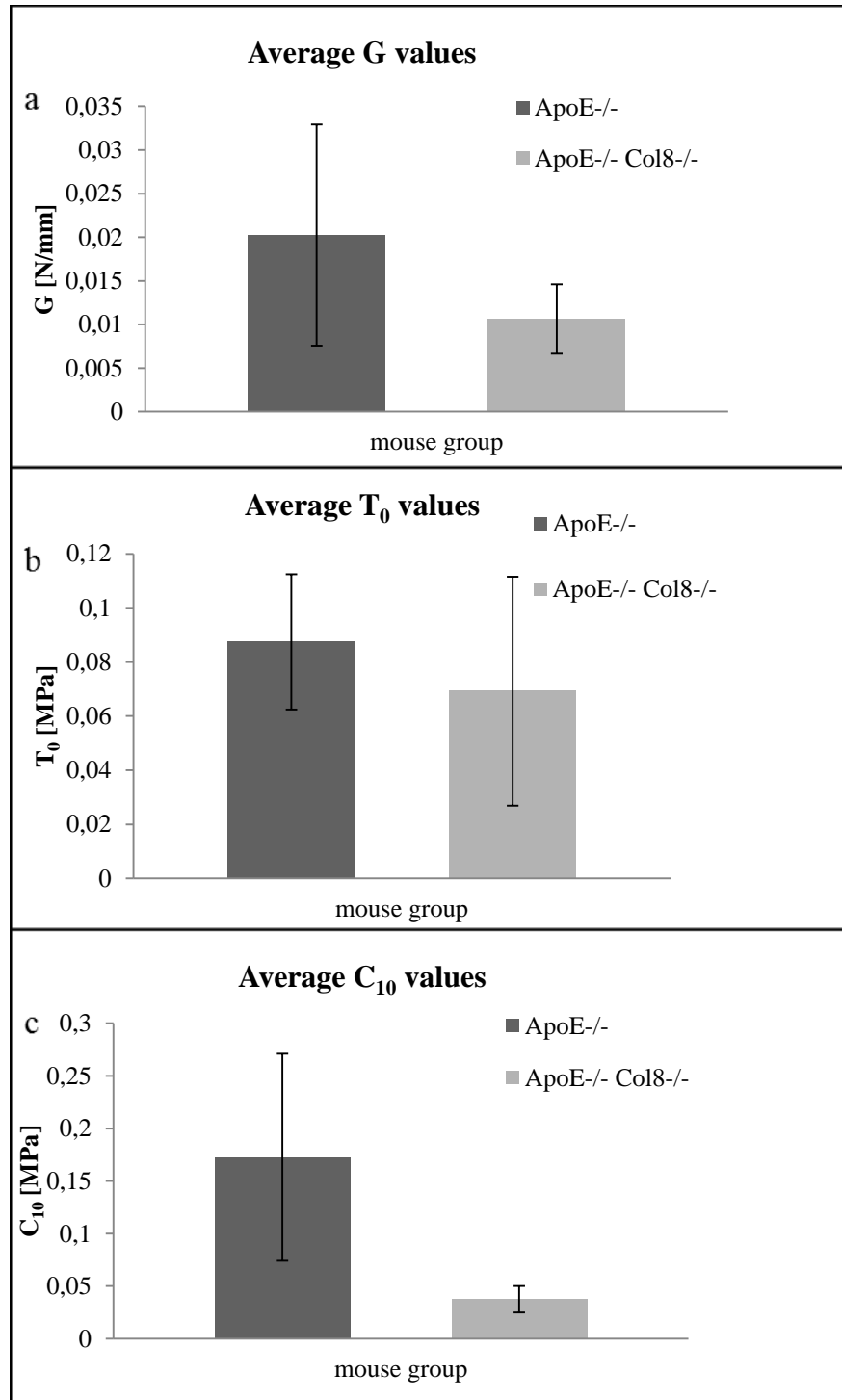


Figure 3.11: Histograms of average identified values and standard deviations for (a) G, (b) T<sub>0</sub>, and (c) C<sub>10</sub>

A statistical test is needed to check for significant differences in the three mechanical parameters between the two mouse groups. However, due to limitations in the number of

tested samples, this statistical test could not be applied. Therefore, we investigated the sample size needed to identify significant differences between groups for a T-test with  $\alpha=0.05$ . Alpha is defined as the Type I error probability for a two-sided test (the probability of false rejection of the null hypothesis). We found that 28 samples would have to be tested from each group with this amount of variation to determine whether there is a significant difference in G values between the two groups, while only 10 samples from each group would be needed to determine whether the differences were significant for  $C_{10}$  values between both groups. The test was not applied for  $T_0$  since the average values were similar. Fewer samples would be required to find significant differences between groups for  $C_{10}$  than for G (or  $T_0$ ).

## Section 4 – Discussion

### I – Discussion of experimental results

Table 3.3 shows the average and standard deviation for G values obtained in both mouse genotypes used in our experiments. We can see that the average value of G for ApoE<sup>-/-</sup>Col8<sup>-/-</sup> mice was slightly higher than for ApoE<sup>-/-</sup> mice (0.016 vs 0.015 N/mm). However, the differences between the two genotypes were not significant. This result did not confirm the findings of Lopes et al.<sup>127</sup>. These authors reported that deficiency of collagen VIII may affect the stability of the plaque by mediating fibrous cap formation. In fact, Lopes et al. 2013<sup>127</sup> observed in their study that collagen VIII in the absence of apoE increases smooth muscle cell proliferation and migration. Consequently, formation of a thicker fibrous cap can be observed in the presence of collagen VIII, and a thinner cap is formed in its absence. A thinner fibrous cap has been previously associated with plaque instability in human patients<sup>59</sup>.

To check whether the duration of Western diet feeding could be a factor explaining these results (i.e., non-significant differences), control ApoE<sup>-/-</sup> mice were compared for two cases. In the first, mice were fed the Western diet for 8 months and in the second they were fed the same diet for 6 months. Wang et al. 2011<sup>4</sup> quantified the rupture resistance of atherosclerotic plaques in ApoE<sup>-/-</sup> mice after 8 months on Western diet, using local delamination experiments and the corresponding local energy release rate (G). In the present study, mice were tested after 6 months on Western diet. G values obtained after 8 months on Western diet, as reported in Wang et al. 2011<sup>4</sup>, varied between 0.005 N/mm and 0.072 N/mm with an average value of 0.024 and SD of 0.018. Figure 3.12 shows the difference in G values between ApoE<sup>-/-</sup> mice fed Western diet for 6 months (present study) vs. 8 months (Wang, et al. 2011). The average G value in the 8- month group (0.024N/mm) was higher than that for the 6-month group (0.015N/mm). This result may be due to the plaque fibrosis (collagen deposition) which would increase the energy required to cause delamination of the plaque (Wang, et al., 2013). Histological studies could determine more accurately the reason for the variation in G values with duration of Western diet feeding. Our study shows that the energy release rate is unaffected by the absence of type VIII collagen and suggests that other types of collagen may be responsible for the differences in adhesion strength previously reported, or simply that the sample size is not sufficiently large to prove the real role of collagen VIII deficiency.

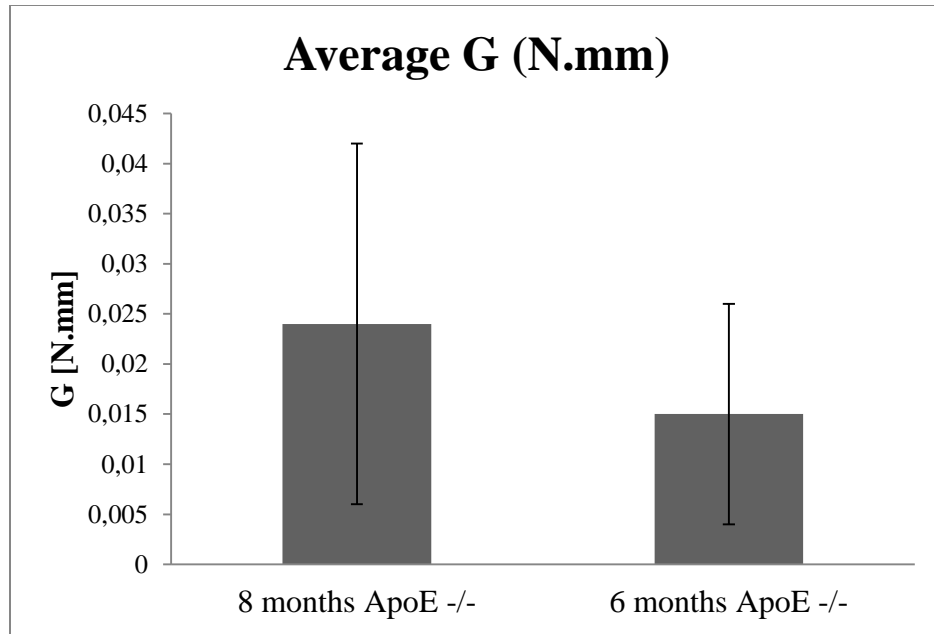


Figure 3.12: Average and standard deviation of the G values obtained for the 8 months and 6 months ApoE<sup>-/-</sup> mouse groups

## II – Discussion of numerical results

In this work we identified for the first time material parameters and cohesive parameters for atherosclerotic plaques in two groups of ApoE<sup>-/-</sup> mice. To accomplish this, we developed an inverse method to calibrate a finite-element model against experimental force/displacement curves. These force/displacement curves were obtained with our specific delamination test<sup>4</sup>.

An explicit time integration scheme was used in these FE simulations for several reasons. Although implicit time integration schemes have shown good agreement with experimental results in one published study<sup>5</sup>, there were still some limitations in modeling contacts and in the selection of a bilinear cohesive law. The presence of more severe contact conditions in our particular model created many convergence issues when using an implicit scheme. Leng et al. 2015<sup>5</sup> simulated the contact between the sample and

the support using springs to avoid direct contacts and thus sidestepped these convergence issues. In our case we used frictionless contact, which was closer to experimental conditions.

In addition, we also observed that some convergence issues occurred at high  $G$  values with implicit resolution. The use of an explicit resolution scheme was able to give acceptable results for all samples despite the high  $G$  values and despite the presence of contacts between the support and the sample. Explicit schemes have been applied in several published studies where cohesive zone models were used to study dissection or fracture in soft biological tissues<sup>84,86,87,89</sup>. Recent studies that reviewed the advantages and limitations of using a cohesive zone model to study fracture showed that a precise determination of material parameters driving the traction-separation relationship is essential for predictive CZM, which justifies the identification of parameters characterizing the traction-separation model and the surrounding material<sup>128, 129, 130, 131</sup>.

The results shown in Figure 3.9 and Figure 3.10 utilize the best-fit parameters identified for a maximum agreement between experiment and simulation. The agreement was acceptable even though some differences remained, especially for the unloading phase. Serrations during the separation phase were always present in the experiments, but they were not reproduced with the implicit scheme<sup>5</sup>. Using the explicit scheme permitted reproducing these serrations during the separation phase. The occurrence of these serrations or the local drop of experimental force values may be explained by the fact that there are fibers bridging the plaque and the underlying artery, and sudden drops in force could be related to fiber breakage. This is not the case numerically, since the fibers were not taken into consideration in this model. Numerically, the serrations represent the

propagation of delamination knowing that each drop in force means that the delamination has propagated a certain length, then the force increases to create another delamination. In summary, the explicit resolution is interesting as a means to simulate the serrations during the separation phase.

In our simulations we reduced the errors in the unloading phase, as is evident in some of the models (161-P1, 157-P1 and 173-P1), by optimizing the application of boundary conditions to represent exactly what was happening in the experiments. However, in some simulations, deviations from the experimental data in the unloading phase could still be observed. These discrepancies could be explained by the fact that a Neo-Hookean strain energy density function was used in our 2D simulations. Leng et al. 2015<sup>5</sup> used a HGO strain energy density function for the material behavior and still had fitting issues for the unloading phase, which tends to confirm that improvements for the unloading phase have to be considered for future work. Moreover, the differences between simulations and experimental data may also be due to the assumptions made for some material parameters. Finally the Neo-Hookean strain energy density function works reasonably well for fitting the data, and this can be attributed to relatively low values of elastic strains preceding the beginning of delamination.

Values in the range [0.02-0.3] MPa were found for the  $C_{10}$  parameter. Assoul et al. 2008<sup>132</sup> identified the elastic moduli of abdominal and thoracic aortas of 2 mm in diameter from adult Wistar rats and found values in the range [0.2-2.8] MPa, which is equivalent to  $C_{10}$  values in the range [0.035-0.5], since in general  $C_{10}=E/6$ . The values obtained for ApoE<sup>-/-</sup> mice were in this range, but the values for ApoE<sup>-/-</sup> Col8<sup>-/-</sup> mice were lower, which could be explained by the absence of collagen type VIII. This result is physiologically

meaningful, as the deficiency of collagen VIII may affect collagen deposition and alter fibrous cap formation, as reported by Lopes et al. 2013<sup>127</sup>. Advanced atherosclerotic plaques typically contain a lipid pool and a fibrous cap. The lipid pool in the atherosclerotic plaque contains several constituents (phospholipids, cholesterol esters, cholesterol crystals and other lipids)<sup>133</sup>. Over time, liquid cholesterol esters may be transformed into a crystalline form, which could lead to a stiffer lipid pool<sup>134</sup>. This phenomenon might also explain the lower plaque stiffness in Col8 deficient mice due to the larger lipid fraction reported for this genotype. Few experimental data on the mechanical properties of lipid pools are available<sup>135</sup>. In our experiments, based on histological analysis, we observed that the lipid pool was always combined with other constituents. It was found using in vitro ultrasound elastography that the average elastic modulus of lipid was  $81 \pm 40$  kPa for 9 human iliac arteries, but increased up to  $1.0 \pm 0.63$  MPa when there was a mixture of smooth muscle cells and collagen fibers with the lipid<sup>136</sup>. Based on this study, we can justify merging the necrotic core and the fibrous cap into a single layer.

Our findings suggest that the adhesion strength of mouse atherosclerotic plaque is not affected by the absence of collagen VIII. We have also shown that the ApoE<sup>-/-</sup> Col8<sup>-/-</sup> plaques are less stiff than the ApoE<sup>-/-</sup> plaques, which may be caused by the lack of type VIII collagen or by impaired migration of SMCs and resulting reduction in matrix deposition, as previously reported.

Notwithstanding these interesting conclusions, refining the model would probably permit reaching a better agreement between experimental and numerical curves. Indeed, the model predictions obtained with the identified parameters have shown some

discrepancies with regard to the experimental results. A 3D geometrical model reconstructed with the actual plaque geometry and an anisotropic nonlinear material model taking into account the regional histology would certainly provide improved accuracy. The CZM technique seems to be a fairly good approach to gain a better understanding of delamination and shows a very good predictive capability in most cases, which is a convincing result for this proof-of concept study. The use of an explicit scheme for simulations allowed us to capture the successive drops in load during the delamination process, but more studies have to be performed to correlate the numerical curves with the experiments by tracking the behavior of both experimental and numerical models in parallel to clearly identify the process leading to these sudden drops in force.

## Section 5 – **Conclusion**

A cohesive zone model (CZM) approach was applied to simulate atherosclerotic plaque delamination experiments. Experiments were carried out on two mouse groups: ApoE<sup>-/-</sup> and Apo<sup>-/-</sup> Col8<sup>-/-</sup>. The experimental results showed that there are non-significant differences in G (critical energy release rate) values between the 2 groups. We then implemented a 2D finite element model in order to have a better understanding of the delamination process. An explicit resolution scheme was used to overcome limitations of implicit resolution methods applied previously to similar problems. An inverse method was used to identify two material parameters: one related to the interface (cohesive parameter) and one elastic parameter related to the plaque constitutive behavior. Results showed a very good agreement between experimental and numerical load-displacement curves after identification of the best-fit parameters. Average values obtained for both parameters revealed that only the elastic parameter could be considered different between

the two groups. Col8<sup>-/-</sup>ApoE<sup>-/-</sup> plaques were less stiff than ApoE<sup>-/-</sup> plaques, which may be attributed to the lack of type VIII collagen or to impaired migration of SMCs and the resulting decrease in matrix deposition<sup>127</sup>. Interfacial properties were non-significantly different. These results suggest that collagen VIII does not play a significant role in determining plaque adhesion strength to the underlying vessel wall. These trends deserve statistical confirmation with more experiments to be performed. Although the present study led to these interesting conclusions, refining the model would probably permit a better agreement between experimental and numerical curves. To this end, we will consider in future studies a refinement of the model by creating 3D finite-element meshes taking into account fiber orientation, and a refinement of the CZM model including regional variations of interfacial properties for a more faithful prediction of the biomechanical response during delamination.

## CHAPTER 4 CONCLUSION AND FUTURE WORK

Despite the existence of many studies on atherosclerotic plaque rupture problems, few were focused on the mechanical process of rupture. The work presented in this thesis had as its objective to use experimental and numerical approaches in order to have a better understanding of the process. For this, an experimental protocol was developed to quantify the energy release rate needed to create delamination in type VIII collagen deficient and non-deficient ApoE<sup>-/-</sup> mice, followed by the creation of a 2D numerical model to simulate the delamination.

This work was preceded by a first numerical study applied to an arterial dissection problem due to the problem similarity, using the coronary arterial dissection data obtained by Wang et al. 2014<sup>3</sup>. In this study, cohesive elements were used to simulate the interface between the dissected layers. The main purpose was to check if the use of an implicit scheme could provide accurate results, and to determine whether the differences between the cohesive parameters in dissection through media and through intima could be considered significant, as observed experimentally on G values between both cases. Results showed that using a cohesive zone model and applying an implicit scheme gave accurate results with some limitations related to convergence in the case of high G values and complex geometrical forms. The cohesive parameters identified were non-significantly different. This result could be explained by the fact that few cycles from each sample were considered due to limitations related to the model. This first result showed that the use of cohesive elements with a simple traction separation law applied to biological tissues was possible, but optimizations had to be implemented to increase the quality of the results

and to ensure convergence while using more complex geometrical forms and in the presence of contacts.

An experimental protocol was then applied on two mouse groups with two different genotypes to quantify the energy release rate  $G$  needed to create the separation between the plaque and the aorta.  $G$  values were compared in both groups, the control group ApoE<sup>-/-</sup> and the group with collagen type VIII deficiency ApoE<sup>-/-</sup> Col8<sup>-/-</sup>. Results showed that there were non-significant differences in  $G$  values between the two mouse groups.

A 2D numerical model was then created using cohesive elements to simulate plaque delamination using an explicit scheme to avoid limitations met in the numerical model for arterial dissection. An inverse method was applied to identify cohesive parameters and Neo-Hookean parameters for the plaque. The aim was to check if the differences between the parameters related to the plaque and to the cohesive elements were different between the two mouse groups. Results showed that  $C_{10}$  values for ApoE<sup>-/-</sup> were higher than  $C_{10}$  for the Col8<sup>-/-</sup> ApoE<sup>-/-</sup> mice. But cohesive parameters were not different. This suggested that collagen type VIII does not play a significant role in determining plaque adhesion strength but may affect the plaque mechanical properties.

Experimentally, the work could be improved by refining the protocol, especially by adding a camera capturing the delamination process from a cross sectional plane of view. This would help to provide a better estimate of some geometrical parameters with more precision to be used in the numerical model. Calculating the area exposed after each cycle of delamination was challenging, thus some improvements are planned in the calculation of this area by using a RGB camera. We also plan to complete this by analyzing histological

pictures (in progress) to have all the elements to understand the delamination process and to correlate G values with microstructure.

All the work presented previously was for the first cycle of each peeling test. Concerning the remaining cycles, a trial of two cycles from one plaque (152-P1) was carried out to check if using the same values obtained after parameter identification could give a good match between the experiments and simulations for the second cycle. The numerical results for two successive cycles are represented in Figure 4.1. While the first cycle was well calibrated, the second cycle was not. This result could be explained by the heterogeneity of the plaque. Cycle 2 had probably a different G value than cycle 1, and considering regional variations of the fracture properties in the numerical model is certainly the most important challenge of our future work.

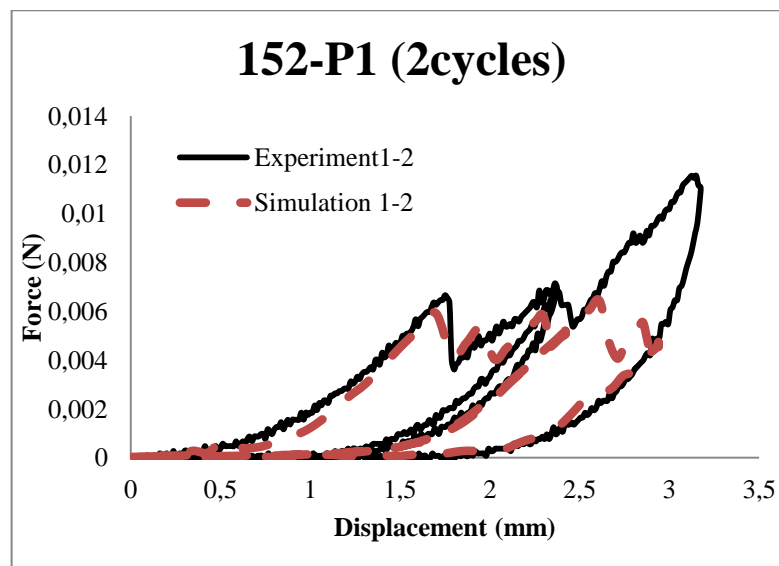


Figure 4.1: Experiment vs numerical load displacement curves for two successive cycles using same material parameter values obtained for the first cycle

Numerically, improvements are also possible to create a more realistic model. Simulations showed that an explicit scheme can give fairly good results, but there is a need to have a more detailed study of all factors that may affect the results, as well as

models with more refined meshes. A 3D model would take into consideration actual fiber orientation and a more realistic material behavior would help to simulate more faithfully the experimental response. Also, the use of the simple bilinear cohesive traction separation law was successful in some cases, but different authors who used cohesive zone models preferred to use alternative forms of cohesive law for more precision. Identification of material parameters was achieved here by calibrating iteratively the models against the experimental curves. This was possible due to the simplicity of the model. If more complex models were used in the future, refined inverse algorithms should be considered for the identification of material parameters<sup>137,138</sup>

## REFERENCES

1. Statistiques sanitaires mondiales. (2012).
2. ALLENDER, S. *et al.* *European cardiovascular disease statistics 2012 edition*.
3. Wang, Y., Johnson, J. A., Spinale, F. G., Sutton, M. A. & Lessner, S. M. Quantitative Measurement of Dissection Resistance in Intimal and Medial Layers of Human Coronary Arteries. *Exp. Mech.* **54**, 677–683 (2014).
4. Wang, Y., Ning, J., Johnson, J. A., Sutton, M. A. & Lessner, S. M. Development of a quantitative mechanical test of atherosclerotic plaque stability. *J. Biomech.* **44**, 2439–2445 (2011).
5. Leng, X., Chen, X., Deng, X., Sutton, M. A. & Lessner, S. M. Modeling of Experimental Atherosclerotic Plaque Delamination. *Ann. Biomed. Eng.* **43**, 2838–2851 (2015).
6. Toussaint, J.-F. *L'athérosclérose: physiopathologie, diagnostics, thérapeutiques*. (Elsevier Masson, 2003).
7. Fung, Y. C. *Biomechanics: Mechanical Properties of Living Tissues*. (Springer Science & Business Media, 2013).
8. Hayashi, K. Experimental approaches on measuring the mechanical properties and constitutive laws of arterial walls. *J. Biomech. Eng.* **115**, 481–488 (1993).
9. Watton, P. N., Ventikos, Y. & Holzapfel, G. A. Modelling the mechanical response of elastin for arterial tissue. *J. Biomech.* **42**, 1320–1325 (2009).
10. Delalleau, A. *Analyse du comportement mécanique de la peau in vivo*. (Saint-Etienne, 2007).
11. Wiley: Principles of Anatomy and Physiology, 14th Edition - Gerard J. Tortora, Bryan H. Derrickson. Available at:

<http://eu.wiley.com/WileyCDA/WileyTitle/productCd-EHEP002935.html>.

(Accessed: 7th July 2015)

12. Humphrey, J. D. *Cardiovascular Solid Mechanics: Cells, Tissues, and Organs*. (Springer Science & Business Media, 2002).
13. Mancini, G. B. J., Dahlöf, B. & Díez, J. Surrogate Markers for Cardiovascular Disease Structural Markers. *Circulation* **109**, IV–22–IV–30 (2004).
14. Ross, R. The Pathogenesis of Atherosclerosis — An Update. *N. Engl. J. Med.* **314**, 488–500 (1986).
15. Tóth, P. P. An urgent matter-identifying your patients' cardiovascular risk and improving their outcomes. Atherosclerosis: the underlying disease. *J. Fam. Pract.* **58**, S19–25 (2009).
16. McGill, H. C., McMahan, C. A. & Gidding, S. S. Preventing Heart Disease in the 21st Century Implications of the Pathobiological Determinants of Atherosclerosis in Youth (PDAY) Study. *Circulation* **117**, 1216–1227 (2008).
17. Crowther, M. A. Pathogenesis of atherosclerosis. *Hematol. Educ. Program Am. Soc. Hematol. Am. Soc. Hematol. Educ. Program* 436–441 (2005). doi:10.1182/asheducation-2005.1.436
18. Ross, R. Atherosclerosis--an inflammatory disease. *N. Engl. J. Med.* **340**, 115–126 (1999).
19. Vengrenyuk, Y. *et al.* A hypothesis for vulnerable plaque rupture due to stress-induced debonding around cellular microcalcifications in thin fibrous caps. *Proc. Natl. Acad. Sci.* **103**, 14678–14683 (2006).
20. Nadkarni, S. K., Bouma, B. E., de Boer, J. & Tearney, G. J. Evaluation of collagen in atherosclerotic plaques: the use of two coherent laser-based imaging methods. *Lasers Med. Sci.* **24**, 439–445 (2009).

21. Fratzl, P. in *Collagen* (ed. Fratzl, P.) 1–13 (Springer US, 2008).
22. Wight, T. The vascular extracellular matrix. *Atheroscler. Coron. Artery Dis.* **1**, 421–440 (1996).
23. Prockop, D. J. & Kivirikko, K. I. Collagens: molecular biology, diseases, and potentials for therapy. *Annu. Rev. Biochem.* **64**, 403–434 (1995).
24. Kadler, K. Extracellular matrix 1: Fibril-forming collagens. *Protein Profile* **2**, 491–619 (1995).
25. Hulmes, D. J. S. Building collagen molecules, fibrils, and suprafibrillar structures. *J. Struct. Biol.* **137**, 2–10 (2002).
26. Rekhter, M. D. Collagen synthesis in atherosclerosis: too much and not enough. *Cardiovasc. Res.* **41**, 376–384 (1999).
27. Shekhonin, B. V., Domogatsky, S. P., Idelson, G. L., Koteliansky, V. E. & Rukosuev, V. S. Relative distribution of fibronectin and type I, III, IV, V collagens in normal and atherosclerotic intima of human arteries. *Atherosclerosis* **67**, 9–16 (1987).
28. Murata, K., Motayama, T. & Kotake, C. Collagen types in various layers of the human aorta and their changes with the atherosclerotic process. *Atherosclerosis* **60**, 251–262 (1986).
29. Ooshima, A. & Muragaki, Y. Collagen Metabolism in Atherogenesis. *Ann. N. Y. Acad. Sci.* **598**, 582–584 (1990).
30. Katsuda, S. *et al.* Collagens in human atherosclerosis. Immunohistochemical analysis using collagen type-specific antibodies. *Arterioscler. Thromb. J. Vasc. Biol. Am. Heart Assoc.* **12**, 494–502 (1992).

31. Suttmuller, M., Bruijn, J. A. & de Heer, E. Collagen types VIII and X, two non-fibrillar, short-chain collagens. Structure homologies, functions and involvement in pathology. *Histol. Histopathol.* **12**, 557–566 (1997).
32. Lopes, J. *et al.* Type VIII Collagen Mediates Vessel Wall Remodeling after Arterial Injury and Fibrous Cap Formation in Atherosclerosis. *Am. J. Pathol.* **182**, 2241–2253 (2013).
33. Scheider, I. Micromechanical based derivation of traction-separation laws for cohesive model simulations. *Procedia Eng.* **1**, 17–21 (2009).
34. Scheider, I. & Brocks, W. The Effect of the Traction Separation Law on the Results of Cohesive Zone Crack Propagation Analyses. *Key Eng. Mater.* **251-252**, 313–318 (2003).
35. Masson, I. Contribution à la modélisation mécanique du comportement dynamique, hyperélastique et anisotrope de la paroi artérielle. (Université Paris-Est, 2008).
36. Demiray, H., Weizsäcker, H. W., Pascale, K. & Erbay, H. A. A stress-strain relation for a rat abdominal aorta. *J. Biomech.* **21**, 369–374 (1988).
37. Burton, A. C. Relation of structure to function of the tissues of the wall of blood vessels. *Physiol. Rev.* **34**, 619–642 (1954).
38. Tickner, E. G. & Sacks, A. H. A theory for the static elastic behavior of blood vessels. *Biorheology* **4**, 151–168 (1967).
39. Patel, D. J. & Fry, D. L. The elastic symmetry of arterial segments in dogs. *Circ. Res.* **24**, 1–8 (1969).
40. Chuong, C. J. & Fung, Y. C. On Residual Stresses in Arteries. *J. Biomech. Eng.* **108**, 189–192 (1986).

41. Saini, A., Berry, C. & Greenwald, S. Effect of age and sex on residual stress in the aorta. *J. Vasc. Res.* **32**, 398–405 (1995).
42. Cardamone, L., Valentín, A., Eberth, J. F. & Humphrey, J. D. Origin of axial prestretch and residual stress in arteries. *Biomech. Model. Mechanobiol.* **8**, 431–446 (2009).
43. *McDonald's Blood Flow in Arteries, Sixth Edition: Theoretical, Experimental and Clinical Principles.*
44. Skalak, R. *et al.* Analytical description of growth. *J. Theor. Biol.* **94**, 555–577 (1982).
45. Takamizawa, K. & Hayashi, K. Strain energy density function and uniform strain hypothesis for arterial mechanics. *J. Biomech.* **20**, 7–17 (1987).
46. Liu, S. Q. & Fung, Y. C. Zero-stress states of arteries. *J. Biomech. Eng.* **110**, 82–84 (1988).
47. Han, H. C. & Fung, Y. C. Species dependence of the zero-stress state of aorta: pig versus rat. *J. Biomech. Eng.* **113**, 446–451 (1991).
48. Stergiopoulos, N., Pannatier, A., Rachev, A., Greenwald, S. E. & Meister, J.-J. Assessment of Mechanical Homogeneity of the Arterial Wall by an Artery-Inversion Test. *Cardiovasc. Eng. Int. J.* **1**, 31–36 (2001).
49. Speelman, L. *et al.* Initial stress in biomechanical models of atherosclerotic plaques. *J. Biomech.* **44**, 2376–2382 (2011).
50. Schievink, W. I. Spontaneous dissection of the carotid and vertebral arteries. *N. Engl. J. Med.* **344**, 898–906 (2001).
51. Sommer, G., Gasser, T. C., Regitnig, P., Auer, M. & Holzapfel, G. A. Dissection properties of the human aortic media: an experimental study. *J. Biomech. Eng.* **130**, 021007 (2008).

52. Pratt, B. & Curci, J. Arterial elastic fiber structure. Function and potential roles in acute aortic dissection. *J. Cardiovasc. Surg. (Torino)* **51**, 647–656 (2010).
53. Celik, S. K. *et al.* Primary spontaneous coronary artery dissections in atherosclerotic patients. Report of nine cases with review of the pertinent literature. *Eur. J. Cardio-Thorac. Surg. Off. J. Eur. Assoc. Cardio-Thorac. Surg.* **20**, 573–576 (2001).
54. Vrints, C. J. M. Spontaneous coronary artery dissection. *Heart* **96**, 801–808 (2010).
55. Tong, J., Sommer, G., Regitnig, P. & Holzapfel, G. A. Dissection properties and mechanical strength of tissue components in human carotid bifurcations. *Ann. Biomed. Eng.* **39**, 1703–1719 (2011).
56. Pasta, S., Phillippi, J. A., Gleason, T. G. & Vorp, D. A. Effect of aneurysm on the mechanical dissection properties of the human ascending thoracic aorta. *J. Thorac. Cardiovasc. Surg.* **143**, 460–467 (2012).
57. Kolodgie, F. D. *et al.* The thin-cap fibroatheroma: a type of vulnerable plaque: the major precursor lesion to acute coronary syndromes. *Curr. Opin. Cardiol.* **16**, 285–292 (2001).
58. Richardson, P. D., Davies, M. J. & Born, G. V. Influence of plaque configuration and stress distribution on fissuring of coronary atherosclerotic plaques. *Lancet Lond. Engl.* **2**, 941–944 (1989).
59. Virmani, R., Narula, J., Leon, M. B. & Willerson, J. T. *The Vulnerable Atherosclerotic Plaque: Strategies for Diagnosis and Management.* (John Wiley & Sons, 2008).

60. Rosenfeld, M. E. & Schwartz, S. M. in *The Vulnerable Atherosclerotic Plaque* (eds. MD, R. V., MD, J. N., MD, Martin B. L. & MD, J. T. W.) 105–127 (Blackwell Publishing, 2006).
61. Rosenfeld, M. E. *et al.* Advanced atherosclerotic lesions in the innominate artery of the ApoE knockout mouse. *Arterioscler. Thromb. Vasc. Biol.* **20**, 2587–2592 (2000).
62. Riou, L. M. *et al.* Effects of mechanical properties and atherosclerotic artery size on biomechanical plaque disruption – Mouse vs. human. *J. Biomech.* **47**, 765–772 (2014).
63. Loree, H. M., Kamm, R. D., Stringfellow, R. G. & Lee, R. T. Effects of fibrous cap thickness on peak circumferential stress in model atherosclerotic vessels. *Circ. Res.* **71**, 850–858 (1992).
64. Cheng, G. C., Loree, H. M., Kamm, R. D., Fishbein, M. C. & Lee, R. T. Distribution of circumferential stress in ruptured and stable atherosclerotic lesions. A structural analysis with histopathological correlation. *Circulation* **87**, 1179–1187 (1993).
65. Lendon, C. L., Davies, M. J., Born, G. V. & Richardson, P. D. Atherosclerotic plaque caps are locally weakened when macrophages density is increased. *Atherosclerosis* **87**, 87–90 (1991).
66. Loree, H. M. *et al.* Mechanical properties of model atherosclerotic lesion lipid pools. *Arterioscler. Thromb. J. Vasc. Biol. Am. Heart Assoc.* **14**, 230–234 (1994).
67. Holzapfel, G. A., Sommer, G. & Regitnig, P. Anisotropic mechanical properties of tissue components in human atherosclerotic plaques. *J. Biomech. Eng.* **126**, 657–665 (2004).

68. Majdouline, Y. *et al.* Endovascular Shear Strain Elastography for the Detection and Characterization of the Severity of Atherosclerotic Plaques: In Vitro Validation and In Vivo Evaluation. *Ultrasound Med. Biol.* **40**, 890–903 (2014).
69. Deleaval, F. *et al.* The Intravascular Ultrasound Elasticity-Palpography Technique Revisited: A Reliable Tool for the In Vivo Detection of Vulnerable Coronary Atherosclerotic Plaques. *Ultrasound Med. Biol.* **39**, 1469–1481 (2013).
70. Le Floc’h, S. *et al.* A Four-Criterion Selection Procedure for Atherosclerotic Plaque Elasticity Reconstruction Based on in Vivo Coronary Intravascular Ultrasound Radial Strain Sequences. *Ultrasound Med. Biol.* **38**, 2084–2097 (2012).
71. Bank, A. J., Versluis, A., Dodge, S. M. & Douglas, W. H. Atherosclerotic plaque rupture: a fatigue process? *Med. Hypotheses* **55**, 480–484 (2000).
72. Versluis, A., Bank, A. J. & Douglas, W. H. Fatigue and plaque rupture in myocardial infarction. *J. Biomech.* **39**, 339–347 (2006).
73. Gasser, T. C. & Holzapfel, G. A. Modeling the propagation of arterial dissection. *Eur. J. Mech. - ASolids* **25**, 617–633 (2006).
74. Dugdale, D. Yielding of steel sheets containing slits. *J. Mech. Phys. Solids* **8**, 100–104 (1960).
75. Barenblatt, G. . The mathematical theory of equilibrium cracks in brittle fracture. *Adv. Appl. Mech.* **7** 55–129 (1962).
76. Hillerborg, A., Modéer, M. & Petersson, P.-E. Analysis of crack formation and crack growth in concrete by means of fracture mechanics and finite elements. *Cem. Concr. Res.* **6**, 773–781 (1976).
77. Gasser, T. C. & Holzapfel, G. A. Modeling plaque fissuring and dissection during balloon angioplasty intervention. *Ann. Biomed. Eng.* **35**, 711–723 (2007).

78. Chenu, P. *et al.* Resistance of the atherosclerotic plaque during coronary angioplasty: a multivariate analysis of clinical and angiographic variables. *Cathet. Cardiovasc. Diagn.* **29**, 203–209 (1993).
79. Chu, B., Gaillard, E., Mongrain, R., Reiter, S. & Tardif, J.-C. Characterization of fracture toughness exhaustion in pig aorta. *J. Mech. Behav. Biomed. Mater.* **17**, 126–136 (2013).
80. Ferracane, J. L. & Berge, H. X. Fracture toughness of experimental dental composites aged in ethanol. *J. Dent. Res.* **74**, 1418–1423 (1995).
81. Carson, M. W. & Roach, M. R. The strength of the aortic media and its role in the propagation of aortic dissection. *J. Biomech.* **23**, 579–588 (1990).
82. Roach, M. R. & Song, S. H. Variations in strength of the porcine aorta as a function of location. *Clin. Invest. Med.* **17**, 308–318 (1994).
83. Ferrara, A. & Pandolfi, A. Numerical modelling of fracture in human arteries. *Comput. Methods Biomech. Biomed. Engin.* **11**, 553–567 (2008).
84. Ferrara, A. & Pandolfi, A. A numerical study of arterial media dissection processes. *Int. J. Fract.* **166**, 21–33 (2010).
85. Gasser, T. C. & Holzapfel, G. A. Modeling the propagation of arterial dissection. *Eur. J. Mech. - ASolids* **25**, 617–633 (2006).
86. Gasser, T. C. & Holzapfel, G. A. Geometrically non-linear and consistently linearized embedded strong discontinuity models for 3D problems with an application to the dissection analysis of soft biological tissues. *Comput. Methods Appl. Mech. Eng.* **192**, 5059–5098 (2003).
87. Caballero, A. & Molinari, J. F. Finite element simulations of kidney stones fragmentation by direct impact: Tool geometry and multiple impacts. *Int. J. Eng. Sci.* **48**, 253–264 (2010).

88. Badel, P., Avril, S., Sutton, M. A. & Lessner, S. M. Numerical simulation of arterial dissection during balloon angioplasty of atherosclerotic coronary arteries. *J. Biomech.* **47**, 878–889 (2014).
89. Untaroiu, C. D., Lu, Y.-C., Siripurapu, S. K. & Kemper, A. R. Modeling the biomechanical and injury response of human liver parenchyma under tensile loading. *J. Mech. Behav. Biomed. Mater.* **41**, 280–291 (2015).
90. Waller, B. F. Topography of atherosclerotic coronary artery disease. *Clin. Cardiol.* **13**, 435–442 (1990).
91. Eberth, J. F., Cardamone, L. & Humphrey, J. D. Evolving biaxial mechanical properties of mouse carotid arteries in hypertension. *J. Biomech.* **44**, 2532–2537 (2011).
92. Holzapfel, G. A. & Ogden, R. W. *Biomechanics of Soft Tissue in Cardiovascular Systems*. (Springer, 2003).
93. Holzapfel, G. A., Sommer, G., Gasser, C. T. & Regitnig, P. Determination of layer-specific mechanical properties of human coronary arteries with nonatherosclerotic intimal thickening and related constitutive modeling. *Am. J. Physiol. Heart Circ. Physiol.* **289**, H2048–2058 (2005).
94. Holzapfel, G. A. Determination of material models for arterial walls from uniaxial extension tests and histological structure. *J. Theor. Biol.* **238**, 290–302 (2006).
95. Hillerborg, A., Modeer, M. & Petersson, P. E. Analysis of crack formation and crack growth in concrete by means of F.N. and finite elements. *Cem. Concr. Res.* **6**, (1976).
96. Hill, M. R., Duan, X., Gibson, G. A., Watkins, S. & Robertson, A. M. A theoretical and non-destructive experimental approach for direct inclusion of

- measured collagen orientation and recruitment into mechanical models of the artery wall. *J. Biomech.* **45**, 762–771 (2012).
97. Yosibash, Z. & Priel, E. Artery active mechanical response: High order finite element implementation and investigation. *Comput. Methods Appl. Mech. Eng.* **237–240**, 51–66 (2012).
98. Chai, C.-K. *et al.* Local axial compressive mechanical properties of human carotid atherosclerotic plaques-characterisation by indentation test and inverse finite element analysis. *J. Biomech.* **46**, 1759–1766 (2013).
99. Le Floc’h, S. *et al.* Vulnerable atherosclerotic plaque elasticity reconstruction based on a segmentation-driven optimization procedure using strain measurements: theoretical framework. *IEEE Trans. Med. Imaging* **28**, 1126–1137 (2009).
100. Merei, B., Avril, S., Badel, P., Sutton, M. A. & Lessner, S. M. Numerical study of delamination through human aortic media using cohesive elements and two different material laws: linear elastic and hyperelastic. in (Mira Digital Publishing, 2012).
101. Carlos, G. D. & Cheryl, A. R. with Kyongchan. Guidelines and Parameter Selection for the Simulation of Progressive Delamination. (2008).
102. Holzapfel, G. A., Gasser, T. C. & Ogden, R. W. A New Constitutive Framework for Arterial Wall Mechanics and a Comparative Study of Material Models. *J. Elast. Phys. Sci. Solids* **61**, 1–48 (2000).
103. Holzapfel, G. A., Gasser, T. C. & Stadler, M. A structural model for the viscoelastic behavior of arterial walls: Continuum formulation and finite element analysis. *Eur. J. Mech. - ASolids* **21**, 441–463 (2002).

104. Holzapfel, G. A., Sommer, G., Auer, M., Regitnig, P. & Ogden, R. W. Layer-specific 3D residual deformations of human aortas with non-atherosclerotic intimal thickening. *Ann. Biomed. Eng.* **35**, 530–545 (2007).
105. Learoyd, B. M. & Taylor, M. G. Alterations with age in the viscoelastic properties of human arterial walls. *Circ. Res.* **18**, 278–292 (1966).
106. Langewouters, G. J., Wesseling, K. H. & Goedhard, W. J. The static elastic properties of 45 human thoracic and 20 abdominal aortas in vitro and the parameters of a new model. *J. Biomech.* **17**, 425–435 (1984).
107. Dinardo, C. L. *et al.* Variation of mechanical properties and quantitative proteomics of VSMC along the arterial tree. *Am. J. Physiol. Heart Circ. Physiol.* **306**, H505–516 (2014).
108. Ahsan, T. & Sah, R. L. Biomechanics of integrative cartilage repair. *Osteoarthr. Cartil. OARS Osteoarthr. Res. Soc.* **7**, 29–40 (1999).
109. Maurice, D. M. & Monroe, F. Cohesive strength of corneal lamellae. *Exp. Eye Res.* **50**, 59–63 (1990).
110. Dong, C. *et al.* Development of a device for measuring adherence of skin grafts to the wound surface. *Ann. Biomed. Eng.* **21**, 51–55 (1993).
111. Roach, M. R. & Song, S. H. Variations in strength of the porcine aorta as a function of location. *Clin. Invest. Med.* **17**, 308–318 (1994).
112. Zhang, S. H., Reddick, R. L., Piedrahita, J. A. & Maeda, N. Spontaneous hypercholesterolemia and arterial lesions in mice lacking apolipoprotein E. *Science* **258**, 468–471 (1992).
113. Nakashima, Y., Plump, A. S., Raines, E. W., Breslow, J. L. & Ross, R. ApoE-deficient mice develop lesions of all phases of atherosclerosis throughout the arterial tree. *Arterioscler. Thromb. Vasc. Biol.* **14**, 133–140 (1994).

114. Pendse, A. A., Arbones-Mainar, J. M., Johnson, L. A., Altenburg, M. K. & Maeda, N. Apolipoprotein E knock-out and knock-in mice: atherosclerosis, metabolic syndrome, and beyond. *J. Lipid Res.* **50**, S178–S182 (2008).
115. An, B., Zhao, X., Arola, D. & Zhang, D. Fracture analysis for biological materials with an expanded cohesive zone model. *J. Biomech.* **47**, 2244–2248 (2014).
116. Ural, A. Prediction of Colles' fracture load in human radius using cohesive finite element modeling. *J. Biomech.* **42**, 22–28 (2009).
117. Ural, A. & Vashishth, D. Anisotropy of age-related toughness loss in human cortical bone: A finite element study. *J. Biomech.* **40**, 1606–1614 (2007).
118. Ural, A. Cohesive modeling of bone fracture at multiple scales. *Procedia Eng.* **10**, 2827–2832 (2011).
119. Sibinga, N. E. *et al.* Collagen VIII is expressed by vascular smooth muscle cells in response to vascular injury. *Circ. Res.* **80**, 532–541 (1997).
120. Plenz, G., Dorszewski, A., Breithardt, G. & Robenek, H. Expression of type VIII collagen after cholesterol diet and injury in the rabbit model of atherosclerosis. *Arterioscler. Thromb. Vasc. Biol.* **19**, 1201–1209 (1999).
121. Analysis User's Manual Version 6.13. *ABAQUS*. (Dassault Systemes Corp, 2013).
122. Chen, X., Deng, X. & Sutton, M. A. Simulation of stable tearing crack growth events using the CZM approach with an explicit solver. *Finite Elem. Anal. Des.* **81**, 32–37 (2014).
123. Pagani, M. & Perego, U. Explicit dynamics simulation of blade cutting of thin elastoplastic shells using 'directional' cohesive elements in solid-shell finite element models. *Comput. Methods Appl. Mech. Eng.* **285**, 515–541 (2015).

124. Gregersen, H., Zhao, J., Lu, X., Zhou, J. & Falk, E. Remodelling of the zero-stress state and residual strains in apoE-deficient mouse aorta. *Biorheology* **44**, 75–89 (2007).
125. Teng, Z. *et al.* Material properties of components in human carotid atherosclerotic plaques: A uniaxial extension study. *Acta Biomater.* **10**, 5055–5063 (2014).
126. Song, K., Davila, C. G. & Rose, C. A. Guidelines and Parameter Selection for the Simulation of Progressive Delamination. (2008).
127. Lopes, J. *et al.* Type VIII Collagen Mediates Vessel Wall Remodeling after Arterial Injury and Fibrous Cap Formation in Atherosclerosis. *Am. J. Pathol.* **182**, 2241–2253 (2013).
128. Elices, M., Guinea, G. V., Gómez, J. & Planas, J. The cohesive zone model: advantages, limitations and challenges. *Eng. Fract. Mech.* **69**, 137–163 (2002).
129. Chandra, N., Li, H., Shet, C. & Ghonem, H. Some issues in the application of cohesive zone models for metal–ceramic interfaces. *Int. J. Solids Struct.* **39**, 2827–2855 (2002).
130. Kyoungsoo Park, G. H. P. Adaptive mesh refinement and coarsening for cohesive zone modeling of dynamic fracture. *Int. J. Numer. Methods Eng.* **92**, 1–35 (2012).
131. Wang, J. T. Investigating Some Technical Issues on Cohesive Zone Modeling of Fracture. *J. Eng. Mater. Technol.* **135**, 011003–011003 (2012).
132. Assoul, N., Flaud, P., Chaouat, M., Letourneur, D. & Bataille, I. Mechanical properties of rat thoracic and abdominal aortas. *J. Biomech.* **41**, 2227–2236 (2008).

133. Smith, E. B. & Slater, R. S. The microdissection of large atherosclerotic plaques to give morphologically and topographically defined fractions for analysis: Part 1. The lipids in the isolated fractions. *Atherosclerosis* **15**, 37–56 (1972).
134. Small, D. M. George Lyman Duff memorial lecture. Progression and regression of atherosclerotic lesions. Insights from lipid physical biochemistry. *Arterioscler. Dallas Tex* **8**, 103–129 (1988).
135. Akyildiz, A. C., Speelman, L. & Gijsen, F. J. H. Mechanical properties of human atherosclerotic intima tissue. *J. Biomech.* **47**, 773–783 (2014).
136. Kanai, H., Hasegawa, H., Ichiki, M., Tezuka, F. & Koiwa, Y. Elasticity Imaging of Atheroma With Transcutaneous Ultrasound Preliminary Study. *Circulation* **107**, 3018–3021 (2003).
137. Acosta Santamaría, V. *et al.* Material model calibration from planar tension tests on porcine linea alba. *J. Mech. Behav. Biomed. Mater.* **43**, 26–34 (2015).
138. Badel, P., Rohan, C. P.-Y. & Avril, S. Finite Element simulation of buckling-induced vein tortuosity and influence of the wall constitutive properties. *J. Mech. Behav. Biomed. Mater.* **26**, 119–126 (2013).

## CHAPTER 5 APPENDIX

### Appendix 1

Abstract accepted at the Biomedical Engineering Society 2012 Annual Meeting. (Co-authors: Stephane Avril, Pierre Badel, Michael Sutton, Susan Lessner)

**Introduction:** Traumatic arterial dissection results in separation of the different layers of the arterial wall, with the creation of a false lumen. Separation could occur between arterial layers or within the layers. The energy release rate during separation is defined as the difference between the variation of total energy applied with respect to the crack length ( $\Delta T/\Delta a$ ) and the variation of the stored energy (strain energy) with respect to crack length ( $\Delta S/\Delta a$ ) (Griffith's energy balance). In order to explore the dissection properties of human coronary arteries, experimental peeling tests were performed. Using measured load-displacement curves, the fracture energy was calculated as the incremental area under the load-displacement curves, neglecting the contribution of the strain energy. The aim of this study is to determine conditions when the contribution of strain energy can properly be neglected in our experimental system. To do so, finite element simulations that incorporate cohesive elements to represent the fracture interface were performed in an effort to better estimate the fracture energy using our experimental curves.

**Materials and Methods:** The model used for simulations is a 2D model of an opened segment of human coronary artery, 0.4mm thick and 8mm long, with the

media comprising the upper two-thirds and the adventitia the lower third of the vessel wall. The media itself is composed of two layers of equal thickness, separated by a zero-thickness layer of cohesive elements, defining an upper part (media) and lower part (adventitia and media) of the specimen. A linear elastic model is used for both the media and adventitia, using as Young's modulus and Poisson's ratio 0.8MPa and 0.45 for the media, and 0.4MPa and 0.45 for the adventitia, respectively. The assumed cohesive zone law is a bilinear function (traction-separation law) with  $G_c$  values of 0.01, 0.005 and 0.0025N/mm for the simulations, which fall within the range of values obtained experimentally during peeling of human coronary artery media. The cohesive parameters defined are the stiffness (K) of the elastic part, the maximum stress at separation (corresponding to a separation value  $U_0$ ), and the maximum separation value corresponding to total damage of the cohesive element ( $U_f$ ). Boundary conditions imposed on the specimen include clamping of the bottom edge and a horizontal displacement condition applied on the left edge of the upper part. To simulate the initial flaw, a material separation is created at the left edge between the media layers before beginning the peeling simulation, consistent with our experiments.

**Results and Discussion:** To ensure convergence, we performed a parametric study of cohesive parameters, which indicated that these parameters should meet certain conditions: K should be in the same range as the stiffness values of the surrounding bulk material, and the ratio  $U_f/U_0$  should be on the order of 100. Figure 5.1(a) shows the strain energy and total energy vs crack length for  $G_c=0.0025$  N/mm (a) Figure 5.1(b) presents the average ratio of  $(\Delta S/\Delta a) / (\Delta T/\Delta a)$  with respect to the critical fracture energy values over a total crack length of 2mm for the three  $G_c$

values. This ratio decreases with increasing values of critical fracture energy. The variation of strain energy constitutes 6% of the variation of the total energy applied with respect to the variation of the crack length for  $G_c=0.0025\text{N/mm}$ , decreasing to 4.5% for  $G_c=0.01\text{ N/mm}$ . Previous studies by Wang, et al. 2011 estimated that the strain energy constitutes 10% of the total energy. This numerical study confirms that the variation of strain energy with respect to crack length can be reasonably neglected compared to the variation of total energy with respect to crack length, particularly at  $G_c$  values of 0.005 N/mm and above.

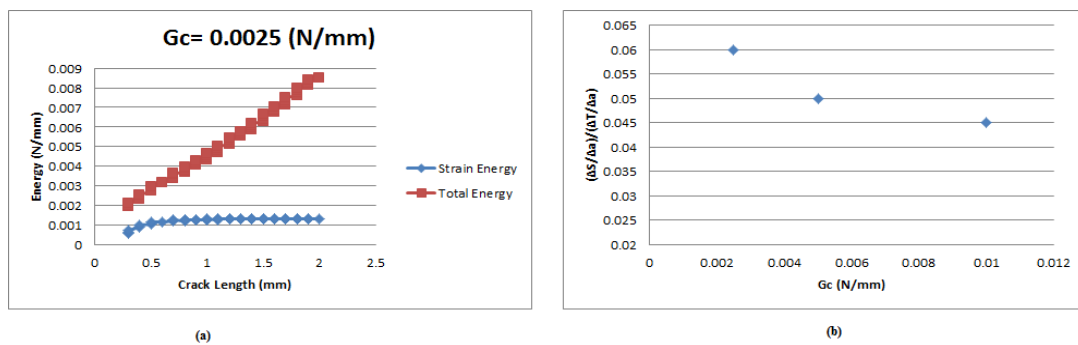


Figure 5.1: (a) Example of the strain energy and the total energy curves vs crack length, for  $G_c = 0.0025\text{ N/mm}$  (b) the average ratio of  $(\Delta S/\Delta a) / (\Delta T/\Delta a)$  vs.  $G_c$  values

**Conclusions:** A numerical study using the cohesive element technique was performed to estimate the contribution of the strain energy during experimental arterial dissection. The results obtained show that the contribution of strain energy to total energy required for dissection becomes relatively more important as fracture energy,  $G_c$  decreases. This result can be applied to our future experiments studying the delamination of atherosclerotic plaques to provide a criterion for neglecting the contribution of strain energy.

## Appendix 2

After applying the experimental protocol described above, the  $\Delta A$ ,  $\Delta E$  and G values are reported for every cycle in Table 5.1 for the control and in Table 5.2 for the type VIII collagen deficient. Cycles for which there was no crack propagation or cycles for which the newly exposed area could not be measured with enough accuracy are not reported.

Table 5.1:  $\Delta A$ ,  $\Delta E$  and G values for the ApoE<sup>-/-</sup> mouse group

Mouse	Plaque & Cycle number	Average A (mm <sup>2</sup> )	E (J)	G (J/m <sup>2</sup> )
12-A-124	P1_C2	1.62E-01	6.44E-06	39.78
12-A-124	P1_C3	6.11E-01	3.68E-06	6.02
12-A-124	P1_C4	1.89E-01	7.84E-06	41.50
12-A-124	P1_C7	8.30E-02	1.10E-06	13.28
12-A-124	P1_C8	2.66E-01	5.06E-06	19.04
12-A-124	P1_C11	4.52E-01	3.77E-06	8.36
12-A-124	P1_C5	5.36E-01	5.44E-06	10.15
13-A-145	P1_C2	1.96E-01	3.16E-06	16.14
13-A-145	P1_C3	4.97E-01	3.99E-06	8.03
13-A-157	P2_C2	3.66E-01	6.76E-06	18.47
13-A-157	P2_C3	3.51E-01	1.21E-05	34.45
13-A-158	P1_C2	5.01E-01	5.44E-06	10.86
13-A-158	P1_C3	7.07E-01	6.04E-06	8.54
13-A-158	P1_C4	1.11E-01	5.96E-06	53.90
13-A-161	P1_C4	1.12E-01	2.01E-06	18.03
13-A-161	P1_C6	6.47E-01	9.16E-06	14.17
13-A-161	P2_C2	1.16E-01	3.73E-06	32.28
13-A-161	P2_C3	2.44E+00	1.00E-05	4.11
13-A-161	P2_C4	1.09E+00	7.26E-06	6.66

<b>13-A-161</b>	P2_C5	2.23E+00	1.01E-05	4.55
-----------------	-------	----------	----------	------

Table 5.2:  $\Delta A$ ,  $\Delta E$  and G values for the ApoE<sup>-/-</sup> Col8<sup>-/-</sup> mouse group

Mouse	Plaque & Cycle number	Average A (mm <sup>2</sup> )	E (J)	G (J/m <sup>2</sup> )
<b>13-C8A-150</b>	P1_C3	3.07 E-01	2.99 E-06	9.75
<b>13-C8A-151</b>	P1_C2	2.49 E-01	8.23 E-06	33.05
<b>13-C8A-151</b>	P1_C3	4.11 E-01	8.45 E-06	20.57
<b>13-C8A-152</b>	P1_C3	1.6 E-01	1.12 E-06	7.01
<b>13-C8A-152</b>	P1_C4	3.215 E-01	2.94 E-06	9.17
<b>13-C8A-157</b>	P1_C3	1.4165 E-01	10.62 E-06	7.49
<b>13-C8A-157</b>	P1_C4	6.065 E-01	8.91 E-06	14.70
<b>13-C8A-173</b>	P1_C3	5.28 E-01	10.45 E-06	19.79
<b>13-C8A-173</b>	P1_C5	3.76 E-01	4.97 E-06	13.24
<b>13-C8A-173</b>	P1_C6	2.23 E-01	7.08 E-06	31.75
<b>13-C8A-174</b>	P1_C3	4.95 E-01	7.75 E-06	15.65
<b>13-C8A-174</b>	P2_C6	4. E-01	6.04 E-06	15.10
<b>13-C8A-174</b>	P2_C7	2.7 E-01	0.81 E-06	3.013
<b>13-C8A-174</b>	P2_C9	3.135 E-01	2.35 E-06	7.52
<b>13-C8A-174</b>	P2_C10	1.26 E-01	1.61 E-06	12.83
<b>13-C8A-174</b>	P2_C11	1.99 E-01	1.40 E-06	7.04
<b>13-C8A-174</b>	P3_C3	6.545 E-01	6.23 E-06	9.53
<b>13-C8A-174</b>	P3_C4	2.7 E-01	1.77 E-06	6.57
<b>13-C8A-174</b>	P3_C5	4.855 E-01	3.39 E-06	6.99
<b>13-C8A-174</b>	P3_C7	4.435 E-01	5.78 E-06	13.04
<b>13-C8A-175</b>	P1_C3	2.59 E-01	2.55 E-06	9.84
<b>13-C8A-175</b>	P1_C4	1.105 E-01	3.94 E-06	35.71
<b>13-C8A-175</b>	P1_C5	4.955 E-01	5.15 E-06	10.40

## Appendix 3

The load vs displacement curves related to each plaque are represented in Figure 5.2, Figure 5.3 and Figure 5.4.

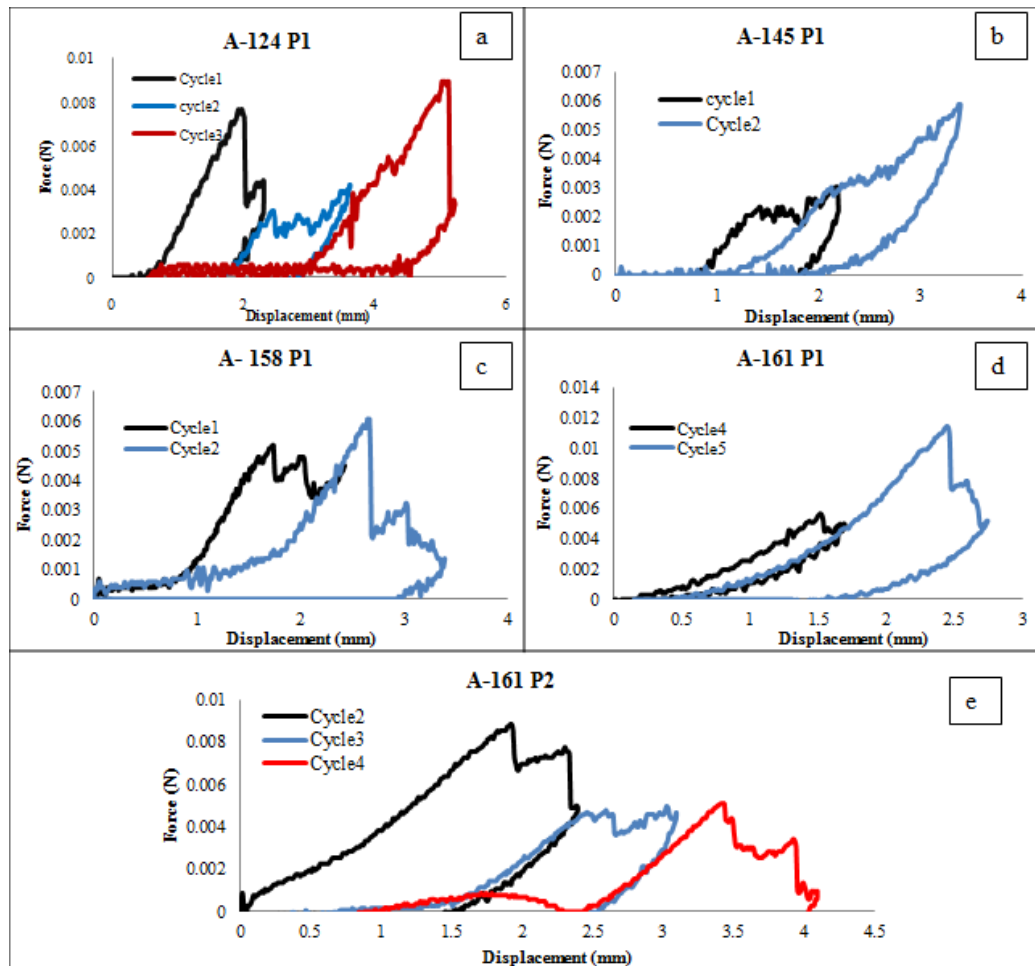


Figure 5.2: Force vs Displacement curves obtained experimentally for the 5 plaques tested from the ApoE<sup>-/-</sup> mouse group

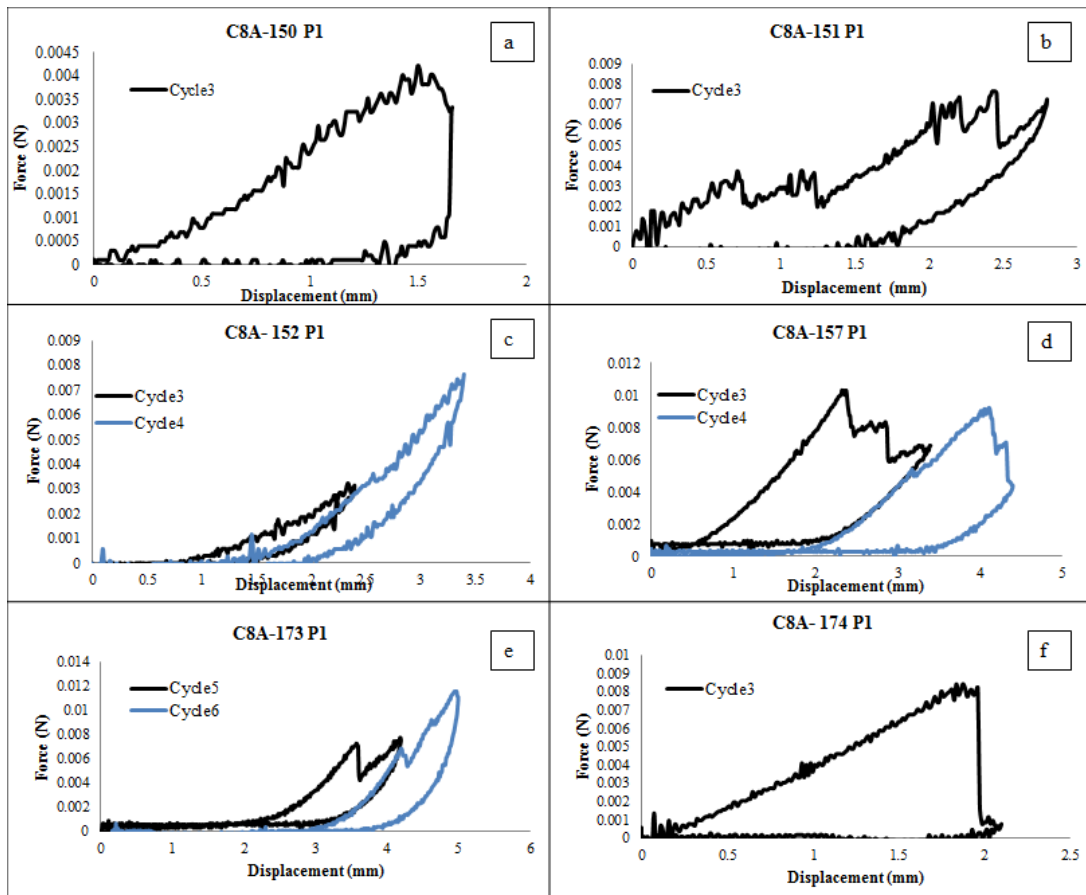


Figure 5.3: Force vs Displacement curves obtained experimentally for 6 plaques tested from the ApoE<sup>-/-</sup> Col8<sup>-/-</sup> mouse group

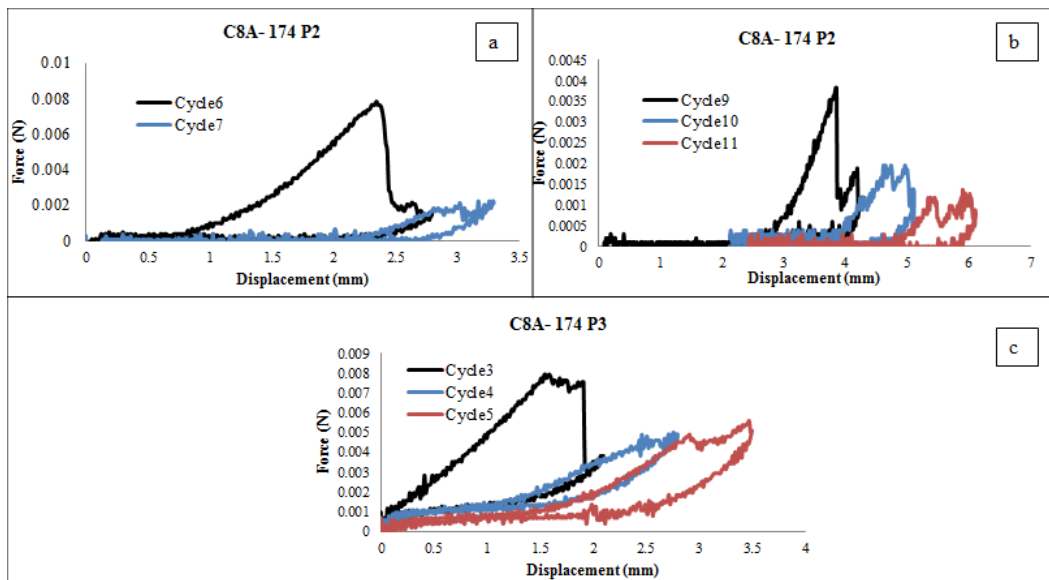


Figure 5.4: Force vs Displacement curves obtained experimentally for the remaining 3 plaques tested from the ApoE<sup>-/-</sup> Col8<sup>-/-</sup> mouse group

